Chem Soc Rev

REVIEW ARTICLE

View Article Online
View Journal | View Issue

Cite this: *Chem. Soc. Rev.*, 2022, 51, 6087

The advent of thermoplasmonic membrane distillation

Sergio Santoro,[a] Ahmet H. Avci,[a] Antonio Politano *[b] and Efrem Curcio*[a]

Freshwater scarcity is a vital societal challenge related to climate change, population pressure, and agricultural and industrial demands. Therefore, sustainable desalination/purification of salty/contaminated water for human uses is particularly relevant. Membrane distillation is an emerging hybrid thermal-membrane technology with the potential to overcome the drawbacks of conventional desalination by a synergic exploitation of the water–energy nexus. Although membrane distillation is considered a green technology, efficient heat management remains a critical concern affecting the cost of the process and hindering its viability at large scale. A multidisciplinary approach that involves materials chemistry, physical chemistry, chemical engineering, and materials and polymer science is required to solve this problem. The combination of solar energy with membrane distillation is considered a potentially feasible low-cost approach for providing high-quality freshwater with a low carbon footprint. In particular, recent discoveries about efficient light-to-heat conversion in nanomaterials have opened unprecedented perspectives for the implementation of sunlight-based renewable energy in membrane distillation. The integration of nanofillers enabling photothermal effects into membranes has been demonstrated to be able to significantly enhance the energy efficiency without impacting on economic costs. Here, we provide a comprehensive overview on the state of the art, the opportunities, open challenges and pitfalls of the emerging field of solar-driven membrane distillation. We also assess the peculiar physicochemical properties and synthesis scalability of photothermal materials, as well as the strategies for their integration into polymeric nanocomposite membranes enabling efficient light-to-heat conversion and freshwater.

Received 19th August 2021

DOI: 10.1039/d0cs00097c

rsc.li/chem-soc-rev

1. Introduction

Freshwater availability in adequate quality and quantity is one of the major societal challenges.[1] Despite the significant technological progress made in the last few decades, demographic growth, climate change, intensive agriculture activities and rapid industrial development make water shortage one of the pressing global issues of this century.[2] The global annual water demand is estimated to increase from 3500 km^3 in 2000 to around 5500 km^3 in 2050.[3] Consistently, the World Health Organization (WHO) predicted an alarming scenario: about 50% of the world's population will live in water-stressed regions by the year 2025.[4]

This drives the need to develop innovative technologies to be able to meet the growing water demand, while reducing the water footprint.[5–7] Seawater desalination is considered the most reliable solution to the freshwater scarcity problem, considering that seawater constitutes more than 97% (*ca.* 1.4×10^9 km^3) of the total available water on Earth.[8,9] Besides, the post-treatment of industrial wastewater has gained more attention in order to reduce the environmental impact in the logic of Circular Economy.[10,11]

Desalination is essentially defined as the process used to produce potable water by removing dissolved salts and minerals from seawater and brackish water.[12] Existing desalination technologies are conventionally classified into two main categories: (i) thermal-based evaporative processes (with phase change) and (ii) filtration-based processes (without phase change).[13] However, the widespread application of these processes, such as multi-stage flash distillation (MSF), multi-effect distillation (MED) and reverse osmosis (RO), requires significant energy power: the demand of conventional thermal desalination processes is 10–15 kW h m^{-3} to vaporize saline water,[14] whereas 3–6 kW h m^{-3} is needed to overcome the osmotic pressure of seawater in RO.[15,16]

The concern about the water–energy nexus due to the urgency of the sustainable production of freshwater without stressing energy supplies has led to membrane filtration as the prominent technology for desalination. In 2021, *ca.* 78 million cubic meters of water were produced per day;[17] RO covers about 60% of global desalination capacity,[18] with an expected growth

[a] *University of Calabria – Department of Environmental and Chemical Engineering, Cubo 44 A, Via Pietro Bucci, 87036 Rende CS, Italy. E-mail: efrem.curcio@unical.it*
[b] *Department of Physical and Chemical Sciences, University of L'Aquila, via Vetoio, 67100 L'Aquila (AQ), Italy. E-mail: antonio.politano@univaq.it*

for the global market of major components of RO systems of $11.7 billion in 2020 and $19.1 billion by 2025 at a compound annual growth rate (CAGR) of 10.3% for the period of 2020–2025.[19]

Despite its success, the pitfall of RO is its maximum freshwater recovery factor which is typically limited to 40–50% due to the increase in the osmotic pressure of the hypersaline (>50 g L^{-1}) rejected stream, known as brine.[20,21] The effect of the osmotic phenomenon hampers the economic feasibility of brine desalination, since it involves severe risk of scaling and fouling in the membrane modules[22] and requires hydraulic pressure exceeding the membrane burst pressure (typically 70–80 bar).[23] As a result, RO desalination plants produce around 40 million m^3 day^{-1} of brine as a by-product discharged to the sea, along with other chemicals involved in the pre-treatment steps including iron, copper, zinc, and cleaning agents (such as hydrochloric acid, sodium hexametaphosphate, anti-scalants *etc.*), severely impacting the marine habitat and the surrounding ecosystem.[24,25]

In recent years, membrane distillation (MD) has emerged as a complementary hybrid thermal/membrane technology not limited by either osmotic or concentration polarization phenomena, having the potential to produce desalted water at recovery factors close to 90% and at moderate operating temperatures (60–80 °C).[26] Indeed, mass transfer in MD is driven by a partial pressure gradient across a hydrophobic microporous membrane; this promotes a net flux of water vapor from a warm saline feed contacting one side of the

Sergio Santoro

Dr Sergio Santoro is a researcher at the Department of Environmental Engineering of the University of Calabria (Italy) with an MSc (with honours) in Materials Science from the University of Calabria and a PhD in "Erasmus Mundus Doctorate in Membrane Engineering" from the Nova University of Lisbon (Portugal) in cotutelle with the University of Calabria (Italy) and the University of Zaragoza (Spain). He worked from 2011 to 2013 at ITM-CNR (Italy) and from 2016 to 2019 in the SAES Group (Italy). He is a co-author of >25 papers in peer-reviewed international journals (H-index = 13). He has participated in several research projects in international funding programs (FP7-NMP, ERANET-MED, Horizon 2020).

Ahmet H. Avci

Dr Ahmet Halil Avci obtained his PhD in Chemical Engineering from the University of Calabria (Italy) in 2018 under the supervision of Prof. Efrem Curcio. His expertise is in membrane preparation for different applications such as mixed matrix membranes for gas separation, polyelectrolyte membranes for reverse electrodialysis and photothermal microporous membranes for membrane distillation. He has participated in different projects supported by international funding programs, namely ExtraSea (ERANETMED), REMIND (MSACA-RISE), and Sea4Value (EU Horizon 2020). Currently, he is working as a postdoc on a project to harvest blue energy from natural and artificial sources in Sweden.

Prof. Antonio Politano has a PhD in Physics and is an Associate Professor at the Department of Physical and Chemical Sciences of the University of L'Aquila (Italy). Previously, he was a post-doc at the Italian Institute of Technology, Genoa (Italy), the Autonomous University of Madrid (Spain), and Imdea Nanociencia, Madrid (Spain). He has coauthored >200 papers in peer-reviewed journals (H-Index: 41) and he is the principal investigator of several national and international projects. He was awarded with three prizes for his scientific activity, four international fellowships, and the APS Outstanding Referee. He was an invited speaker at about 20 conferences. He is involved in the evaluation of research projects in 11 countries.

Efrem Curcio

Dr Efrem Curcio has a PhD in Chemical Engineering and is a full Professor at the Department of Environmental Engineering – University of Calabria (Italy), was a visiting scientist (2012) at the Department of Chemical Engineering – MIT Massachusetts Institute of Technology (Boston, US), has coauthored >130 papers in peer-reviewed international journals (H-Index: 44) and >150 publications in congress and conference proceedings in the field of membrane technology, is a recipient of the European Membrane Society Award 2004 for the best published paper in Membrane Science and Engineering, and has participated and coordinated several research projects in international funding programs (MISTI/MIT, VII EU Framework Programme, ERANET-MED, Horizon 2020, and Horizon EU).

membrane, towards the opposite side.[26] MD exhibits outstanding advantages with respect to conventional desalination processes: high quality of desalted water (theoretically, only volatile species evaporate, while dissolved salts are completely retained), small footprint, and low susceptibility of water vapor flux to feed concentration.[27,28]

Likewise, MD can be used in treating a large variety of industrial wastewater for the purification, extraction, concentration and final formulation of organic and inorganic species being a feasible route in order to implement the concept of Zero Liquid Discharge (ZLD).[29] Beyond the benefits related to the remarkable reduction in the amount of disposed brine, the possibility to concentrate saline solutions up to supersaturation allows the implementation of the concept of membrane distillation-crystallization, opening unprecedented horizons in raw material recovery by mining desalination brine.[30] To date, efforts have been focused on the development of innovative membranes and on process optimization, but MD is still far from technological maturity.

At the operational level, the performance of MD is negatively affected by the low thermal efficiency mainly due to temperature polarization (TP), a phenomenon intrinsically related to the removal of latent heat associated with water evaporation and – to a lesser extent – to the conductive heat flux through the membrane.[31] Since evaporation takes place at the feed–membrane interface, a decreasing feed temperature profile throughout the adjacent boundary layer is observed. Consequently, evaporation occurs at a temperature lower than the bulk value, the net driving force to the mass transfer decreases and, ultimately, the overall efficiency of the process drastically falls ($<50\%$).[32,33]

Despite the occurrence of TP, the low operative temperature of MD makes process integration with renewable energy or waste energy very attractive. Several attempts to exploit solar energy with MD for seawater desalination have been reported in the literature.[34–37] In the last decade, efforts have been focused on the development of autonomous solar driven MD units for desalination in arid and remote regions by using solar thermal collectors for heating the seawater or brackish water, while the electricity is supplied by photovoltaic panels.[38–40] Studies confirmed the viability of solar-driven MD, obtaining good quality of freshwater with a specific energy consumption of 200–300 kW h m^{-3}.[38–40]

Although solar energy is renewable, ''bulk'' heating of feed saline water is energetically inefficient due to the occurrence of TP within the boundary layer adjacent to the membrane. Conversely, photothermal nanomaterials as ''nano-heaters'' incorporated on the membrane surface promote a localized light-to-heat conversion, leading to the withdrawal of TP for highly efficient water evaporation. In the last few years, intensive efforts have been devoted to the rational design of efficient photothermal nanoparticles (NPs) through the fine tuning of their chemical composition, surface functionalization and structural morphology.[41,42] In particular, thermoplasmonics, *i.e.*, the light-to-heat energy conversion associated with optically resonant plasmonic excitations in metal NPs, has been demonstrated to be beneficial for facilitating the vaporization of water with photothermal interface.[43–45] Distinct from conventional intensive and inefficient heating in bulk water processes, interfacial vaporization boosted by photothermal surfaces drastically minimizes the heat loss by locally harvesting the heat at the water–vapor interface.[46,47]

Analogously, MD has received a new impulse due to the latest advances in thermoplasmonics that encourage the development of novel photothermal membranes for TP mitigation and improved MD performance.[48–50] Moreover, next-generation materials exhibiting photothermal effects have the potential to exploit solar renewable energy for decentralized off-grid desalination by converting sunlight into heat for a unique and favorable water–energy nexus.[51,52]

Here, we review the recent progress in the development of photothermal membranes prepared by the immobilization of advanced functional nanomaterials in a polymeric network for efficient light-to-heat conversion in solar-driven low-energy water purification applications.

Moving beyond solar steam generation, which is the topic of some previously published review articles, we critically focus on technological potential, current challenges, and perspectives of photothermal membrane distillation (PMD). The review critically discusses the link between the morphological and physicochemical properties of MD membranes and the fundamentals of light-to-heat conversion in photothermal NPs (metals, semiconductors, carbon-based materials, and polymers), offering a comprehensive background for the development of the next generation of PMD membranes. In addition, this review systematically assesses the impact of the design criteria of membrane modules and optimization of the process parameters on the photothermal-driven freshwater production. Overall, the review highlights the need for a multidisciplinary approach to drive the practical implementation of thermoplasmonic MD, embracing fundamental studies of physics for understanding the mechanism of light-to-heat conversion, advanced chemical synthesis for the preparation of photothermal NPs, advances in materials science for the development of effective photothermal membranes, and a rational engineering of the PMD process.

2. Membrane distillation (MD)

2.1 Membrane distillation (MD): operational principles

MD is a non-isothermal process based on the evaporation and transport of volatile molecules (usually water vapor) through the macropores (typical pore size of 0.05–0.5 μm) of a hydrophobic membrane contacting an aqueous solution, whereas non-volatile components (*i.e.*, ions, biomolecules, colloids, bacteria *etc.*) are rejected due to the hydro-repellent character of the membrane itself.[53,54] In this sense, the membrane does not play an active role as a selective material in the separation but provides a support for the creation of a liquid–vapor interface at each pore mouth where phase transition takes place. Therefore, MD is categorized as ''Membrane Contactors'' technology. Its unique operational features make MD suitable for a wide spectrum of applications, such as desalination, wastewater

decontamination and purification, and dehydration of aqueous solutions.[55] When protracting the dehydration of the aqueous solution above the saturation limit – thus leading to the formation of crystals – MD is referred to as membrane crystallization (MCr), a versatile technology able to control the nucleation rate by modulating both the supersaturation degree and the physicochemical properties of the membrane surface where nuclei originate.[56]

The productivity of MD is quantified in terms of transmembrane flux (J), which varies linearly with the partial pressure gradient (Δp_i) of the i-th component transported in the vapor phase across the membrane:

$$J = K \cdot \Delta p_i \quad (1)$$

where K is a coefficient mainly depending on the membrane properties.[66]

This gradient, acting as a driving force for the mass transfer in MD, is typically – but not exclusively – generated by a temperature difference (osmotic distillation[57] is an exception); in the most common case of an aqueous feed solution, mass transfer includes three main steps:

(1) evaporation of water molecules at the interface of the warm aqueous feed solution in contact with the membrane (''feed'' or ''retentate'' side);

(2) transport of water vapor across the membrane *via* Knudsen diffusion and/or molecular diffusion depending on the membrane pore size, the mean free path of diffusing molecules, and the eventual presence of trapped air in the pores;[58,59] and

(3) removal or condensation of water vapor on the opposite side of the membrane (the ''distillate'' side).

Depending on the methodology adopted to reduce the partial pressure on the distillate side, MD is classified into four basic configurations[60] (Fig. 1):

(1) Direct contact membrane distillation (DCMD): the distillate side consists of pure water set at a lower temperature with respect to the feed solution;[61]

(2) Air gap membrane distillation (AGMD): the distillate compartment consists of: (i) a thin and stagnant air gap and

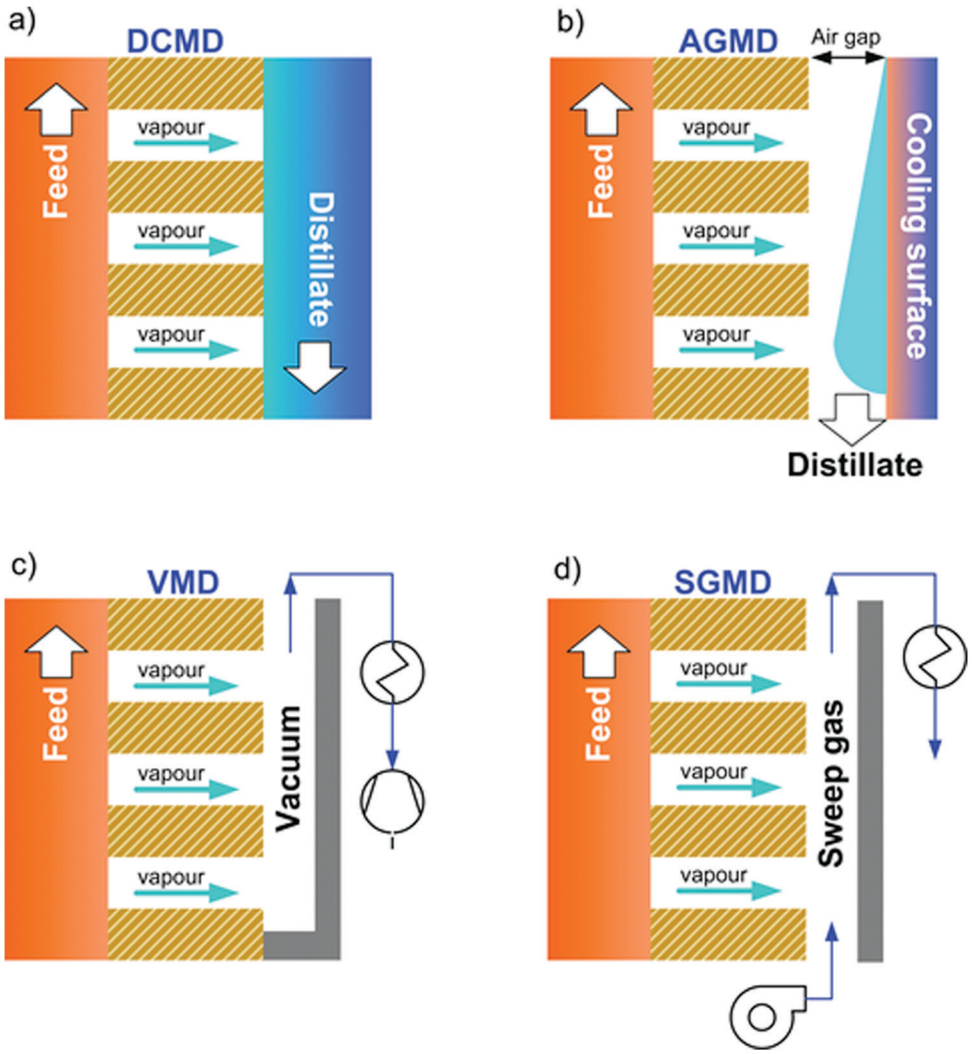

Fig. 1 The four basic membrane distillation configurations: (a) direct contact membrane distillation (DCMD); (b) air gap membrane distillation (AGMD); (c) vacuum membrane distillation (VMD) and, (d) sweep gas membrane distillation (SGMD).

(ii) a condensing cold surface made of a dense polymer or metal film;[62]

(3) Vacuum membrane distillation (VMD): a vacuum is applied at the distillate side at a level below the saturation pressure of water at the feed temperature, whereas the vapor is condensed in a subsequent step;[64]

(4) Sweep gas membrane distillation (SGMD): an inert sweep gas – which collects the vapor – flows at the distillate side, whereas condensation takes place in a subsequent step.[63]

Other configurations can be regarded as variants or hybrids of the four basic schemes previously described. For instance, permeate gap membrane distillation (PGMD) is a combination of AGMD and DCMD obtained by sandwiching the distillate channel between the membrane and the cooling surface.[65] Vacuum-enhanced air gap membrane distillation (V-AGMD) is a combination of AGMD and VMD, where a weak vacuum is used to suck air from the gap (while allowing the condensation of the vapor) in order to decrease the mass transfer resistance.[66]

2.2 MD membranes

2.2.1 Polymeric membranes. Although inorganic membranes in the form of hydrophobized metallic stainless-steel hollow fibers[67–69] or ceramic membranes[70] have been marginally explored in laboratory activities, the vast majority of membranes for applications in MD – including commercial ones – are usually made of inherently hydrophobic polymers, such as polytetrafluoroethylene (PTFE), polyvinylidene fluoride (PVDF) and polypropylene (PP).

Fluoropolymers are particularly suitable for MD, owing to their high thermal and chemical stability, and low surface tension. These properties are mainly related to the low polarizability, strong electronegativity, and minimal van der Waals radius of the fluorine atom combined with the strength of the C–F bond.[71] Among the above-mentioned polymers, PTFE has been widely used due its low surface energy (9–20 $\times$ 10^{-3} N m^{-1}) and high crystallinity.[72] The high degree of crystallinity (in general from 92% to 98%) depends on the long and unbranched PTFE molecules with CF_2 groups along the polymer chain, twisted into a helix as in a length of rope whereas fluorine atoms prohibit a planar zigzag conformation.[71] On the other hand, PTFE is poorly soluble being non-polar, thus hampering membrane preparation *via* phase-separation methods widely used in industrial practice, such as non-solvent induced phase separation (NIPS) or thermal induced phase separation (TIPS). Usually, PTFE membranes are prepared *via* the sintering process by mixing PTFE powders with volatile lubricating agents, resulting in a paste, subsequently extruded into flat sheets or hollow fibers.[73] Alternatively, PTFE membranes are prepared *via* the polymer melt extrusion method followed by stretching.[74]

PVDF, consisting of long chain macromolecules containing 59.4 wt% fluorine and 3 wt% hydrogen,[71] represents the most diffuse polymer used in the fabrication of membranes for MD,[75] as a result of its superior solubility in a wide range of polar aprotic organic solvents, such as *N*-methyl-2-pyrrolidone (NMP), *N*,*N*-dimethylformamide (DMF), or dimethylacetamide (DMA),[60] allowing membrane preparation using conventional phase inversion techniques. The Hansen solubility parameters, based on the assumption that cohesive energy can be expressed in terms of contributions from dispersive (δ_d), polar (δ_p) and hydrogen bonding (δ_h) forces, are effectively used to estimate the affinity between polymers and solvents.[76,77] As shown in Table 1, the Hansen parameters of PVDF are close to the ones of a wide range of solvents complying with the chemist's ''rule of thumb'' that ''like dissolves like''.[77,78]

Table 1 Hansen parameters ($MPa^{\frac{1}{2}}$) of PVDF in comparison with those of PTFE and common solvents[77,82–84]

Chemical	δ_h	δ_d	δ_p
PVDF	9.2	17.2	12.5
PTFE	0	14	0
TEP	9.2	16.8	11.5
DMF	11.3	17.4	13.7
DMA	11.8	17.8	14.1
NMP	7.2	18.4	12.3
Polar clean	9.2	15.8	10.7

Consequently, PVDF enables high processability, flexible manufacturing in large-scale production, low cost and fine control on the membrane morphology.[79] Moreover, recent studies have shown the feasibility of PVDF membrane preparation using green solvents (*e.g.*, dimethyl sulfoxide (DMSO),[80] triethyl phosphate (TEP),[81] and methyl-5-(dimethylamino)-2-methyl-5-oxopentanoate known as Rhodiasolv Polarclean®[79]).

Macroporous PP membranes are also widely employed for MD applications, due to their superior elastic properties and crystallinity.[60] PP membranes are fabricated either by dry-uniaxial stretching or by thermal phase separation after dissolving the polymer in diluents at a temperature above its melting point.[85] Physicochemical properties of PP membranes, such as crystallinity, porosity and mechanical response, are easily tuned by post-stretching or annealing, since during membrane preparation the polymer is rapidly cooled down from the melt state to room temperature leading to imperfect packing density.[86,87] Thus, post-treatment usually promotes polymer chain relaxation reaching a thermodynamically stable state causing ultimately significant changes in microstructure and physical properties.[86,87]

2.2.2 Required membrane properties. The prevention of membrane wetting is vital in MD, since mass transfer must take place exclusively in the vapor phase. This requirement is satisfied if the hydraulic pressure (applied to recirculate solutions within the membrane module) is lower than the liquid entry pressure (LEP), estimated by Laplace's equation:[75,88]

$$\mathrm{LEP} = -\frac{B \cdot \gamma_l \cdot \cos\theta}{r_{max}} \quad (2)$$

where B is a pore geometry coefficient (1 for ideally cylindrical pores, and 0.4–0.6 for stretched membranes with a small curvature radius[89]), γ_i is the liquid surface tension, θ is the contact angle at the membrane surface, and r_{max} is the maximum pore size of the membrane. While wetting risk is reduced for pure water and aqueous solutions of inorganic salts exhibiting high values of γ_l ($\geq$72.8 mN m^{-1}), the occurrence of natural organics, surfactants, oils *etc.* – even at low concentration – can significantly decrease the

surface tension of the feed solution.[90] Hydrophobicity is, hence, a critical requirement for the membrane, whose structure must consist of at least one hydrophobic layer to prevent wetting by the liquid phase.[75] A minimum LEP of 250 kPa is generally recommended.[91]

In MD, macroporous membranes exhibit a pore size typically in the range of 0.05–0.5 μm. Larger pore diameters, though favouring higher mass transport, increase the risk of wetting as per eqn (2).[75,92] Membranes with elevated porosity (ε = 70–80%), maintaining sufficiently high mechanical strength (elastic modulus of 34–491 MPa, tensile strength of 3.4–57.9 MPa, and elongation at break of 41–710%[91]), secure high transmembrane flux.

Conversely, the membrane thickness is a key parameter exhibiting counteracting effects on the performance of MD: a low membrane thickness reduces the resistance to mass transport and improves the transmembrane flux, whereas reduction of conductive heat loss is favoured by a thick membrane. On the basis of this trade-off, the optimal membrane thickness lies between 10 and 60 μm.[93]

In general, membranes for MD require specific optimization of materials, structural and physicochemical properties.[92] Different conventional and innovative techniques for membrane preparation (*e.g.* electrospinning[94]) and membrane modification (*e.g.* stretching, grafting and plasma treatment[94]), as well as novel polymers (*e.g.* ethylene chlorotrifluoroethylene (ECTFE)[95,96] and Hyflon[97]) have been explored in the last few decades. Several studies have been focused on mixed matrix membranes, where different fillers play a key role in favoring the mass transport or enhancing the thermal efficiency of MD.[94] A wide variety of nanomaterials have been also explored to provide antifouling,[98] bactericidal,[99] sensing,[100,101] and catalytic[102,103] properties.

Table 2 offers an overview of the main requirements of conventional membranes for MD applications.

2.3 Current challenges in energy efficiency

Since feed temperatures in MD typically range from 60 °C to 80 °C, low-energy waste heat or solar energy is suitable for the process. The specific thermal energy consumption (STEC) defined as the ratio of the rate of thermal energy added to the system (kW h s^{-1}) to the total production of distillate (m^3 s^{-1}) ranges – for most commercially available MD modules – between 100 and 500 kW h m^{-3} depending on the operational conditions (mainly temperature difference and feed flowrate) and effectiveness of the heat recovery.[104,105]

Regardless of the peculiar advantages and drawbacks related to a specific configuration (Table 3), energy efficiency in MD is severely affected by: (i) temperature polarization to a greater extent when the transmembrane flux is higher (about 50–80% reduction in driving force[32,106]); (ii) conduction heat losses through the membrane; and (iii) mass transfer resistance within the membrane pores.

In MD, the term "temperature polarization" (TP) refers to the phenomenon whereby the temperature of the bulk feed solution is higher than the temperature at the feed side membrane interface, thus having a severe impact on transmembrane flux reduction. In this regard, Fig. 2a illustrates the temperature profiles within thermal boundary layers on both feed and distillate sides of the membrane for DCMD configuration. At the feed side, heat flux (Q_f) is transferred from the bulk to the membrane surface by convection:

$$Q_f = h_f \cdot \left(T_f^b - T_f^m\right) \quad (3)$$

where T_f^b is the bulk feed temperature, T_f^m is the feed temperature at the membrane interface, and h_f is the feed convective heat transfer coefficient.

The heat flux transferred through the membrane (Q_m), that is equal to Q_f at the steady state, takes place by (i) conduction through the membrane (not contributing to water evaporation) and (ii) latent heat (ΔH_v) associated with the transmembrane flux (J) of evaporating molecules:

$$Q_m = \frac{k_m}{\delta_m} \cdot \left(T_f^m - T_d^m\right) + J \cdot \Delta H_v \quad (4)$$

where k_m is the thermal conductivity of the membrane, δ_m is the membrane thickness, and T_d^m is the temperature at the membrane interface in the distillate side. For conventional MD membranes, the value of k_m generally lies in the range of 0.1–0.3 W m^{-1} K^{-1} considering a temperature of the membrane in the range of 20–80 °C.[107]

According to eqn (3) and (4), the overlapping effects of the removal of the latent heat of vaporization associated with the transmembrane flux and – to a lesser extent – of the conductive heat loss through the membrane, cause the TP phenomenon.

The reduction of the effective temperature difference (at the membrane interface) with respect to the theoretical driving force (across the bulks) is quantified by the temperature

Table 2 Physicochemical membrane properties for MD operations

Parameters	Recommendations (range used in the literature)	Impacts
Membrane thickness (δ)	10–60 μm (10–200 μm)	Trade-off between the thermal efficiency and the mass transfer
Contact angle (θ)	>90° (90°–160°)	High wetting resistance
Liquid entry pressure (LEP)	>250 kPa (50–460 kPa)	High wetting resistance
Porosity (ε)	70–80% (40–90%)	High flux and energy efficiency Reduces the mechanical strength of the membrane
Average pore size (r_{max})	0.3 μm (0.05–0.5 μm)	Low pore size reduces the risk of wetting but compromises the flux
Thermal conductivity (k_m)	As low as possible (0.1–0.3 W m^{-1} K^{-1})	Mitigate the temperature polarization
Tortuosity	As low as possible (1.0–3.9)	High pore tortuosity reduces the flux
Tensile strength	As high as possible (3.4–57.9 MPa)	High mechanical stability of the membrane

Table 3 Advantages and disadvantages of the four main MD configurations

MD configuration	Advantages	Drawbacks
DCMD	– Technologically simple in design, easy scale-up – Moderate transmembrane flux – Direct condensation of the distillate inside the module	– High thermal conductive loss
AGMD	– Low thermal conductive loss – Feed solution used as a cooling medium (pre-heating) – Direct condensation of the distillate inside the module (heat recovery)	– Low transmembrane flux due to additional mass transfer resistance of the air gap
SGMD	– Moderate transmembrane flux – Low thermal conductive loss	– High cost for condensing the distillate outside the module
VMD	– High transmembrane flux – Very low thermal conductive loss	– High cost for vacuum – High cost for condensing the distillate outside the module

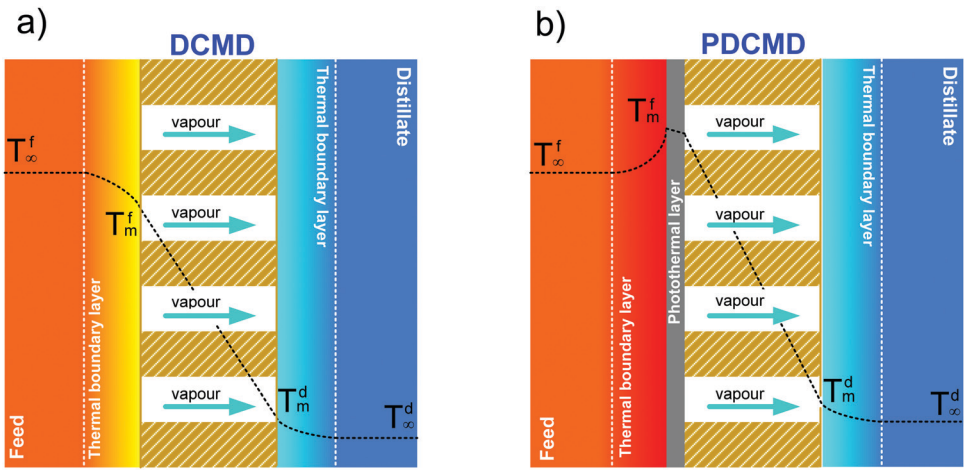

Fig. 2 (a) Temperature profile in the direct contact membrane distillation (DCMD) configuration; (b) photothermal direct contact membrane distillation (PDCMD): the effect of a self-heating membrane surface incorporating metal NPs as localized "nano-heaters" on the temperature profile.

polarization coefficient (TPC):[108,109]

$$\mathrm{TPC} = \frac{T_{\mathrm{m}}^{\mathrm{f}} - T_{\mathrm{m}}^{\mathrm{d}}}{T_{\infty}^{\mathrm{f}} - T_{\infty}^{\mathrm{d}}} \quad (5)$$

For VMD, temperatures related to the distillate side are omitted in (5). In general, TPC (≤ 1) becomes more pronounced in the axial direction of the feed stream flowing tangentially to the module and, operationally, it is maximized by enhancing the mixing degree inside the membrane module for a subsequent reduction of the boundary layer thickness.[110–112] Unfortunately, high feed velocities induce a severe pressure drop causing membrane pore wetting and reduction in the quality of permeate flux.[110,111] Several studies were focused on the development of membrane modules and spacers able to promote turbulences, with modest outcomes.[111]

Recently, significant progress in the design and synthesis of advanced photothermal materials has allowed devising innovative nanotechnologies with excellent light-to-heat efficiency. Specifically, the incorporation of nanomaterials exhibiting thermoplasmonic effects in polymers has opened unprecedented scenarios related to radically innovative concepts enabled by UV- or sunlight-driven self-heating membranes. This is the premise for a radical change in the MD paradigm: from the conventional and highly energy-intensive approach of heating the bulk feed solution to efficient localized heating at the membrane surface – where water evaporation takes place – not limited by temperature polarization (Fig. 2b).

3. Photothermal materials

Recently, many classes of nanomaterials have emerged as promising candidates for light-to-heat conversion, whose efficiency can be tailored by tuning the physicochemical properties and atomic structure through bottom-up synthesis strategies.[113] Specifically, photothermal materials can be classified into four categories: metals, inorganic semiconductors, carbon-based nanomaterials and polymers (see Table 4).

3.1 From plasmons to thermoplasmonics

Plasmons are intrinsic collective charge oscillations coupled *via* the Coulomb interaction, which constitutes the restoring force. Specifically, bulk plasmons are excited at the plasma frequency, for which the real part of the dielectric permittivity is zero (epsilon-near-zero, ENZ, conditions[114]). Bulk plasmons are longitudinal waves and, generally, they cannot be excited with free-space light (transverse waves). However, it has been shown

Table 4 Main classes of photothermal materials

Photothermal materials	Advantages	Drawbacks
Metals	Size-dependent optical properties Efficient light-to-heat conversion	Chemical instability for transition metals Expensive raw materials in the case of noble metals Plasmonic excitations typically in the UV range
Inorganic semiconductors	Chemical stability Moderate cost of raw materials	Modest efficiency of light-to-heat conversion
Carbon-based nanomaterials	Chemical stability Efficient light-to-heat conversion	Complicated routes of synthesis for nanotubes Poor scalability
Polymers	Inexpensive materials Processability	Poor efficiency of light-to-heat conversion

that the bulk plasmons (ENZ modes) are not completely longitudinal waves for ultrathin thickness,[115,116] so that they can be excited with free-space light. Conversely, surface plasmon polaritons and localized surface plasmons can couple with light.[117] These surface modes are collective charge oscillations at the interface between a dielectric and a conductor, with a resonance frequency smaller than that of bulk plasmons, as shown in Fig. 3.

The opportunity to excite and manipulate surface plasmon polaritons and localized surface plasmons has merged photonics and electronics at the nanoscale.[118] However, to date, plasmons have been used mostly in optoelectronic[119–123] or biomedical[124–127] applications. The relatively high losses and the limited choice for materials represent serious hurdles for extending the application fields. Decay of plasmons into hot carriers is one of the main loss mechanisms,[128–130] that, however, could be exploited for thermoplasmonic applications, where conversion into heat is beneficial.

In particular, different decay channels (electron-to-photon, electron-to-electron, and electron-to-phonon, see Fig. 4) permit the dissipation of plasmonic excitation in thermal energy.[131] The absorption and the subsequent temperature increase around plasmonic nanostructures were long considered as side effects in plasmonic applications, mostly related to the optical properties. Only recently the scientific community has realized that the enhanced light absorption at plasmonic nanostructures could make them ideal nano-sources of heat. Thermoplasmonics,[132] *i.e.*, the thermal heating associated with the excitation of plasmons in metal nanostructures, is based on the control of nanoscale thermal hotspots by light irradiation. Thus, thermoplasmonics allows for controlling thermal-related phenomena at the nanoscale. In particular, plasmonics offers new pathways and tools for chemical processes, through innovative or improved solutions to many important challenges in several subfields of chemistry, including NP chemistry,[133] catalytic reactions,[133,134] photovoltaics,[133] sensing,[135] biochemistry,[136,137] therapeutics[133] or membrane processes.[48]

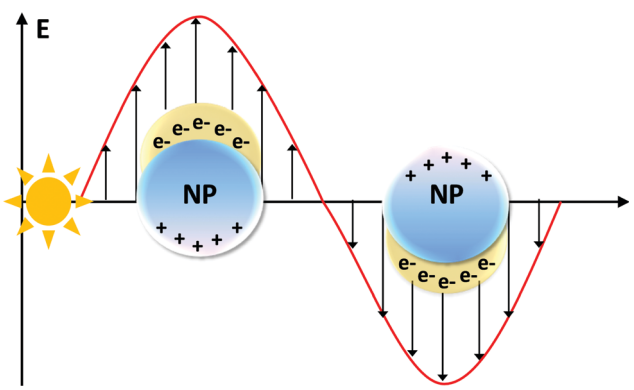

Fig. 3 Light irradiation of a metal NP induces the oscillation of the conduction band electrons. This collective electronic excitation is named localized surface plasmon resonance (LSPR).

The relative efficiency of scattering and absorption processes can be measured by introducing the photothermal efficiency:[138,139]

$$\mu = \sigma_{abs}/\sigma_{sct} \quad (6)$$

where σ_{abs} and σ_{sct} stand for absorption and scattering cross sections. Therefore, for an efficient light-to-heat energy conversion, μ (and σ_{abs}) should be maximized.

The heat power Q_j carried by each NP is directly related to σ_{abs}:

$$Q_j = \frac{1}{2}\sigma_{abs} n_m \varepsilon_0 c |E_{ext}|^2 \quad (7)$$

where n_m is the refraction index of the neighboring medium, ε_0 is the vacuum permittivity, c is the speed of light, and E_{ext} is the electric field of the external electromagnetic radiation.

Whenever NPs are sufficiently far from each other, they can be considered as optically independent and, therefore, the heating power of each NP (Q_{NP}) is equal, so that:

$$Q_{NP} = Q_j = I\sigma_{abs} \quad (8)$$

where I is the irradiance of the illumination (power per unit surface):

$$I = 1/2 n_m \varepsilon_0 c |E_{ext}|^2 \quad (9)$$

The absorption cross section can be estimated as:

$$\sigma_{abs} = k\mathrm{Im}[\alpha(\omega)] - \frac{k^4}{6\pi}|\alpha(\omega)|^2, \quad (10)$$

where k is the wave number in the medium and $\alpha(\omega)$ is the polarizability of the particle, which in the case of spherical NPs is given by the Clausius–Mossotti expression:

$$\alpha(\omega) = 4\pi R_{NP}^3 \left[\frac{\varepsilon(\omega) - \varepsilon_m}{\varepsilon(\omega) + 2\varepsilon_m}\right], \quad (11)$$

where ε_m is the dielectric constant of the medium and $\varepsilon(\omega)$ is

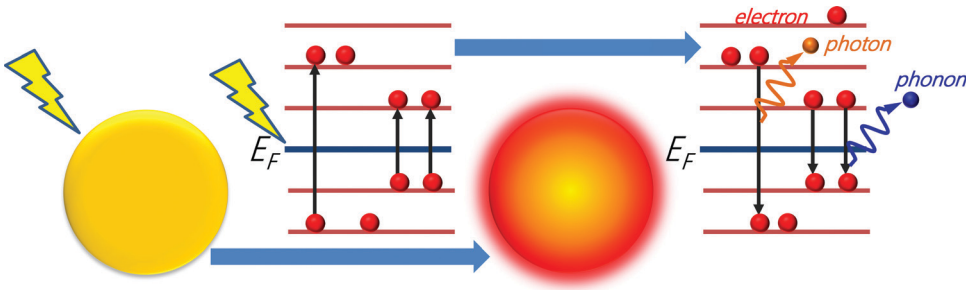

Fig. 4 Decay channels for plasmonic excitation: electron-to-photon, electron-to-electron, and electron-to-phonon.

the complex relative permittivity of the NP of radius R_{NP} dipped in a medium with real relative permittivity $\varepsilon_m = n_m^2$.

From eqn (11), one can infer a resonance condition for plasmonic NPs corresponding to $\varepsilon(\omega) \sim -2\varepsilon_m$.[140,141] As an example, for a spherical Au NP whose diameter is less than 30 nm, the resonance condition corresponds to $\lambda \sim 530$ nm.[132]

Therefore, the scattering cross section (σ_{sct}) scales as $\propto R_{NP}^6$ according to

$$\sigma_{sct} = \frac{8\pi}{3} k^4 R_{NP}^6 \left| \frac{\varepsilon(\omega) - \varepsilon_m}{\varepsilon(\omega) + 2\varepsilon_m} \right|^2. \quad (12)$$

Hence, size dependence plays a key role in the evaluation of the photothermal efficiency. Explicitly, in the case of Au NPs absorption dominates over scattering for NPs with diameter d below 80 nm (Fig. 5a), enabling their employment as nanoheaters, whereas scattering is preferential for larger NPs ($d >$ 80 nm) (Fig. 5a).

The extinction cross section, σ_{ext}, defined as the sum of absorption and scattering cross sections:

$$\sigma_{ext} = \sigma_{abs} + \sigma_{sct}, \quad (13)$$

depends on both the size and the wavelength (Fig. 5b), as evident from its behavior for the case-study example of Ag NPs (Fig. 5c).

The increase of the temperature (ΔT_{NP}) of a single NP irradiated by light is related to σ_{abs}:[143]

$$\Delta T_{NP} = \frac{\sigma_{abs} I}{4\pi\kappa R_{NP}}; \quad (14)$$

where κ is the thermal conductivity of the material. For one Au spherical NP with $R_{NP} = 100$ nm immersed in water, ΔT reaches *ca.* 50 K upon irradiation under resonant conditions (λ = 530 nm)[122] (Fig. 6a).

Whenever the concentration of the NPs increases, the distance among NPs is definitely reduced with the activation of the thermal collective effects.[144,145] Therefore, two different regimes are identified: (i) the "temperature confinement regime" related to the temperature distribution around the single hotspot and (ii) a "delocalization regime" consisting of a uniform temperature profile along the medium.[146] In the latter case, the temperature increase ΔT_{dr} is estimated to be:

$$\Delta T_{dr} = \frac{\sigma_{abs} I}{k} \frac{1}{4} \frac{D}{A} \left(1 - \frac{2\sqrt{A}}{\sqrt{\pi} D} \right), \quad (15)$$

where D is the diameter of the circular illumination and A is the unit cell area of the NP lattice.[146]

Indeed, for the case of an array of NPs with N elements, an additional contribution (ΔT_j^{ext}) arises from the heat delivered by the other $N - 1$ elements (q_k) of the array.[146] In a region of

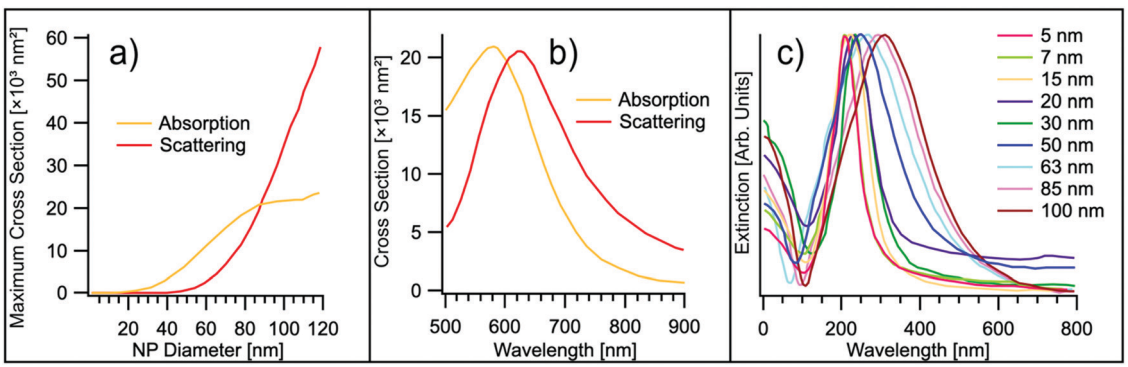

Fig. 5 (a) Evolution of the maximum absorption and scattering cross-section as a function of the NP diameter d for the case-study example of gold. Experimental points are taken from ref. 132. (b) Absorption and scattering cross-section for a gold nanosphere in water, with d = 88 nm. Experimental points are taken from ref. 132. (c) UV-Vis extinction spectra of Ag NPs of different diameters. Experimental points are taken from ref. 142.

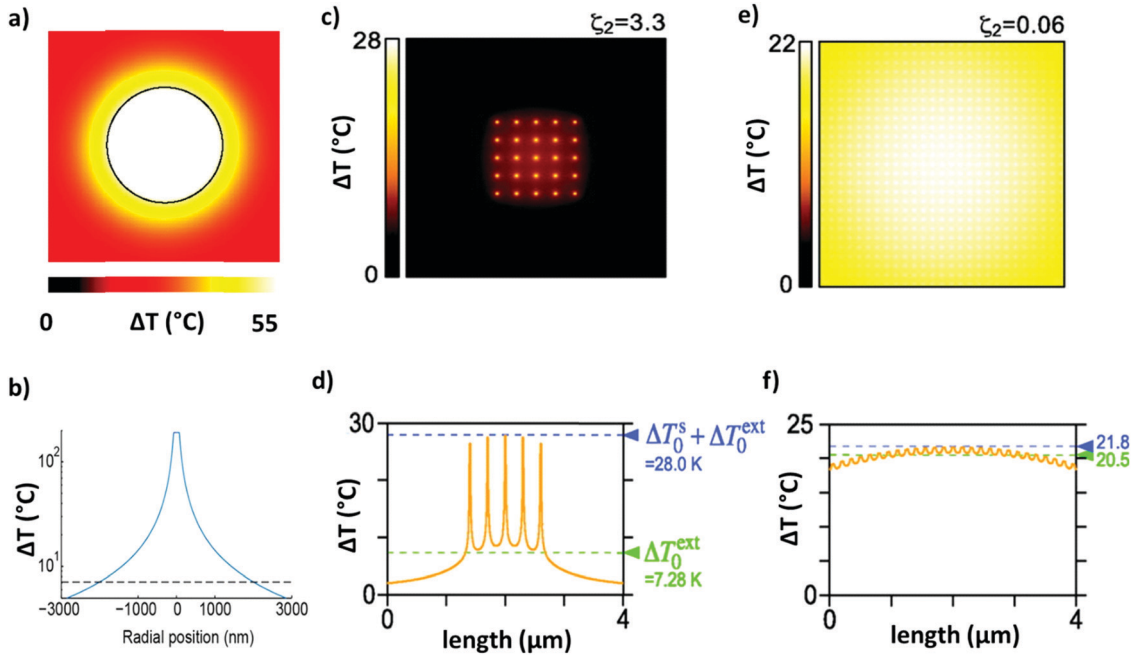

Fig. 6 (a) Equilibrium distribution of the temperature increase around an Au NP with a diameter of 100 nm irradiated with λ = 530 nm. Adapted with permission from ref. 143. Copyright 2010 American Chemical Society. (b) Temperature profile around an irradiated Au NP with a diameter of 150 nm (adapted from ref. 147. This work is licensed under a Creative Commons Attribution 4.0 International License). (c and d) Temperature distribution throughout a finite-size square lattice of NPs, uniformly illuminated (p = 300 nm, d = 15 nm, N = 5 × 5, and I = 5.7 × 10^9 W m^{-2}). Reprinted (adapted) with permission from ref. 146. Copyright 2013 American Chemical Society. (e and f) Temperature distribution throughout an infinite and periodic square lattice of NPs illuminated by a uniform circular beam (p = 150 nm, d = 40 nm, D = 6 μm, and P = 2 mW). Reprinted (adapted) with permission from ref. 146. Copyright 2013 American Chemical Society.

radius r_k around a NP, ΔT_j^{ext} is estimated to be:

$$\Delta T_j^{\text{ext}} = \sum_{\substack{k=1 \\ k\neq j}}^{N} \frac{q_k}{4\pi\bar{\kappa}} \frac{1}{|r_j - r_k|}, \tag{16}$$

where $\bar{\kappa}$ is the average conductivity of the interface between the NP and its environment.

The regime can be identified by analyzing the dimensionless number ζ_2, defined as the ratio between ΔT_{NP} associated with the single particles and ΔT_0^{ext} related to the contribution from the 2D array, as follows:[146]

$$\zeta_2 = \frac{l^2}{3R_{\text{NP}}L}, \tag{17}$$

where l is the distance between the particles and L is the size of the illuminated region. Thus, the temperature confinement regime dominates in the case of isolated NPs ($\zeta_2 > 1$), whereas in the case of a concentrated array ($\zeta_2 \ll 1$) the photothermal effect is homogenously distributed over the portion of the space occupied by the array. Therefore, NPs act as nanoscale thermal hotspots in the temperature confinement regime (Fig. 6c), while a homogeneous dispersion of concentrated NPs provides a homogeneous heating of the medium, regardless of the nanometric size of the NPs (Fig. 6e).

Overall, the contribution of an array of metallic NPs in a homogeneous medium is obtained by solving the equation for heat flow transfer, given by:

$$\rho(r)c_p(r)\frac{\partial T(r,t)}{\partial t} = \nabla k(r) + \nabla T(r,t) + Q(r,t), \tag{18}$$

where ρ, c_p, k, and T are the mass density, specific heat, thermal conductivity and temperature, respectively, expressed as a function of time t and/or coordinate r and $Q(r, t)$ is the local heat intensity.[144] Consequently, it is rather difficult to estimate the effect of nano-heaters on the temperature of the membrane in PMD. Recently, the model was modified by adding a term considering the loss of heat in heat density $D(r, t)$ as reported in the following equation:

$$D(r,t) = \frac{\mathcal{L}}{k} - \frac{v(r,t)}{\beta\tau}; \tag{19}$$

where $\upsilon = \Delta T_{\text{m}}(r, t)$ is the medium temperature increase, $\beta = k/\rho c$ is the thermal diffusivity of the medium, $\mathcal{L}$ is the effective continuous heat production from NPs depending on the excitation energy, the intensity, the NP size and their concentration, and τ is a cooling time constant taking into account the dissipative phenomena.[148] According to this model, the membrane steady-state temperature ($\Delta T_{\text{m}}^{\text{SS}}$) in a spherical section of radius R_{m} is defined as:[148]

$$\Delta T_{\text{m}}^{\text{ss}} = -\frac{\mathcal{L}\kappa\tau}{k}\left\{\left(1 + \frac{R_{\text{m}}}{\sqrt{\beta\tau}}\right)e^{\frac{-R_{\text{m}}}{\sqrt{\beta\tau}}}\right\} + \frac{\mathcal{L}\beta\tau}{k}. \tag{20}$$

The model in ref. 144 was compared to recent experiments[148] and to the theoretical model proposed by Baffou *et al.*[146] Fig. 7

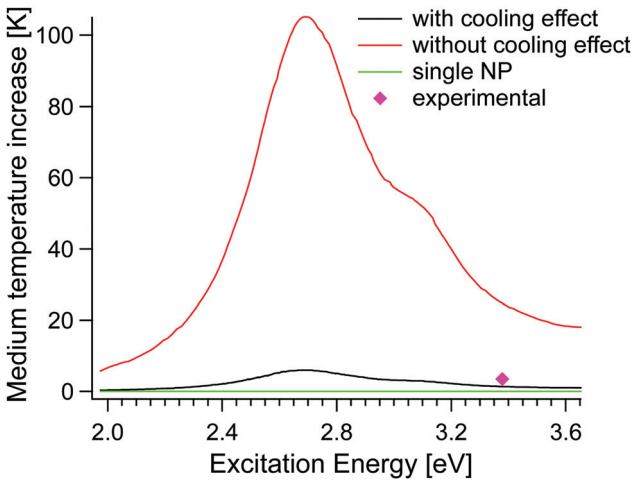

Fig. 7 Membrane temperature increase as a function of the excitation energy, with (model by Elmaghraoui[148]) and without the cooling effect (model by Baffou *et al.*[146]). The heating generated from a single NP, represented by the green curve is practically invisible as the maximum temperature is too small. Experimental points are taken from ref. 148.

shows the increase of membrane temperature as a function of the amount of Ag NPs with and without considering the dissipative cooling effect, respectively. For the two models, the membrane temperature increases with the amount of nanofillers, although the model by Elmaghraoui *et al.*[148] gives a better description of the experimental results, thus validating the importance of the cooling effect in modelling photothermal MD.

The validation by direct measurements of the temperature at the nanoscale is technically challenging and macroscale experiments are often characterized by collective heating effects, which tend to make the actual temperature increase unpredictable. Moreover, IR thermal radiation measurement fails at the nanoscale since it implies the employment of micrometric wavelength (>10 μm). To date, several optical techniques have been explored for thermal microscopy,[149–151] half of them based on the employment of luminophores with a strong temperature-dependent emission,[151–153] limited by their poor emission and chemical stability at high temperature. Interestingly, luminophores have been recently exploited for the *in situ* monitoring of membrane processes and the experimental evaluation of the temperature on membrane surfaces, opening up interesting perspectives for the empiric description of TP and, eventually, of the effect of thermoplasmonics in the membrane process.[32,33,100,154]

3.2 Metals

Commonly, the plasma frequency of metals occurs in the UV region with energy between 5 and 15 eV, depending on their band structure.[155] However, plasmonic modes in metals are affected by large losses related to interband transitions. These losses are detrimental to the performance of plasmonic devices, seriously limiting the feasibility of many plasmonic applications,[156] but not those related to energy conversion, such as plasmon-assisted photocatalysis and thermoplasmonic MD.

In general, d-electron metals (including noble metals) show strongly damped features in the excitation spectra, owing to efficient decay channels associated with interband transitions involving d-bands.[157] For Ag and Au, interband transitions starting from d-bands induce a shift of the energy of the surface plasmon from 6.5 eV (as expected for a free-electron gas of density matching with Ag and Au) to 3.8[157] and 2.5 eV,[158] respectively. In particular, Ag plasmonic modes show large values of the propagation depth (up to 10 μm),[159] due to the relatively low value of the imaginary part of the dielectric function around frequencies of the resonance conditions.[157]

Alkali metals, such as Na and K, show minimal loss compared to Ag but they are extremely reactive in the ambient atmosphere or in aqueous solutions, thus hindering their practical applications.[160]

In the ultraviolet range, Al represents a better choice for plasmonics, although Al is easily oxidized in the ambient atmosphere. Definitely, the formation of native Al_2O_3 oxide induces a shift of the surface plasmon resonance from 10.5 to 6.5 eV.[161] Similarly, surface plasmon resonance in Mg is red-shifted from ~ 7 to ~ 5 eV upon air oxidation. Al NPs, able to absorb the solar spectrum ($>96\%$), were found to be beneficial for solar-driven desalination.[162]

To quantify the relative efficiency of plasmonic metals, it was proposed to simply consider the ratio between the real part and the imaginary part of the permittivity of the material at the considered wavelength $-\varepsilon'(\lambda)/\varepsilon''(\lambda)$.[163–165] Although this figure of merit was extensively adopted, it is inadequate for quantitative comparison between different materials, or between different wavelengths, and it does not account for the nature of the surrounding medium. Recently, the Joule dimensionless number (J_0) has been proposed for quantifying the ability of a material to produce heat:[166]

$$J_0 = \frac{\lambda_{ref}\sigma_{abs}}{2\pi V_{NP}}; \quad (21)$$

with V_{NP} being the volume of the NP, and λ_{ref} is fixed as 1240 nm (Fig. 8).

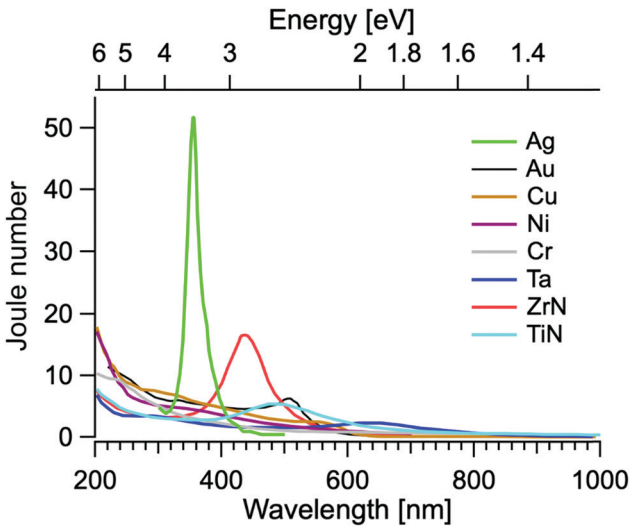

Fig. 8 J_0 for different metals: Ag, Au, Cu, Ni, Cr, Ta, ZrN and TiN. Experimental points are taken from ref. 166.

Table 5 Dimensionless number J_0, characterizing the capability of one metal to generate heat[166]

Element	λ [nm]	J_0
Au	528	6.3
Ag	357	52.0; ~111
Cu	585	2.6
Al	140	~477
Co	366	>12
Cr	289	>11
Fe	337	>11
Mo	154	41.3
Mn	380	>9.2
Ni	218	21.4
Pd	223	>21
Pt	323	~12

Table 5 reports the Joule dimensionless number along with the corresponding resonance wavelengths (λ) of several elements. Al shows the highest photothermal efficiency (J_0 = 477), although in the ultraviolet, thus beyond the solar radiation spectrum. In the range of solar radiation, Ag displays the highest photothermal efficiency, with values ranging from 52 to 111, depending on the reference adopted from optical constants.[167,168] As a matter of fact, usually numerical estimations for Ag difficulty match experimental results, mainly owing to sulfidation with the ultimate formation of Ag_2S on the NP surface,[169] which strongly damps Ag plasmonic excitations and it is difficult to control.

The photothermal efficiency of Ag and Au was widely explored, considering their tunable absorption properties, morphology and size combined with chemical stability.[170–173]

Concerning Cu, its surface oxidation dramatically hinders its practical application in thermoplasmonics.[174] Nevertheless, significant efforts were focused on the limitation of the oxidation of both Cu and Al NPs by the employment of an ultra-thin protective coating or corrosion inhibitors.[175,176]

Most recently, photothermal effects in bimetallic NPs (Fe–Au,[177] Ag–Au[176] or Pd–Au[178]) have been explored for exploiting the possibility to tune the plasmonic frequency through the stoichiometry of the bimetallic alloy.

3.3 Inorganic photothermal semiconductors

Inorganic semiconductors, exhibiting a bandgap between the valence band (VB) and the conduction band (CB), act as photothermal materials. Photo-excited electrons with incident light energy greater than the band gap energy first transfer to CB-bottom *via* non-radiative transition, then return to the VB recombining with holes and releasing energy in the form of light (dissipated as radiation) and heat.

Limitations related to the narrow absorption wavelength of TiO_2 (bandgap of 3.2 eV, only responsive in the UV region[179]) were mitigated through magnesium reduction to give black TiO_x NPs.[180] Besides, narrow-bandgap Ti-based semiconductors, such as nanosized titanium sesquioxide Ti_2O_3 (~400 nm particle size, bandgap ~0.1 eV) absorbed almost 94% of UV, 95% of visible, and 89% of infrared solar irradiation with a total absorption capacity of 92.5% over the whole solar spectrum;[181] analogous broadband absorption properties were also detected for TiAlN black coatings with a vertically aligned columnar structure[181] and layer-by-layer assembly of TiN plasmonic NPs with polyelectrolytes.[182]

In addition, Si and Ge are efficient photothermal materials as the largest part of their absorbed energy is thermally dissipated. For instance, water-dispersed Ge NPs with a diameter in the range of 3–5 nm irradiated with light (λ = 770 nm, P = 0.9 W cm^{-2}) demonstrated efficient light-to-heat conversion, as indicated by the temperature increase of *ca.* 20 °C.[183] Similarly, suspensions of porous Si in salty water are heated by ΔT = 27 °C upon irradiation with NIR light (P = 0.3 W cm^{-2}).[184]

Unfortunately, synthesis routes for colloidal semiconductor NPs with uniform sizes and shapes are much less mature with respect to metal NPs. Explicitly, Ge requires high temperature of crystallization and, moreover, its salts need harsh reaction conditions and chemicals to be converted into elemental Ge;[185] similar concerns exist for Si.

Degenerately doped semiconductors, such as copper chalcogenides $Cu_{2-y}X$ (X = S, Se, Te) are suitable candidates for thermoplasmonic applications, also considering the density of free carriers as high as 10^{21} cm^{-3}.[186] Recently, copper chalcogenides have been explored in biomedical applications. In particular, CuS NPs with an average size of *ca.* 3 nm, dispersed in an aqueous medium under light irradiation (λ= 808 nm, P = 24 W cm^{-2}), increased the surrounding temperature by *ca.* 12.7 °C in 5 min, killing about 50% of the cancer cells.[187] The presence of intermediate bands in the energy gap provides additional channels for light-to-heat-conversion, as it enables the relaxation of the photo-excited electrons *via* the non-emissive pathway,[188] thus improving the photothermal efficiency. As an example, chalcopyrite ($CuFeS_2$), empty Fe 3d orbitals generate an intermediate band activating an additional absorption at 0.5 eV,[188] activate an additional absorption at 0.5 eV. Frequency tunability is achieved by changing the stoichiometry.[189] However, the difficult scalability due to synthesis issues and the insufficient stability of copper chalcogenides inevitably limit their extensive use as photothermal agents.

Lately, nano-sized MoS_2-based materials exploiting the excellent solar absorbing performance of the 2D transition metal dichalcogenide have also attracted attention in solar desalination applications.[190]

3.4 Carbon-based photothermal materials

Carbon-based photothermal materials can absorb light – efficiently converted into heat – like a black body, and exhibit the advantages of inexpensiveness, wide variety of optical and chemical properties and excellent ambient stability.[191] The large number of conjugated π bonds present in carbon nanotubes (CNTs) and graphene results in a red-shift of the absorption light spectrum for high-efficiency solar energy utilization. In addition, a very low reflectance (<4% in UV-vis-IR regions) is observed for vertically aligned multiwall carbon nanotubes (MWCNTs).[192,193] The combination of strong absorption capacity (up to 98% in the visible and NIR region[194]) and exceptional thermal conductivity (higher than 2000 W m K^{-1}[195] although amorphous carbon-based nanostructures display inferior values due to phonon

scattering[196]) guarantees both high light-to-heat conversion and remarkable heat transfer to the surrounding environment.[197]

Graphene-based derivatives, with easily tunable optical and surface properties, are promising photothermal nanofillers. Recently, it has been shown that dispersions of reduced graphene oxide (rGO) with concentration of 30 μg mL^{-1} under irradiation (t = 5 min, λ = 808 nm, P = 0.6 W cm^{-2}) heated up from 25 to 70 °C,[198] whereas an improvement of *ca.* 30 °C has been observed when using CNTs as photothermal materials under a solar illumination intensity of 10 kW m^{-2}.[199] Interestingly, the effect on the bulk fluid temperature was maximized at a CNT concentration of 4.76 × 10^{-4} vol% whereas, a higher amount of CNTs hindered the photothermal activity of nanofillers dispersed below the top layer directly exposed to the radiation.[199] Despite their excellent photothermal properties, these materials still suffer from important limitations related to complicated synthesis procedure and high fabrication cost.

Another promising class of carbon-based nanomaterials is represented by Ti-based carbide nanosheets, *i.e.*, MXenes, which display ∼100% light-to-heat conversion efficiency[200] in the NIR region, although the mechanisms ruling photothermal effects are unclear yet. An aqueous suspension of Ti_3C_2 nanosheets with a concentration of 72 ppm resulted in a temperature enhancement of 57 °C in 6 min upon laser irradiation at 808 nm (P = 1.5 W cm^{-2}).[201] While some researchers claimed the high photothermal efficiency to be related to light trapping effects with multiple reflection between layers,[202,203] a more reliable origin of the enhanced photothermal efficiency of MXenes is related to their plasmonic properties. Definitely, spatially-resolved electron energy loss spectroscopy experiments revealed that the plasmonic spectrum of MXenes exhibits both transversal (optically allowed) and longitudinal (optically forbidden) surface-plasmon modes ranging from visible down to 0.1 eV in the MIR region,[204] whose frequency can be tuned with the shape, size, and thickness of $Ti_3C_2T_x$ flakes (T = F, OH). Correspondingly, MXenes exhibit conductivity as high as 4600 S cm^{-1}.[202,205]

Nevertheless, the state-of-the-art synthesis techniques for MXenes do not enable scalability for industrial applications, owing to high costs and insufficient crystalline quality for large-scale production.[206,207] Furthermore, MXenes are hydrophilic,[208] with subsequent unfeasibility in their application as nanofillers for PMD.

3.5 Polymeric photothermal materials

Polymers afford several possible advantages, including high flexibility and mechanical resistance, tunable morphological properties, and low-cost and scalable synthesis. Unfortunately, they suffer from a narrow absorption window and limited charge-carrier mobility, restricting their employment as photothermal materials.[209] Strategies to overcome these drawbacks are based on the chemical modification of the polymers such as copolymerization of electron donor–acceptor complexes and oxidative doping.[209]

Their possible use as photothermal materials was explored for conjugated polymers, such as polyaniline (PANi)[210] and polypyrrole (PPy),[211] owing to the presence of π-conjugated backbones of sp^2-hybridized carbon atoms composed of aromatic heterocyclic rings.

Table 6 Efficiency of some selected photothermal materials

Material	Size (nm)	Concentration (μg mL^{-1})	λ (nm)	P (W cm^{-2})	ΔT (°C)	Ref.
Au nanorods	100	30	800	0.5	∼30	217
Ge NPs	3–5	1000	770	0.9	∼20	183
rGO	50	30	808	0.6	∼45	198
PANi NPs	116	500	808	2.4	∼55	215

PANi is characterized by light absorption in the visible and NIR regions and its Lewis basic character provides binding sites for dopants able to modulate the optical properties[212] by inducing mid-gap states.[213] Moreover, protonation in an acidic environment usually reduces the band gap causing a shift of the absorption toward the NIR region.[214] For instance, the maximum of absorption of PANi NPs (115.6 ± 16.3 nm) shifted from 580 to 810 nm in phosphate buffer solution (pH 1).[215] Correspondingly, irradiation by NIR light (λ = 808 nm, P = 2.45 W cm^{-2}) increased the temperature of a dispersion of PANi (concentration of 0.5 mg L^{-1}) by *ca.* 55 °C in 3 min.[215]

On the other hand, PPy has gained attention in photothermal ablation with promising results, as demonstrated by the efficient light-to heat conversion under NIR radiation (temperature increase from 21.3 to 55.8 °C) in a culture medium containing 30 μg mL^{-1} of Ppy NPs with a diameter of 46 nm.[216]

3.6 Outlook

Overall, extensive experimental and theoretical studies have been focused on identification of photothermal materials aiming to maximize the light-to-heat conversion. Tendentially, metal and carbon-based plasmonic nanostructures display superior performance, but economic issues related to the high cost of raw materials hinder the practical exploitation of the former, while the scalability of the routes of synthesis is the major drawback for the latter. In the case of semiconductors and polymers, the photothermal efficiency is insufficient and usually compensated by adapting highly concentrated systems (see Table 6).

4. Photothermally-assisted evaporation and photothermal membrane distillation (PMD)

Conventional thermal desalination occurs by bulk heating of feed seawater to generate vapor. Recently, emergent photothermal materials with efficient light-to-heat conversion have enabled innovative capabilities related to heat harvesting, opening up new opportunities for water purification and desalination.[218]

The efficacy of a photothermal material is usually evaluated in terms of the evaporation efficiency (η):

$$\eta = \frac{\dot{m}(\Delta H_v + \Delta H_s)}{I}, \quad (22a)$$

where I is the irradiance of the illumination, $\dot{m}$ is the mass flow

rate of vaporized water, and ΔH_v (J kg^{-1}) is the latent heat of vaporization of water that is a function of the temperature T (in K[219]):

$$\Delta H_v(T) = 1.91846 \times 10^6[T/(T - 33.91)]^2, \quad (22b)$$

and ΔH_s is the sensible heat required to increase the initial temperature of the system to the evaporation temperature (dependent on the specific heat of water c_p = 4186 J kg^{-1} K^{-1}).

Fig. 9 illustrates the evolutionary path of photothermal evaporation technology, starting from early investigations on nanofluids up to the most recent developments on photothermal membrane distillation. A critical discussion on each stage of advancement is proposed in the following sections.

4.1 From photothermal nanofluids to floating photothermal membranes

Preliminary investigations on photothermal evaporation of aqueous solutions were mainly focused on suspensions of photothermal NPs dispersed in a bulk solution, named "nanofluids", able to convert solar light to heat through the excitation of surface plasmon resonance. A practical problem of nanofluids is the need to separate the NPs from the solutions after the operation. In this respect, photothermal materials are often decorated with magnetic NPs, such as Fe_3O_4, to facilitate their recovery and recycle from the treated solution.[220]

Nanofluids, as volumetric heating systems, are affected by severe energy loss to the surrounding aqueous medium by thermal conduction and convection, thus resulting in the undesired heating of the bulk liquid with a consequently modest evaporation efficiency. With the aim to overcome these limitations, several non-submersible solar absorbers have been developed in order to achieve localized heat harvesting at the water–air interface.[221,222] Typically, the surface of the photothermal NPs is functionalized with hydrophobic moieties, such as alkyl or fluoroalkyl groups, in order to guarantee their self-floating capacity.[223] However, the side effects related to the exposure to light, chemical oxidation or physical rubbing were found to compromise the functionalization and, ultimately, the opportunity for NPs to be suspended at the water interface.[224]

Table 7 summarizes the performance of some selected photothermal materials for volumetric and interfacial evaporation.

Localized photothermal heating at the water–air interface maximizes solar utilization by suppressing heat loss to the bulk water, and thus increases the efficiency of steam generation.[225] On this premise, the immobilization of NPs on the surface of membranes is considered a promising approach to effective solar harvesting and conversion into thermal energy for a wide range of practical applications. Floating membranes directly placed on the feed seawater surface, exhibiting suitable sunlight absorption and persistent capillary flow of water to the heat source, are among the most investigated photothermal systems.[228]

In a static photothermal system, the water vapour released at the surface of the floating membrane exposed to air is typically condensed on a transparent cover (Fig. 10a and b).[229] The housing design must promote fast dropwise condensation to prevent the head space from being saturated with water vapor, since a highly humid environment leads to a drastic reduction of the driving force for evaporation. As an additional drawback, the formation of droplets on the condensing surface causes light reflection and scattering that reduce the efficiency of the light absorber.

In this regard, efforts have been focused on creating superhydrophobic nanotextured surfaces to limit droplet adhesion and increase water repellence (Fig. 10c).[230] The roughness of a hydrophobic solid surface enhances its hydrophobicity according to the Wenzel model with the fluid wetting all of the rough surface area,[231] or according to the Cassie model with the droplet resting on the tips of the surface asperities.[232] Aili *et al.* (2017) attributed the increase of the nucleation rate of water droplets to the decreased energy barrier in confined cavities (Fig. 10d).[233]

In general, the adoption of floating membranes in static solar evaporation systems suffers from additional limitations due to the lack of fluid-dynamics control. The absence of tangential flow at the membrane surface drastically reduces the mass

Table 7 Performance of nanofluids in terms of evaporation efficiency (η) and mass flow rate of vaporized water ($\dot{m}$). P_{in} is the power of the incident light

Photothermal material	Configuration	η (%)	$\dot{m}$ (kg m^{-2} h^{-1})	P_{in} (kW m^{-2})	Ref.
rGO–Fe_3O_4	Volumetric	70	2.5	2	220
Au	Volumetric	65	6.3	10	225
Au	Volumetric	36	0.6	1	226
Au	Interfacial	52	0.8	1	226
Au-Cored C	Interfacial	33.8	n.a.	5.1	227
Fe_3O_4/C	Interfacial	n.a.	2.3	1.4	224

n.a.: data not available.

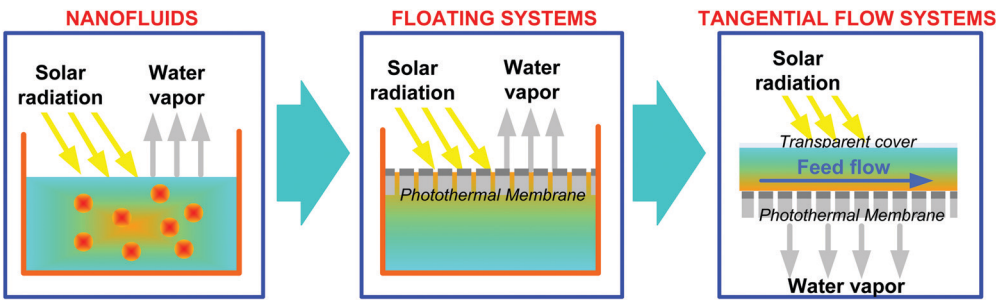

Fig. 9 The evolutionary pathway of photothermal evaporation.

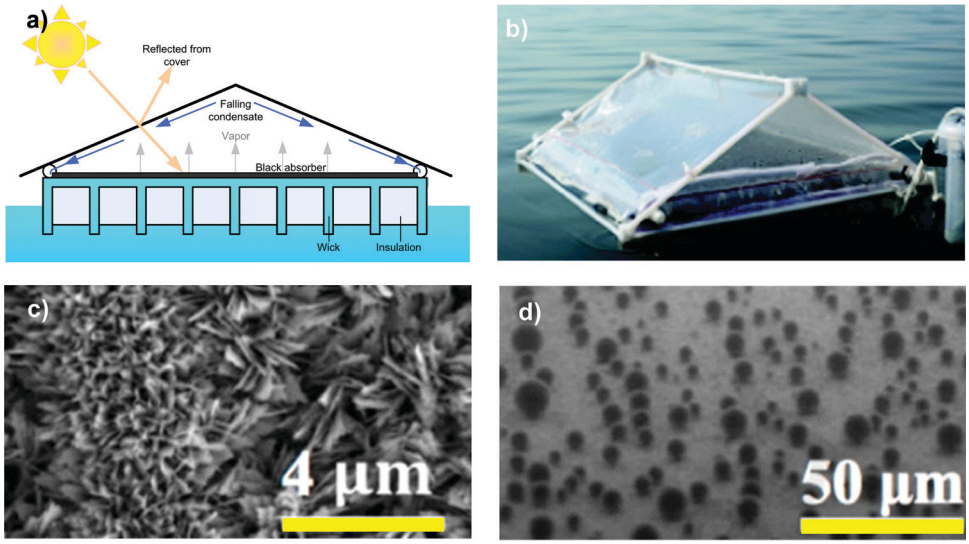

Fig. 10 (a) Illustration of the floating evaporation structure in a fabricated polymer-film based condensation cover; (b) device operating in the ocean. Adapted from ref. 229 by permission of The Royal Society of Chemistry; (c) SEM image of the super-hydrophobic nanostructured condensing surface; (d) nucleation of water droplets. Reprinted (adapted) with permission from ref. 233. Copyright 2017 The American Society of Mechanical Engineers.

transfer coefficient within the boundary layer adjacent to the floating surface, thus exacerbating the concentration polarization phenomenon (*i.e.*, the increase in concentration of rejected species at the membrane–feed solution interface due to the removal of water). As a consequence, sparingly soluble salts usually present in natural feed waters (mainly $CaCO_3$, $MgCO_3$ and $CaSO_4$) can easily precipitate, resulting in a rapid incrustation and clogging of the membrane (a phenomenon known as "scaling"[22,234]). Static operational conditions also hinder the possibility to locally promote turbulence with the aim to mitigate the occurrence of biofouling due to adhesion, accumulation of dissolved organic matter and microorganisms on the supporting substrates. The impact of scaling and biofouling is expected to be particularly significant for substrates made of cellulose materials with an interconnected porous network, where the blockage of hydrophilic channels would stop the transport of water to the photothermal layer *via* the capillary force.[235]

4.2 Photothermal membrane distillation (PMD)

In order to overcome the limitations of floating photothermal evaporation systems, and to push lab-scale applications of photothermal membranes towards technology demonstration in an industrially relevant environment, R&D activities have recently focused on dynamic operations under tangential flow for continuous processing, and on modular systems implementing different configurations (see Section 2.1) for large productivity, easy scale-up and efficient heat recovery.[236]

In PMD, the photothermal active layer provides a localized heating at the membrane surface that reduces or eliminates the external energy input required for heating the feed. The enhancement of temperature at the feed solution interface drastically reduces or reverses the temperature polarization phenomenon, leading to a highly efficient evaporation process (see Section 2.3).

At steady-state, the evaporative heat flux associated with the transport of water vapor through the membrane (transmembrane flux) is given by the difference between the absorbed radiative flux (Section 4.2.1) and heat fluxes across: (i) the boundary layer at the feed–membrane interface (Section 4.2.2); (ii) the membrane (Section 4.2.3); and (iii) the boundary layer at the distillate–membrane interface (Section 4.3).

The heat transfer mechanisms involved in PMD are:

(i) convection (q_{conv}) through a moving fluid (liquid or gas), occurring because the surface temperature of the membrane (T_m) is different from that of the surrounding fluid (T_∞):

$$q_{conv} = h(T_\infty - T_m), \quad (23a)$$

where h is the convective heat transfer coefficient (W m^{-2} K^{-1});

(ii) conduction (Q_{cond}) through a medium under a temperature difference ΔT:

$$q_{cond} = \frac{k}{\delta} \cdot \Delta T, \quad (23b)$$

where k is the thermal conductivity coefficient (W m^{-1} K^{-1}) and δ is the thickness of the medium;

(iii) radiation (q_{rad}), *i.e.*, the emission of electromagnetic waves from matter with a nonzero absolute temperature (*i.e.*, the membrane):

$$q_{rad} = \varepsilon \cdot \sigma(T_m^4 - T_\infty^4), \quad (23c)$$

where ε is the emissivity of the membrane in the fluid, and σ the Stefan–Boltzmann constant (5.67×10^{-8} W m^{-2} K^{-4}).

The specific configurations adopted to reduce the partial pressure on the distillate side (options listed in Section 2.1 for conventional MD) are discussed in Section 4.3 for PMD applications.

It is worth pointing out that a passive multistage system, realized using dead-end water or water wicking through the

hydrophilic layer as the feed water supply, are here not categorized as PMD systems since they do not exhibit the peculiar requisites of modularity for a reliable process scale-up, neither tangential-flow operability for a feasible synergic integration with other membrane processes.

4.2.1 Maximizing light harvesting. Light harvesting efficiency depends on the ability of photothermal materials to increase the light absorption and to reduce light reflection. Research efforts have addressed the development of photothermal membranes with superior light absorption in order to enhance the absorbed radiative flux (Q_{abs}), defined as:

$$Q_{abs} = \alpha I, \quad (24)$$

where α is the absorptance and I the irradiance. Specifically, the solar absorptance as a function of the incident angle of light (θ) and wavelength (λ) is determined by the ratio of the total absorbed solar radiation to the incident radiation:[237]

$$\alpha = \frac{\int_{\lambda_{min}}^{\lambda_{max}} I(\theta,\lambda)[1 - R(\theta,\lambda)]d\lambda}{\int_{\lambda_{min}}^{\lambda_{max}} I(\lambda)d\lambda}, \quad (25)$$

where λ_{min} and λ_{max} are 300 and 2500 nm, respectively, and $R(\theta, \lambda)$ is the reflectivity function of the membrane.

In this regard, noble-metal (Ag, Au) NPs immobilized in/on the membranes have been widely used for stream solar generation. Membranes with Au nanofillers deposited on their surface *via* vacuum-assisted flocculation exhibited sunlight absorption as high as ~90% and an efficiency of~ 62.5% under 1 sun (1 sun = 1 kW m^{-2});[238] here, the anchoring of NPs was promoted by pre-treating the membrane with poly-diallyl dimethyl ammonium chloride (PDDA) solution, so that positively charged functional groups fixed on the polymeric support were able to attract the negatively charged Au NPs.[238] Black Ag nanostructures are particularly efficient systems for absorbing and converting solar energy into heat.[239] The assembly of Ag NPs in rod-shape with widely distributed interparticle distances *via* seeded growth confined on ellipsoidal iron oxyhydroxide nanorods led to broadband absorption in the visible and near-IR spectrum.[239]

Al–Ti–O (aluminum–oxygen–titanium) semiconductor NPs, easily produced by top-down approaches such as planetary milling of low-cost precursors (*i.e.*, TiO_2 and Al powder) and dispersed in a PVDF membrane, showed a solar absorption of *ca.* 90% with a water vapor flux of 0.5 kg m^{-2} h^{-1}; it was also observed that the presence of Al positively affects the localized surface plasmon resonance of Ti.[240] Moreover, an ultrathin porous photothermal film based on 2D transition metal dichalcogenide MoS_2 nanosheets and SWCNTs exhibited an absorption higher than 82% over the whole solar spectrum range; with a temperature at the evaporative interface as high as 50 °C, the transmembrane flux reached 6.6 kg m^{-2} h^{-1} in air.[190]

With regard to carbon-based materials, single-wall CNTs deposited on a filter paper exhibited high broadband absorption (>90%) in the solar light spectra, resulting in a vapor generation rate of 3.6 kg m^{-2} h^{-1} under a solar power of 5 sun and evaporation efficiency above 40%.[241]

It is worth mentioning the promising strategy consisting of the exploitation of the synergistic benefits of different photothermal materials.

A photothermal layer resulting from the combination of 2D rGO and 1D MWCNTs, applied to a PVDF substrate, improved the evaporation rate by 79% and 8.9% with respect to that of bare rGO and MWCNT membranes, respectively.[242] Membranes derived from carbonized egg-shell in combination with CNTs exhibited superior performance with respect to the functionalization with r-GO, showing an absorption of 99% in the IR-Vis-NIR region and a water vapour flux of *ca.* 1.3 kg m^{-2} h^{-1}.[243]

The maximization of absorbance properties of photothermal materials can be complemented with the advanced design of morphological architectures at the photothermal surface with the aim to reduce the light reflection and the consequent energy loss. Intuitively, an increase of the optical path of the incident photons due to Lambertian scattering can lead to efficient recycling of reflected light for higher light harvesting efficiency. In this regard, main research lines include the design of photothermal devices based on macroscopic and microscopic structures. Practical interest of macroscopic structures, evolved from simple cylindrical and cone-like structures to more complex and elegant origami, is limited to static photothermal systems due to the relatively large size (in the order of centimeters) of the 3D assemblies. Shi *et al.*[244] developed a cylindrical 3D cup-shaped photothermal structure (with the diameter and height of the wall as 4.7 and 5 cm, respectively) capable of recovering diffuse reflectance to ambient air; the composite, fabricated using $CuFeMnO_4$ NPs – selected among mixed metal oxide (MMO)-type inorganic pigments – and a quartz glass fibrous filter membrane, reached near 100% energy efficiency with evaporation rate of 2.04 kg m^{-2} h^{-1} under one-sun illumination. According to Wang and coworkers,[245] 3D photothermal cones with a tunable apex angle were able to achieve an absorbance of up to 99.2% within the solar spectrum and evaporation rate of up to 1.70 kg m^{-2} h^{-1} under 1 sun illumination, corresponding to 93.8% solar conversion efficiency, which is about 1.7 times as high as the result obtained for a corresponding plane film. The light-trapping effect in a periodic concavity pattern was also observed for a 3D origami-based nanocarbon composite of GO and NTs designed on a Miura-ori tessellation, that reached a solar energy efficiency close to 100% under 1 sun illumination in a highly folded configuration.[246]

On the other side, the fabrication of micrometric anti-reflective structures on the surface of photothermal membranes – *via* hierarchical chemical functionalization or physical methods – can be potentially effective for improving their evaporation efficiency in PMD applications. 2D nanosheets of graphdiyne (GDY), a highly π-conjugated structure of sp- and sp^2-hybridized C with a narrow band gap (0.46 eV) for an optical absorption window extending to ~2700 nm, were fully decorated on the surface of 1D vertical CuO nanowires and supported on copper foam (CF). The ability of this 3D hierarchical architecture (Fig. 11a) to trap light by increasing its traveling distance inside the materials increased the solar absorption by 8%; moreover, under an irradiation density of 5 kW m^{-2}, the temperature of GDY/CuO CF reached an equilibrium value of about 126 °C,

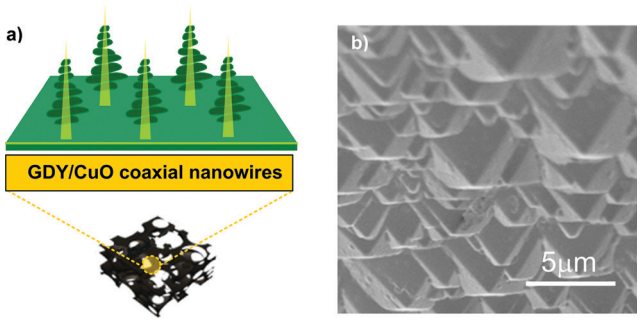

Fig. 11 (a) Schematic illustration of graphdiyne/CuO-based multidimensional architecture. Reprinted (adapted) with permission from ref. 247. Copyright 2017 American Chemical Society. (b) The SEM images of the inverted pyramids of the photothermal membrane. Adapted from ref. 248 by permission of The Royal Society of Chemistry.

i.e., 18 °C higher than that detected for the CuO nanowire substrate.[247]

Sun *et al.* fabricated an inverted pyramid structure with anti-reflective ability on the surface of a hydrogel loaded acetylene carbon black photothermal material by using a Si wafer template (Fig. 11b): as a result of its anti-reflective ability, the surface temperature of the photothermal membrane with inverted pyramids reached 49.4 °C after being irradiated under 1 sun for 30 min, that is 4.3 °C higher than the temperature measured on the flat surface.[248]

Moreover, a relevant aspect in maximizing light harvesting is that the light-to-heat conversion efficiency of photothermal membranes differs in the "dry" and "wet" states. The Fresnel equation,[249] expressing the reflectivity (R) of light at the interface between two homogeneous media with refractive indices n_1 and n_2, provides a useful theoretical background to screen the optimal photothermal substrates:

$$R = \left(\frac{n_1 - n_2}{n_1 + n_2}\right)^2 \tag{26}$$

According to eqn (15), reflection losses are strongly reduced if the photothermal material possesses the same refractive index as the surrounding media. While the refractive index of air is 1, in the "wet state" case the presence of water (having a refractive index of about 1.33 in the optical range) should be accounted for. Consequently, both the scattering properties (reflection, transmission and absorption) and the efficiency of light-to-heat conversion change. Considering that the refractive indices of most amorphous polymers of interest for PMD fall between 1.35 and 1.55[250] it is expected that, in the "wet" state corresponding to the characteristic PMD configuration of the feed solution contacting the photothermal membrane surface, the refractive index matching increases and, correspondingly, the light reflection decreases and the absorption increases.

4.2.2 Heat transfer within the feed/membrane thermal boundary layer. In PMD, the aqueous feed stream is recirculated tangentially to the surface of the photothermal membrane. Due to the temperature difference between the bulk of the feed solution (T^f_∞) and the membrane interface (T^f_m), a thermal boundary layer adjacent to the membrane interface develops. Here, energy is transferred *via* thermal forced convection according to eqn (23a) and – to a lesser extent – *via* radiation according to eqn (23c). In conventional MD (see Fig. 2a), the transversal profile of temperature decreases within the boundary layer in the direction that goes from warm feed to the membrane ($T^f_\infty > T^f_m$), thus determining a reduction of the driving force to evaporation since it takes place at the membrane interface. In order to reduce this negative effect (temperature polarization), the feed flow rate is increased since a high Reynolds number improves the heat transfer coefficient h according to empirical correlations expressed in terms of dimensionless numbers in the following generic form:

$$\mathrm{Nu} = a \cdot \mathrm{Re}^b \cdot \mathrm{Pr}^c \cdot (d_h/L)^d \tag{27a}$$

$$\mathrm{Nu} = \frac{h \cdot d_h}{k} \tag{27b}$$

$$\mathrm{Re} = \frac{\rho \cdot v \cdot d_h}{k} \tag{27c}$$

$$\mathrm{Pr} = \frac{c_p \cdot \mu}{k} \tag{27d}$$

where Nu is the Nusselt number (*i.e.*, the ratio of convective to conductive heat transfer, determining the value of the convective heat transfer coefficient h), Re is the Reynolds number (*i.e.*, the ratio of inertial to viscous forces, determining the impact of fluid-dynamics of the heat transfer rate), Pr is the Prandtl number (*i.e.*, the ratio of momentum to thermal diffusivity), d_h is the hydraulic diameter, k is the thermal conductivity of the fluid, ρ is the density, v is the velocity, c_p is the specific heat, and μ is the dynamic viscosity. In eqn (27a), exponents a, b, c and d are commonly available in the literature for different thermal convection mechanisms (forced or natural), fluid-dynamic conditions (laminar or turbulent flow) and system geometries.[251]

Conversely, in PMD, the incorporation of photothermal NPs at the membrane interface determines, under light irradiation, an inverse temperature profile transversally to the boundary layer (see Fig. 2b), with $T^f_m > T^f_\infty$. Therefore, this requires that the convective heat flux be minimized to reduce heat losses from the membrane surface towards the bulk of the feed solution. In this regard, low feed flow rates (Re in the order of 10^2) determine low values of h and, hence, higher evaporation rates, while guaranteeing an adequate control over concentration polarization and fouling phenomena. Experimental evidence of these deductions is offered by Wu *et al.*, who observed an increase of the trans-membrane flux from 0.43 kg m^{-2} h^{-1} to 0.57 kg m^{-2} h^{-1} when the feed flow rate decreased from 8.1 to 1.5 mL min^{-1}.[252]

The extreme situation of zero feed flow rate reduces PMD to a static photothermal evaporation system (free convection), thus suffering from limitations previously discussed (Section 4.1). It is worth pointing out that, for free (natural) convection, the Nusselt number is expressed as a function of Prandtl number and Grashof number (Gr) – *i.e.*, the ratio of buoyant to viscous forces – defined as:

$$\mathrm{Gr} = \frac{g \cdot \beta \cdot \Delta T \cdot L^3}{\nu^2} \tag{28}$$

where g is gravitational acceleration, β is the coefficient of thermal expansion, ΔT is the characteristic temperature difference (for the specific situation, that between the photothermal membrane surface and the bulk of surrounding fluid), L is the characteristic length, and ν is the kinematic viscosity. While the convective heat transfer coefficient of water usually ranges from 500 to 10 000 W m^{-2} K^{-1} depending on the operational conditions, typical intervals of h for air in free and forced convection are in the range of 2.5–25 and 10–500 W m^{-2} K^{-1}, respectively.[248]

The idea of using spacers (usually employed in membrane modules to promote turbulence in feed channels) to induce photothermal conversion in proximity of the membrane surface, deserves a particular mention.[253] Adoption of metal spacers made of Ni and coated with photocatalytic Pt led to a reduction of up to 28% in energy per unit volume of distillate under light irradiation with respect to DCMD carried out with conventional polymeric spacers.[253]

In addition to heat loss by convection, the amount of energy leaving the system by thermal radiation can represent a significant parasitic loss: considering the dependence on T^4 in eqn (23c), the radiative heat loss is 680 W m^{-2} (one-sun illumination) assuming a black solar absorber ($\varepsilon = 1$) at 100 °C and an air temperature of 20 °C.

The electromagnetic solar radiation mostly extends from 290 to 3200 nm, with radiation energy distribution non-uniformly spread among ~2% in the UV region, ~47% in the visible region and ~51% in the infrared (IR) region.[254] On the other hand, the blackbody radiation spectrum extends over a broader wavelength region. For a nonselective thermal radiator, Kirchhoff's law states that – at any temperature and wavelength – the spectral directional emittance (ε) is equal to the spectral absorbance (σ) for radiation incident from the same direction.[255] Therefore, an effective strategy to minimize thermal radiation heat loss is to use selective light absorbers (typically categorized as multi-layer thin film coatings, plasmonic nanostructures and carbon-based materials) that should ideally eliminate the transmittance and reflectance.

Lu *et al.*[256] fabricated a patterned film absorber (Fig. 12a) comprising an ultrathin Ge film (Fig. 12b) and a reflective Au layer by laser interference lithography. In Fig. 12c, simulation results reveal that the optimized bilayer system (Ge/Au) can reach a total solar absorptance of 84.1% between 400 and 1100 nm.

A spectrally selective solar absorber, consisting of a cermet (BlueTec eta plus) with a solar absorptance of 0.93 and an emittance at 100 °C of 0.07, was coated on a copper sheet; with respect to a blackbody absorber, the radiative heat loss was reduced by one order of magnitude.[258]

Lin *et al.*[257] coated a 30 nm-thick structured graphene metamaterial (SGM) – consisting of alternating graphene and dielectric layers – on a 3D trench-like copper substrate (Fig. 12a). The resulting hybrid nanostructure, designed in such

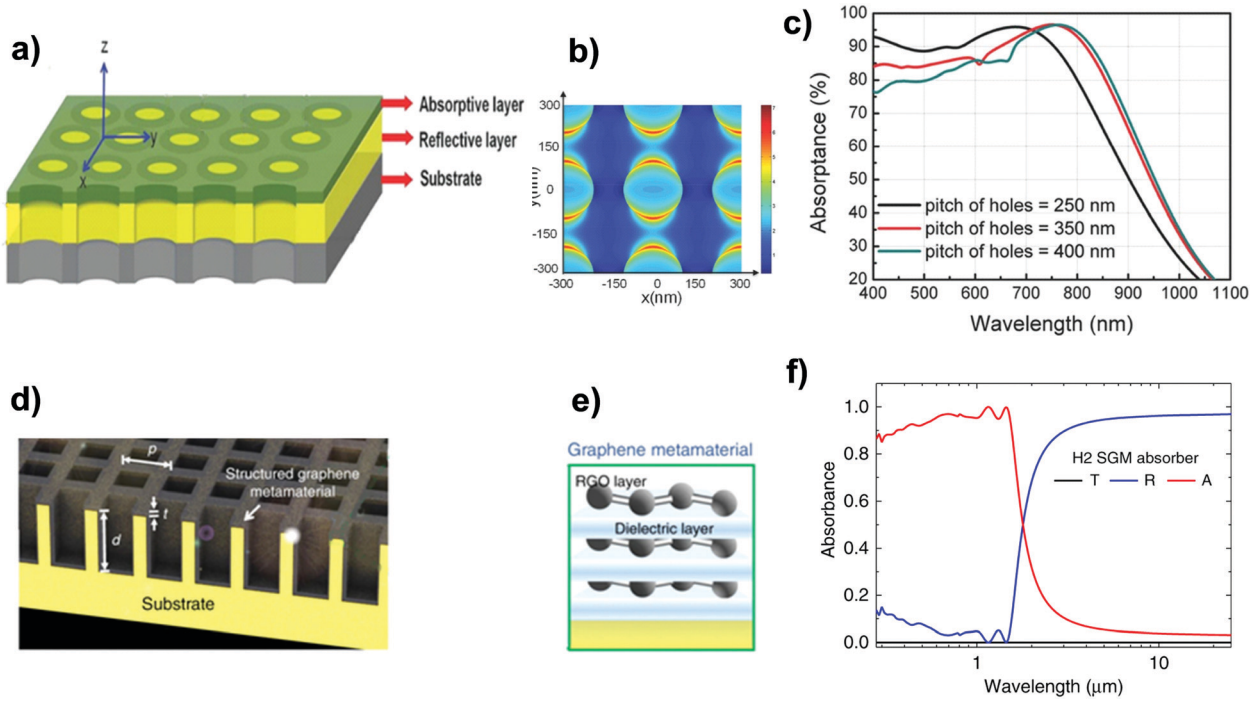

Fig. 12 (a) Schematic representation of the plasmonic enhanced ultrathin film absorber with nanoporous patterns consisting of an absorptive layer and a reflective layer deposited on a substrate; (b) top view of energy flow distribution in the Ge layer; (c) simulated absorptance as a function of distance between nanoholes. Reprinted (adapted) with permission from,[256] John Wiley and Sons. (d) Schematic representation of the 3D SGM absorber (*d*: depth of trenches, *t*: thickness of the graphene metamaterial layer, *w*: width of the hole, and *p*: period of the structure). (e) Structure of the graphene metamaterial. (f) Simulated spectral reflectance (*R*), transmittance (*T*), and absorbance (*A*) for the SGM absorber (d = 1 μm, t = 30 nm, w = 0.59 μm, p = 0.8 μm). Reproduced from ref. 257 (Creative Commons Attribution CC BY, Copyright 2020, Springer Nature).

a way that it should have the C_4 rotational symmetry to realize polarization-independent absorption, was able to achieve a near-unity absorption across the UV and NIR spectral ranges while suppressing almost completely the absorbance in the IR regime due to the strong interference phenomena (Fig. 12c). The SGM absorber reached a solar-to-vapor efficiency of 96.2% and a water evaporation rate of 1.5 kg m^{-2} h^{-1}.[257]

In principle, radiative heat loss can be effectively reduced by decreasing the surface temperature exposed to light radiation. A study by Li *et al.*[259] proved that, despite the lower surface temperature (32.7 °C) compared to the other configurations (39.5 °C for 2D direct contact evaporator, and 43.0 °C for 2D indirect contact evaporator), a 3D umbrella-like system exhibited the highest solar steam efficiency (85%) due to the consequent reduction of heat losses towards the environment.

However, the effectiveness of this approach is questionable since a low working temperature deteriorates the transmembrane water vapor flux (driven by a vapor pressure gradient, whose intensity depends exponentially on temperature). Beyond the interest of a comprehensive understanding of the heat transfer phenomena occurring in photothermal systems for solar evaporation, these creative solutions are of no practical use for PMD.

4.2.3 Heat transport within the membrane: minimizing the conductive heat loss. According to eqn (4), the total heat flux through the membrane includes two terms: the convective heat flux in the form of latent heat associated with the net flux of water vapor molecules moving from the feed side to the opposite distillate side (the higher this term, the greater the evaporation efficiency of the system according to eqn (22a), and the conductive heat flux across the membrane. The latter, represents not only a loss of efficiency since this portion of energy is not exploited for water evaporation, but has an additional negative impact of increase of temperature at the membrane/distillate interface and the consequent decrease of the driving force to mass transfer.

In order to determine the effective thermal conductivity of composite materials or layers ($k_{c,eff}$) made by dispersing nano-fillers within a matrix, several empirical models have been proposed in the literature.[260] For filler volume fractions up to 40%, the Lewis–Nielsen mathematical model provides relatively good results for a wide range of NP shapes:

$$k_{c,eff} = \frac{1 + A \cdot B \cdot \phi_f}{1 - B \cdot \psi \cdot \phi_f} \quad (29a)$$

$$B = \frac{k_f/k_s - 1}{k_f/k_s + A} \quad (29b)$$

$$\psi = 1 + \left(\frac{1 - \phi_m}{\phi_m{}^2}\right)\phi_f \quad (29c)$$

where k_s is the thermal conductivity of the support material, k_f is the thermal conductivity of the photothermal filler, ϕ_f is the filler volume fraction, ϕ_m is the maximum filler packing fraction, and A is the shape coefficient for the filler particles (Table 8).

Table 8 Maximum packing fraction (ϕ_m) and values of A for different shapes of the fillers and type of packing[260]

Shape	Type of packing	φ_m	NP aspect ratio (length/diameter)	A
Sphere	Face-centered cubic	0.7405	1	1.5
	Body-centered cubic	0.6		
	Simple cubic	0.524		
	Random close	0.637		
	Random loose	0.601		
Rods	Uniaxial hexagonal close	0.907	2	1.58
	Uniaxial simple cubic	0.785	4	2.08
	Uniaxial random	0.82	6	2.8
	Three-dimensional	0.52	10	4.93
	Random		15	8.38

Finally, the thermal conductivity of the membrane (k_m) can be estimated as a function of the effective thermal conductivity of the photothermal composite ($k_{c,eff}$) and of the fluid (k_{fluid}) filling the pores, according to the following relationship:[66]

$$k_m = (1 - \varepsilon_p)\cdot k_{c,eff} + \varepsilon_p \cdot k_{fluid} \quad (30)$$

where ε_p is the porosity. Depending on whether the membrane is hydrophobic or hydrophilic, it is filled by air (0.024 W m^{-1} K^{-1}) or water (0.617 W m^{-1} K^{-1}), respectively.

Mitigation of conduction heat loss is critical in MD, where the required hydrophobicity of the membrane is achieved by using polymers (*i.e.*, PFTE, PVDF, and PP) exhibiting a relatively high thermal conductivity (see Table 9). This situation is further exacerbated by the incorporation of photothermal materials.

An increase of the membrane thickness reduces the thermal conductivity flux across the membrane (eqn (23b)); however, this positive effect is counterbalanced by the higher resistance to mass transport. Therefore, the most effective option to reduce the conductive heat loss is to support the photothermal layer with a thermally insulating layer (low k_m in eqn (23b)). Recently, a large variety of materials have been explored for the realization of an additional thermally insulating layer in composite membranes, including polymers or carbon-based foam, cotton, wood, aerogels and hydrogels (Table 9).

On these premises, we focus our attention on homogeneous hydrophobic photothermal membranes (Section 4.2.4), with the photothermal material uniformly dispersed in the hydrophobic polymeric matrix, and on more energy-efficient composite hydrophilic/hydrophobic photothermal membranes (Section 4.2.5).

4.2.4 Homogenous hydrophobic photothermal membranes. Homogeneous hydrophobic membranes show the relevant advantage of an easy and potentially scalable preparation method: as the photothermal material is dispersed within the polymeric solution, conventional phase separation methods can be applied for the production of a large membrane surface area (Fig. 13).

The first photothermal membrane for MD application was reported by Politano *et al.* (2017); here, Ag NPs were dispersed in a solution of PVDF in DMF. Localized thermal hotspots, activated under UV irradiation at a wavelength of 366 nm, resulted in an increase of temperature at the membrane surface even greater than 23 K with respect to the bulk value.[278]

Table 9 Thermal conductivity of materials commonly used in the manufacture of photothermally-enhanced membranes

Photothermal material	Category	Thermal conductivity (W m^{-1} K^{-1})	Ref.
Graphene film	Carbon	1000–3000	261
Vertically aligned graphene	Carbon	100–600	
Graphene foam	Carbon	<2 (pristine) 90 (compressed)	
Ag	Metal	429	262
Au	Metal	318	263
MWCNT film	Carbon	244–267	264
MWCNT	Carbon	12–17	
MoS_2	Semiconductor	34.5	265
$CuFeS_2$	Semiconductor	5.9	266
Polypyrrole	Polymer	~0.7–1	267
Support material		**Thermal conductivity (W m^{-1} K^{-1})**	**Ref.**
Mixed cellulose esters		0.565	268
Polyurethane		0.5182	269
PTFE		0.25–0.27	85
PVDF		0.17–0.19	
PP		0.11–0.16	
MWCNT array		0.145	264
Wood		0.11-0.35	235
Cellulose aerogel		0.06	270
Polymer foam		0.057	271
Cotton rod		~0.04	272
Polystyrene foam		~0.04	273
Air-laid paper		0.03–0.05	274
Cellulose paper		0.031	275
Cellulose-membrane		0.02	181
Polyacrylonitrile (PAN) electrospun nanocomposite fibers		0.02	276
Graphene oxide aerogel		0.0047–0.035	277

Flat-sheet microporous membranes consisting of black Al–Ti–O nanohybrid structures[240] showed an evaporation rate (with pure water as the feed) of 1.03 kg m^{-2} h^{-1} with a corresponding thermal efficiency of ~77%.

In porous HCuPO (40%)–PDMS films in contact with 3.5% NaCl aqueous solution an evaporation rate of 1.01 kg m^{-2} h^{-1} and a thermal efficiency of 63.6% under one sun[279] were observed.

The most critical drawback of homogeneous membranes is that a large part of the photothermal material, incorporated within the interior part of the membrane not exposed to light irradiation, is not effectively used. Moreover, the uniform dispersion of nanofillers increases the thermal conductivity of the whole membrane, leading to high conductive thermal losses.

To overcome these limitations, bi- and multi-layered membranes have been developed at the unavoidable cost of introducing complexity in the manufacturing procedure.[280]

4.2.5 Bi- and multi-layered photothermal membranes

Membranes made of metal-based photothermal materials on a polymeric support. Au NPs with a particle size of 30–40 nm were immobilized by filtration on a PVDF membrane with asymmetric wettability, prepared *via* the phase inversion method within a coagulation bath comprising hydrophilic copolymer poly-vinylpyrrolidone-vinyltriethoxysilane (PVP-VTES).[281] The thermal conductivity of the hydrophobic side of the membrane was 0.026 W m^{-1} K^{-1}, thus determining a low conductive loss (between 13.4 and 17.0% depending on the orientation of the device). The composite membrane exhibited opposite wettability, with the hydrophilic top layer with spherical structures and the bottom surface with a flower-like structure characterized by a contact angle of 142–145° (Fig. 14a–c).

Zhao *et al.* (2018) fabricated a composite MXene membrane by depositing 2D delaminated d-Ti_3C_2 nanosheets, and made it hydrophobic by chemical modification with trimethoxy-(1*H*,1*H*,2*H*,2*H*-perfluorodecyl) silane (PFDTMS), on a mixed cellulose ester filter.[282] A steady-state temperature of *ca.* 39 °C was measured on the membrane surface; the distillation performance was stable over 200 hours of continuous operation.

Nanowires represent another interesting category of photothermal materials, enabling the penetration of the exciting

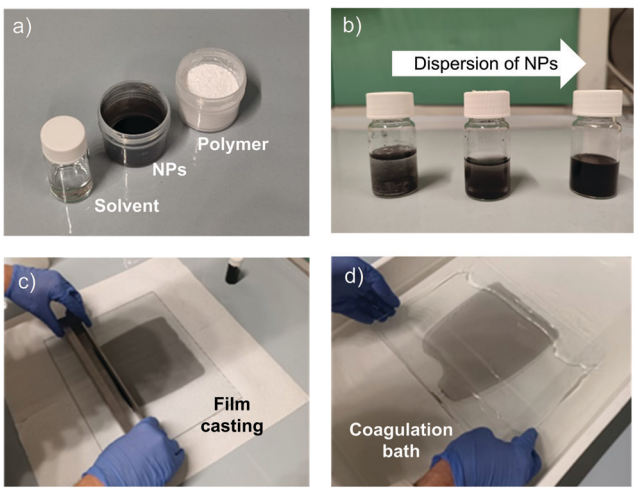

Fig. 13 Preparation of homogeneous membranes *via* non-solvent induced phase separation (NIPS): (a) materials, (b) preparation of the polymeric solution, (c) casting of the polymeric solution, (d) NIPS induced by the coagulation bath.

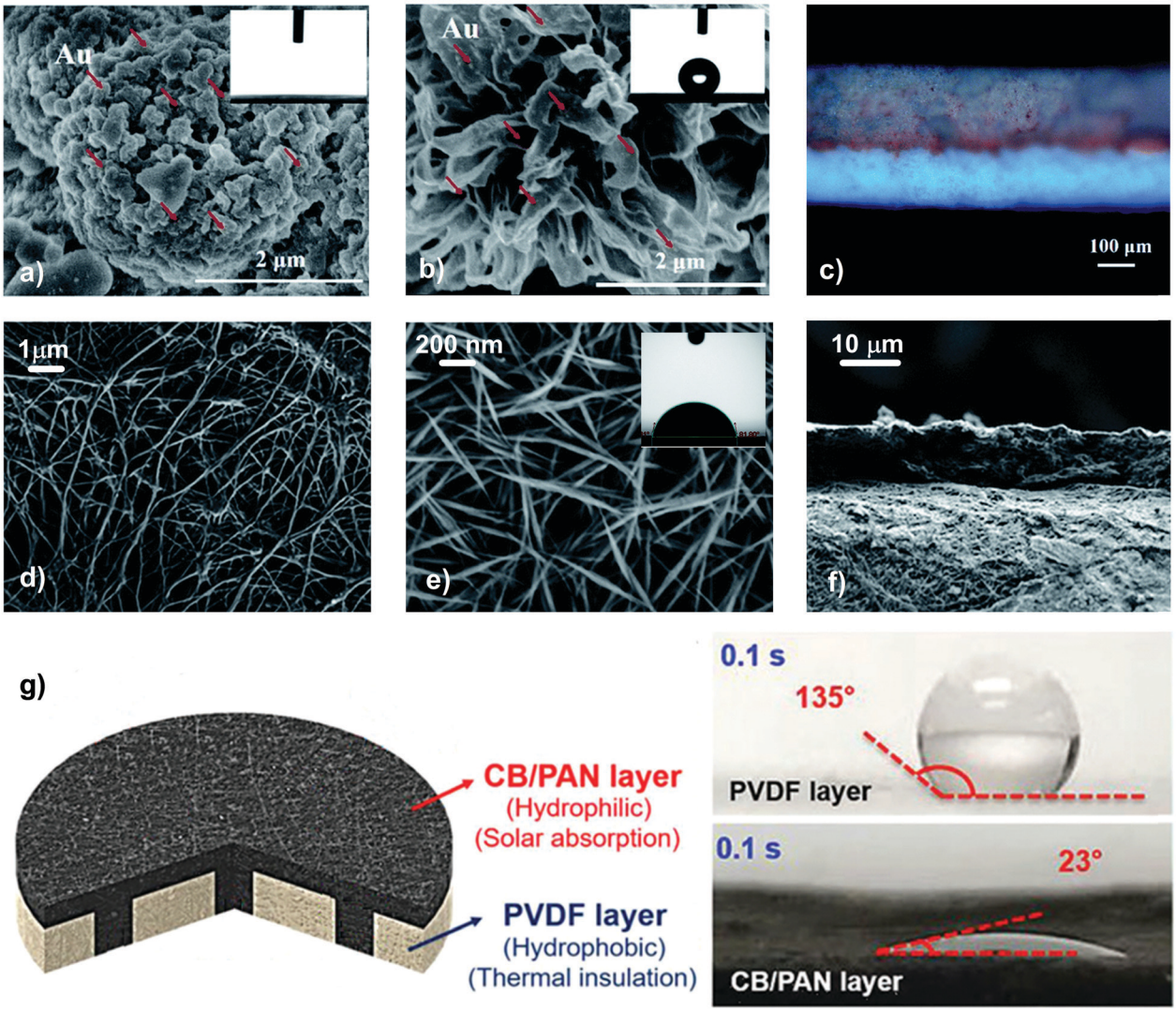

Fig. 14 SEM micrographs of the Au NPs/PVDF composite membrane: (a) top layer with the spherulitic structure showing almost zero water contact angle; (b) bottom layer with a flower-like morphology exhibiting a contact angle of ~140°; (c) cross-sectional image of the by-layered structure. Adapted from ref. 281 with permission from Royal Society of Chemistry. SEM micrographs of the $W_{18}O_{49}$@PDMS/PTFE composite membrane: (d) PTFE hydrophilic support; (e) $W_{18}O_{49}$@PDMS mesocrystals at the top layer; (f) cross-sectional image of the by-layered structure. Adapted from ref. 287 with permission from Royal Society of Chemistry. (g) Schematics of the bi-layered hydrophilic CB/PAN – hydrophobic porous PVDF membrane and contact angles of the PVDF and CB/PAN nanofiber layers. Reprinted (adapted) from ref. 288 with permission from John Wiley and Sons.

electric field in the confined geometries,[283,284] with Green's dyadic function estimating a +60% change in the heating efficiency by shifting the Au NP morphology from spherical to elongated nanorods.[285] Pt–Ni–S nanowires, having high light absorption capacity in the whole spectral region between 200 and 2500 nm, were poured onto a commercial PTFE membrane and then dried; after the chloroalkylsilane modification method, the membranes exhibited a water contact angle of 106°.[286] The best performance, registered for a Pt3Ni–S NW solution concentration of 21.6 mg mL^{-1} deposited on PTFE membrane, resulted in a water evaporation rate of 1.27 kg m^{-2} h^{-1} and a thermal conversion efficiency of ~80%.

Membranes made of semiconductor photothermal materials on a polymeric support. A bi-layered solar steam generator was developed by immobilizing non-stoichiometric $W_{18}O_{49}$ mesocrystals on a PTFE membrane using PDMS as a binder (Fig. 14d–f). The mesocrystals showed a broad absorption band of 550–2500 nm, whereas PDMS acted as a hydrophobic modifier guaranteeing self-floating properties; the system was able to generate 1.15 kg m^{-2} of steam after 1 h under one-sun irradiation, with efficiency reaching 82%.[287]

Beside their potential use for solar stream generation and desalination, photothermal membranes are of interest in a wide range of applications, such as wastewater treatment or pasteurization. The combination of plasmonic Au NPs with hedgehog-like ZnO particles acting as the photocatalyst on the surface of a cellulose ester hydrophilic support (contact angle of *ca.* 70°) resulted in a super-hydrophobic membrane (top layer water contact angle of *ca.* 155°) able to synchronize the process

of stream generation with photodegradation. Specifically, the presence of Au NPs allowed the tripling of the rate of water evaporation whereas ZnO favoured the degradation under solar photocatalysis of 30% of an organic dye contaminant (*i.e.*, Rhodamine B).[289]

Membranes made of carbon-based photothermal materials on a polymeric support. In MD and PMD, the non-wetting properties of a composite membrane are satisfied by the presence of a single hydrophobic layer. A Janus membrane fabricated *via* the electrospinning technique and formed by a hydrophobic layer made of carbon black NP (CB)-coated polymethylmethacrylate (PMMA) for light harvesting, supported by a low-thermally conductive bottom hydrophilic polyacrylonitrile (PAN) layer for water uptake, was proposed by Xu *et al.*[290] After 5 min under 6 sun illumination, the temperature of the top layer increased from 27 to 60 °C, while that of the bottom water only increased by 0.4 °C, thus confirming the insulation ability of the PAN layer. Under one-sun irradiation, the measured transmembrane flux was 1.3 kg m^{-2} h^{-1} with an energy conversion efficiency of 72%.

Despite the good performance, the intrinsic detaching problem of electrospinning layers remains challenging, ultimately making the system unsuitable for robust and long-term desalination operation.

Based on a similar concept, but with inverted hydrophilic/hydrophobic properties of the solar absorption/support layers, Gao *et al.*[288] proposed a Janus membrane composed of a hydrophilic carbon black/polyacrylonitrile (CB/PAN) composite nanofiber layer on an electrospun hydrophobic polyvinylidene fluoride (PVDF) support (Fig. 14g). The estimated thermal conductivity of the bilayer membrane under wet and dry conditions was 0.075 and 0.046 W m^{-1} K^{-1}, respectively. As a consequence of the low conductive loss, the steady-state temperature of the top light absorbing layer increased up to 34.3 °C under one-sun irradiation, while the steady-state temperature of the bottom PVDF layer was significantly lower (20.2 °C); under these conditions, an efficiency of 82.0% was achieved.[288]

Membranes made of polymer-based photothermal materials on a polymeric support. Photothermal membranes based on conjugated polymers were developed using PPy as the coating photothermal layer deposited onto the substrates *via* CVDP.[291] The preparation method consisted of dipping the membrane substrate in $FeCl_3$ – used as an oxidizing agent to initiate polymerization – and pyrrole monomer solutions, thus obtaining a layer of PPy. PVDF/PPy-coated membranes exhibited an evaporation rate of 1.41 kg m^{-2} h^{-1} and a solar conversion efficiency of 81.9%.[291]

A Janus membrane was fabricated by coating hydrophobic PPy on the inner pore walls of the PVDF membrane *via* CVDP, and by deposition of hydrophilic polydopamine (PDA) on a single side of the membrane itself.[292] While the PPy-coated sides exhibited a water contact angle (WCA) >120°, the WCA of the opposite membrane side decreased with increasing PDA coverage (a minimum WCA of *ca.* 50° was measured for the highest adopted deposition time of 80 min).

4.3. Design of the distillate compartment and PMD module configurations

As stated in Section 2.1, the driving force that activates the transmembrane flux in the vapor phase is a partial pressure difference between the feed and distillate sides. Moreover, under typical PMD conditions (feed temperature at the interface of photothermal membranes in the range of 60–80 °C), water vapor carries a latent heat of vaporization of about 2400 kJ kg^{-1}. At the distillate side, the particular strategy adopted to lower the partial pressure, to condense the water vapor, to minimize conductive heat loss, and to recover the condensation heat determines the specific configuration of the PMD membrane module (Fig. 15).

The heat transfer mechanisms within the distillate side for photothermal direct contact membrane distillation (PDCMD), photothermal air gap membrane distillation (PAGMD), and photothermal sweeping gas membrane distillation (PSGMD), complementing energy balances in Sections 4.2.2 and 4.2.3, are detailed in Table 10. Temperature profiles reported in Fig. 2b (PDCMD) and Fig. 16a and b (PSGMD, PAGMD) clarify the meaning of the terms of the reported equations.

In the specific case of photothermal vacuum membrane distillation (PVMD), since low vacuum pressure is applied at the distillate side, no boundary layer is considered. Table 11 provides a selection of the most relevant contributions to PMD operated under different lab-scale module configurations; although still in its infancy, the growing number of studies demonstrates the enthusiasm of the scientific community towards this emerging technology.

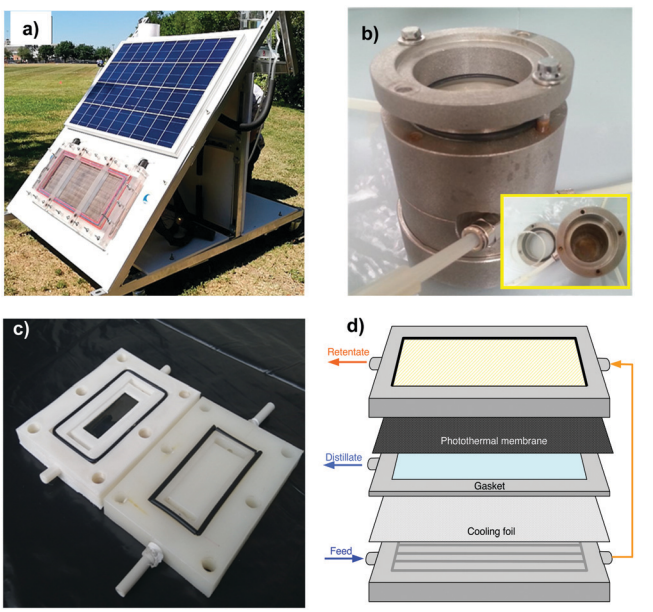

Fig. 15 (a) Prototype equipped with a solar panel to provide electric power for the feed and permeate/vacuum pump in PVMD. Reprinted (adapted) with permission from ref. 293. Copyright 2019 American Chemical Society. Membrane modules employed in lab activities for experiments of (b) PVMD, and (c) PDCMD or PSGMD. (d) Scheme of a membrane module for PAGMD.

Table 10 Heat transfer mechanisms at the distillate side for different PMD configurations

Configuration	Heat flux at the distillate side	Equation
PDCMD	Convective heat flux within the distillate channel	$q_{conv} = h_d\left(T_m^d - T_\infty^d\right)$
PSGMD	Convective heat flux within the coolant channel	$q_{conv} = h_{sweep}\left(T_m^g - T_\infty^g\right)$
PAGMD	Conductive heat flux across the air gap	$q_{cond} = \frac{k_{air-vapor}}{\delta_{air\,gap}}\left(T_m^a - T_{satur}\right)$
	Latent heat flux of water vapor across the air gap	$q_{conv} = J{\cdot}\Delta H_v$
	Conductive heat flux within the condensing film layer (Nusselt theory[260])	$q = h_{Nusselt}\left(T_{satur} - T_{plate}^d\right)$
		$h_{Nusselt} = 0.943\left[\frac{\rho_{liquid}\left(\rho_{liquid}-\rho_{vapor}\right){\cdot}\lambda{\cdot}g{\cdot}k_{liquid}{}^3}{\mu_{liquid}\cdot L_{plate}\cdot\left(T_{satur}-T_{plate}^d\right)}\right]^{0.25}$
	Conductive heat flux across the cooling plate	$q_{cond} = \frac{k_{plate}}{\delta_{plate}}\left(T_{plate}^d - T_{plate}^c\right)$
	Convective heat flux within the coolant channel	$q_{conv} = h_{coolant}\left(T_{plate}^c - T_{cool}\right)$

4.3.1 Photothermal direct contact membrane distillation (PDCMD). In PDCMD, the photothermal membrane is directly in contact with the cold liquid distillate (pure water) recirculated tangentially to the membrane. The main advantage of this configuration is that the water vapor is condensed internally to the module, without the need for an external condenser; conversely, the main drawbacks come from the high conductive thermal loss across the membrane (sandwiched between the hot feed stream and the cold distillate stream), and the consequent occurrence of temperature polarization also at the distillate side, exacerbated by the release of latent heat by the condensing water vapor. Therefore, the use of homogeneous hydrophobic membranes is not appropriate for the PDCMD configuration. In this scenario, the surface modification of pristine MD membranes with photothermal materials was recognized as a flexible and simple route to develop robust coatings achieving photothermal activity. A significant advantage of the surface modification of MD membranes with a photothermal top-layer is the economic viability at large scale, whereas the adhesion and robustness of the coating and the premature release of photothermal materials remain critical concerns.[306]

Polydopamine (PDA), a mussel-inspired polymer characterized by broad light absorption and photothermal conversion behavior combined with hydrophilic character and adhesive properties, was employed for the preparation of a PDA-coated poly-vinylidene fluoride (PVDF) photothermal membrane, subsequently operated in the PDCMD configuration.[252] The coating was prepared *via* self-polymerization, whereas the hydrophobicity of the membrane surface was guaranteed by fluoro-silanization with (tridecafluoro-1,1,2,2-tetrahydrooctyl)-trichlorosilane (FTCS). Using pure water as the feed, the sunlight-driven PDCMD system exhibited – under an irradiation of 0.75 kW m^{-2} – a transmembrane flux of 0.58 kg m^{-2} h^{-1}, a 3.8 fold higher value with respect to the pristine PVDF membrane tested under the same operation conditions. When feeding the PDCMD system with saline water (NaCl 0.5 M), the water flux decreased to 0.49 kg m^{-2} h^{-1} due to the lower vapor pressure of the feed solution.

Analogously, a bilayer structure obtained by freeze-drying a hydrogel made of PDA particles and nanocellulose subsequently grafted with FTCS showed a permeate flux of 1 kg m^{-2} h^{-1} under 1 sun (efficiency of 68%) in the PDCMD process combined with antibacterial activities.[307]

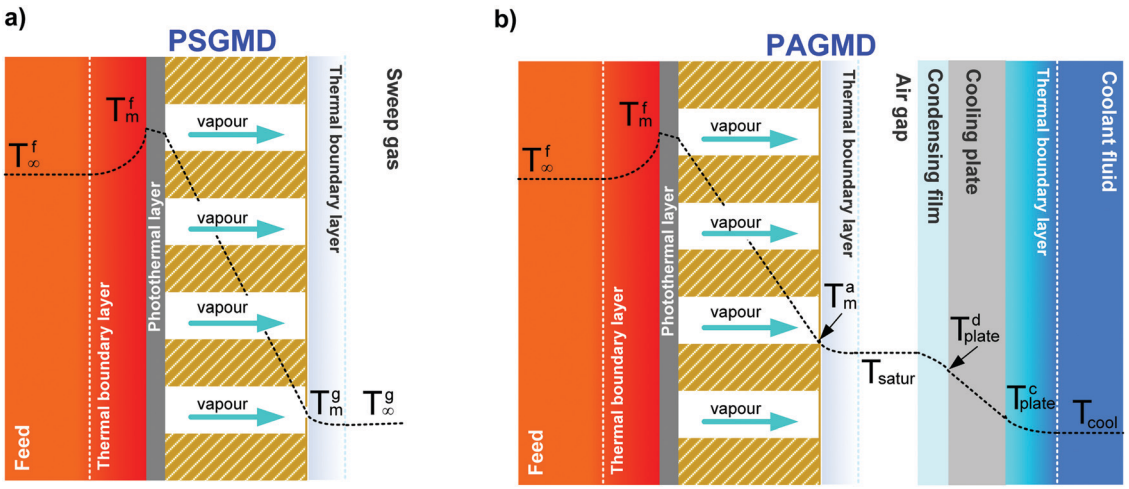

Fig. 16 Temperature profile in: (a) PSGMD and (b) PAGMS configurations.

Table 11 Selected literature studies on PMD

PMD configuration	Membrane	Membrane properties	Feed	PMD operational conditions	Flux (kg m^{-2} h^{-1})	Ref.
PDCMD	FTCS-PDA-PVDF	θ = 125° r = 0.46 μm ε = 73.2%	T_f = 20 °C, NaCl 0.5 M	P_{in} = 0.75 kW m^{-2} T_m^f = 35 °C (wet) Q_f = 16.2 mL min^{-1}	0.5	252
	CB-PVA-PVDF	n.a.	T_f = 20 °C, NaCl 1%	P_{in} = 0.7 kW m^{-2} T_f^m = 21–28 °C (wet) Q_f = 17 mL min^{-1}	0.2–0.5	294
	Fe_3O_4-PVDF-HFP	θ = 140° r = 0.44 μm ε = 91.7%	T_f = 25 °C, NaCl 3.5%	P_{in} = 1 kW m^{-2} T_m^f = 36.5 °C (wet) Q_f = 20 mL min^{-1}	1.0	295
	PDMS-MWCNTs-PVDF	θ = 154° r = 0.51 μm	T_f = 25 °C, NaCl 3.5%	P_{in} = 1 kW m^{-2} T_m^f = 66 °C (wet) Q_f = 1.5 mL min^{-1}	0.6	296
	mXenes-PVDF	θ = 152°	T_f = 65 °C, NaCl 1%	P_{in} = 5.8 kW m^{-2} T_m^f = +49 °C (dry) Q_f = 250 mL min^{-1}	8–10	297
	TiN-PVA-PVDF	LEP = 1.95 bar r = 0.20 μm ε = 70.3%	T_f = 23.1 °C, NaCl 3.5%	P_{in} = 1 kW m^{-2} T_m^f = 39.4 °C (wet) Q_f = 25 mL min^{-1}	1.0	298
	PANI-PVDF	θ = 32° LEP = 2.7 bar	T_f = 25 °C, NaCl 1%	P_{in} = 1 kW m^{-2} T_m^f = 52 °C (dry) Q_f = 0, 01 mL min^{-1}	1.1	299
	PVDF-HFP-PDA	θ = 152° r = 0.26 μm ε = 81%	T_f = 20 °C, NaCl 3.5%	P_{in} = 1 kW m^{-2} T_m^f = 30 °C (wet) Q_f = 20 mL min^{-1}	1.3	300
	$Ca_{10}(PO_4)_6(OH)_2$-PDA-CS	θ = 126° r = 0.2 μm	T_f = 20 °C, 0.5M NaCl	P_{in} = 1 kW m^{-2} T_m^f = 46 °C (dry) Q_f = 3.6 mL min^{-1}	0.9	301
PVMD	ATO-PVDF	θ = 125° LEP = 1, 5 ε = 77%	T_f = 70 °C, NaCl 3.5%,	P_{in} = 0.1 kW m^{-2} T_m^f = 81 °C (wet) Q_f = 1500 mL min^{-1}	27	302
	TiC-TiO_2-PVDF	θ = 162° r = 0.41 μm ε = 67%	T_f = 20 °C, NaCl 30 g L^{-1}	P_{in} = 1 kW m^{-2} T_m^f = 33 °C (wet) v_f = 0.02 m s^{-1}	0.6	303
	Ag-PVDF	θ = 80° r = 0.4 μm ε = 22%	T_f = 30 °C, NaCl 0.5%	P_{in} = 23 kW m^{-2} T_m^f = 54 °C (wet) Q_f = 330 mL min^{-1}	26	278
PSGMD	Ag-PVDF-non-woven tissue	θ = 138° r = 0.15 μm ε = 69%	T_f = 25 °C, NaCl 3%	P_{in} = 23 kW m^{-2} T_m^f = 41 °C (wet) Q_f = 50 mL min^{-1}	8.6	280
PAGMD	TiN-PVA-PVDF	θ = 23° r = 0.79 μm	T_f = 20 °C, NaCl 3.5%	P_{in} = 1 kW m^{-2} T_m^f = 58 °C (wet) Q_f = 0 mL min^{-1}	0.9	304
	FTCS-PDA-Graphene-PTFE	θ = 118° r = 1.58 μm LEP = 1, 2	T_f = 20 °C, NaCl 0.5 M	P_{in} = 0.75 kW m^{-2} T_m^f = 52 °C (dry) Q_f = 0 mL min^{-1}	1.2	305

v_f = flow velocity, n.a. = not available.

As discussed in Section 3.4, carbon-based materials are attracting increasing attention in photothermal membrane manufacturing. The performance of CB deposited on a PVDF membrane *via* the evaporation method was compared with SiO_2/Au anchored to the PVDF surface using polydopamine (PDA) as the binder.[308] CB-PVDF membranes exhibited a flux of 0.5 kg m^{-2} h^{-1} in PDCMD, which is one order of magnitude higher than the value observed in the case of a SiO_2/Au–PVDF membrane (0.07 kg m^{-2} h^{-1}).[308] The theoretical investigation ascribed the flux improvement under one sun irradiation to the remarkable increase (33%) of the TPC.[308]

Electrospinning was also employed to develop a bilayer structure consisting of a commercial PVDF membrane treated with polydopamine to ensure the adhesion of a thin (25 μm) optically absorbing, porous layer of electrospun polyvinyl alcohol (PVA) loaded with carbon black (CB).[294] Although this method allowed increasing the concentration of the photothermal materials up to 20%, the optimal performance in terms of water flux was observed for a value of CB of 5.5 wt% that guaranteed higher light absorption and superior temperature increase at the PVDF membrane surface.[294] Water vapor flux reached 0.22 kg m^{-2} h^{-1} with a solar efficiency of 21% at 20 °C, which increased to 0.55 kg m^{-2} h^{-1} with a solar efficiency of 54% when increasing the operating temperature to 40 °C; a pilot plant equipped with a membrane of 1 m^2 active area and operated in the PDCMD configuration at a peak temperature of ~35 °C was able to distillate 4 L day^{-1} under about 700 W m^{-2} illumination and 8 hours of sunlight in the summer.[294]

Similarly, PVDF membranes were modified to incorporate titanium nitride (TiN)[301] or MXenes ($Ti_3C_2T_x$).[297] MXene fillers were transferred to the membrane surface *via* vacuum filtering; the mechanical stability of the photothermal layer was guaranteed by a protective layer of PDMS subsequently deposited *via* dip-coating.[297] Although the presence of the coating imposed an additional resistance to the mass transport, resulting in a flux decline of *ca.* 13%, the photothermal properties of MXenes allowed a decrease of *ca.* 12% of the energy input per unit volume of the distillate and provided remarkable antifouling properties to the membrane.[297]

Immobilization of Fe_3O_4 NPs on an electrospun polyvinylidene fluoride-*co*-hexafluoropropylene membrane (PVDF-HFP) by vacuum-assisted filtration resulted in a strong interfacial adhesion, owing to the coordination between inorganic NPs and polymeric nanofibers.[295] Fe_3O_4/PVDF-HFP membranes showed a light-to-heat conversion efficiency of 53% and a water evaporation rate of ca 1 kg m^{-2} h^{-1} under static conditions. Fe_3O_4/PVDF-HFP membranes were tested in a pilot scale PDCMD system obtaining a flux of *ca.* 22 kg m^{-2} h^{-1} under the exposure to light irradiation with an intensity of 3 kW m^{-2}, *ca.* 11% higher than the performance observed in absence of irradiation.[295]

The transition towards more eco-compatible approaches inspired the development of novel membranes based on bio-materials, such as hydroxyapatite ($Ca_{10}(PO_4)_6(OH)_2$,), the main inorganic mineral in the bones, or chitosan (CS), a biopolymer. Cao *et al.*[296] developed a bilayer membrane by assembling a photothermal layer of hydroxyapatite NWs coated with PDA over a thermal isolator support of hydroxyapatite NWs. The bio-inspired membrane, operated in the PDCMD configuration, showed a photothermal efficiency of 62% and a water vapor flux of 0.89 kg m^{-2} h^{-1} under 1 sun.[296]

4.3.2 Photothermal vacuum membrane distillation. In PVMD, a vacuum pressure lower than the saturation pressure of the water vapor removed from the feed stream is applied at the distillate side. The most significant advantages of this module configuration include: (i) the highest driving force, leading to the highest transmembrane flux among all PMD configurations operated under the same feed conditions; and (ii) high thermal efficiency due to negligible conductive heat loss, thus making possible the use of homogeneous photothermal membranes. The main drawback is related to the high costs and technical complexity of the vacuum pump and the external condenser. Increased risk of wetting of the hydrophobic membrane subjected to a relatively high-pressure gradient, and consequent decrease of distillate quality, is usually mitigated by the use of membranes with a liquid entry pressure greater than 250 kPa (Sections 2.2 and 5.1).

In a pioneering study on PVMD, Ag NPs were immobilized in PVDF membranes *via* NIPS, thus leading to a homogeneous photothermal membrane.[278] The NIPS method, widely used in the industrial production of membranes, guarantees the stable embodiment of nanofillers into the membrane, avoiding their release as a crucial requirement in water purification operations.[309,310]

Notably, an increase of the temperature at the membrane surface under UV irradiation was revealed, withdrawing the thermal polarization in PVMD experiments and, consequently, dramatically improving the productivity of the process (Fig. 17). Surprisingly, plasmonic nanofillers reversed the temperature polarization effect under UV exposure (TPC increased up to 106.5% for the highest Ag NP loading), thus leading to a membrane surface temperature higher than that in the bulk and determining an unprecedented improvement of the process performance. In fact, the transmembrane water flux increased from 2.2 kg m^{-2} h^{-1} to 25.7 kg m^{-2} h^{-1}, as a consequence of the thermoplasmonic effects induced by UV radiation.[278] Heat balance evidenced an enhancement of the thermal efficiency of the PVMD process by 28%.[311]

Spraying NPs over a substrate is another option to localize the photothermal activity on the membrane surface. This strategy has been already explored for titanium carbide (TiC) using PDMS as an anchoring agent, securing a flux of 0.64 kg m^{-2} h^{-1} under one-sun at room temperature in PVMD.[312] Alternatively, PDMS was also employed as a protective layer to prevent the leakage of MWCNTs sprayed on PVDF nanofibers.[296]

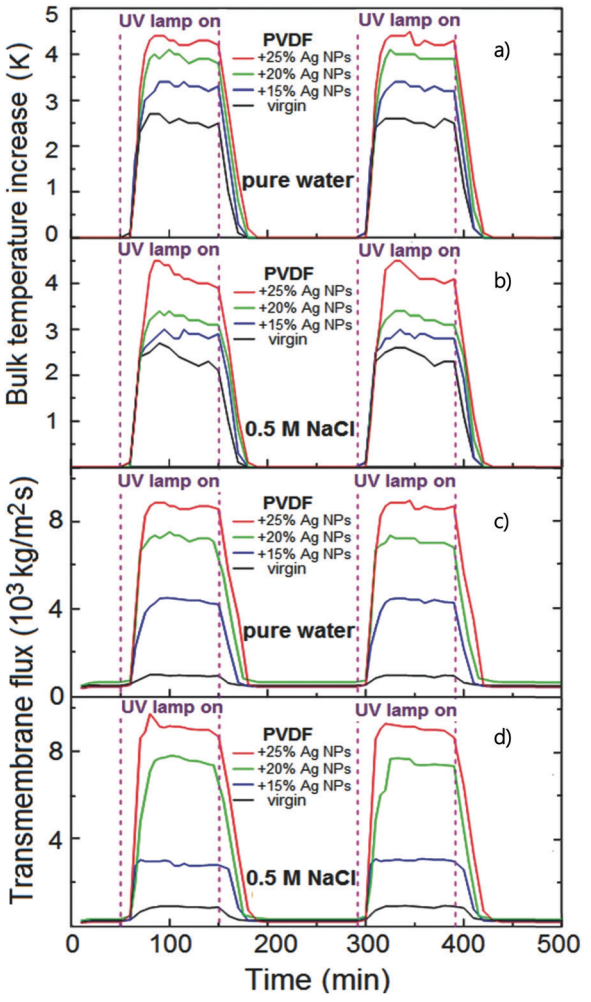

Fig. 17 The effect of Ag NP concentration in PVDF dope solution on (a and b) the bulk feed temperature, and (c and d) water vapor flux in PVMD operated with pure water and 0.5 M NaCl solution. Copyright 2016 Wiley. Used with permission from ref. 278.

Recently, electrospinning has emerged as an innovative and attractive method for nano-composite membranes made of uncountable polymeric nanofibers,[313] enabling the development of a nanostructured photothermal membrane through the effortless dispersion of the photothermal NPs in the polymeric solution submitted to electrospinning. For instance, antimony-doped tin oxide (ATO) nano-powder was directly dispersed in a PDVF solution and subsequently electrospun in order to obtain a PVDF membrane made of functional nanofibers loaded with inorganic ATO NPs.[302] When compared to the unloaded PVDF nanofiber membrane, the hybrid PVDF-ATO membrane exposed to IR light presented a surface temperature higher by *ca.* 13 °C, which reduced the impact of temperature polarization by increasing the TPC from 98.2% to 116.1% in PVMD operation; as a result, a remarkable enhancement of the flux from 8 kg m^{-2} h^{-1} to 27 kg m^{-2} h^{-1} was observed.[302]

4.3.3 Photothermal sweeping gas membrane distillation (PSGMD). In PSGMD, the photothermal membrane is in contact – at the distillate side – with a stream of gas (usually air or, occasionally, inert nitrogen) that sweeps water vapor into a condensation chamber located outside the configuration module. Rather than temperature, system performance is affected by the humidity of the gas stream. With respect to PDCMD, this module configuration offers higher evaporation efficiency due to the modest conductive heat loss across the membrane. It is interesting to consider that PSGMD produces higher permeate flux than PAGMD due to the low mass transfer resistance offered by the sweeping gas. However, high costs associated with the use of an external condenser, aggravated by the difficulty in heat recovery, reduce the attractiveness of this module configuration for water treatment applications. On the other hand, PSBMD is more suitable for dehydration of aqueous solutions as in brine valorization approaches aimed at energy generation (Salinity Gradient Power) or solute crystallization (mineral recovery from brine).

Avci *et al.* developed composite membranes consisting of a 20–25 μm photothermal layer of PVDF loaded with Ag NPs cast on the non-woven fabric of 110–115 μm by VIPS/NIPS routes; the inclusion of the photothermal layer led to a gain of 10-fold transmembrane flux under UV radiation in PSGMD operation.[280] Experiments were performed by feeding a saline solution (0.5 M NaCl) to the membrane module at a flow rate of 3 L h^{-1} at 25 °C whereas air (RH = 50%, T = 20 °C) was flushed at 50 L h^{-1} for the removal of water molecules from the distillate compartment.[280] The warm and hyper-concentrated retentate stream (from 1 to 4 M NaCl) was fed to a reverse electrodialysis (RED) stack to generate a maximum power density of up to 0.9 W m_{MP}^{-2} (MP: RED membrane pair).

4.3.4 Photothermal air gap membrane distillation. In PAGMD, the presence of a stagnant air gap (with thickness typically below 5 mm) between the cold side of the membrane and the condensation surface is adopted with the aim to reduce the conductive heat loss within the membrane. The possibility to realize heat recovery internally to the membrane module, by transferring the latent heat of water vapor – through a cooling plate – to the feed stream (which is, thus, preheated) brought the conventional AGMD configuration to the commercial stage. However, the additional resistance to mass transfer determined by the air and water vapor entrapped within the gap significantly decreases the transmembrane flux.

A dual-layer membrane with a PVA photothermal coating layer doped with TiN electrospun on a PVDF support layer was recently tested in PAGMD.[304] With a stagnant feed-water, the embodiment of 10% of photothermal TIN NPs secured an improvement of the flux from 0.498 kg m^{-2} h^{-1} to 0.772 kg m^{-2} h^{-1} increasing to 0.940 kg m^{-2} h^{-1} when the depth of the feed was decreased from 15 mm to 2 mm.[304] In fact, the feed water on the top of the membrane slightly scatters the radiation reducing the number of effective phonons reaching the membrane surfaces resulting in a diminution of the self-heating performance. As mentioned above, PAGMD offers the advantage to implement the heat recovery strategy, such as in the case of a multi-layer stacked module (1 mm of air gap) equipped with a photothermal FTSC/PDA/graphene/PTFE membrane.[305] A four-layered module achieved a flux of 1.17 kg m^{-2} h^{-1} under the exposure to light irradiation with an intensity of 0.75 kW m^{-2}; which consists of a remarkable gain with respect to the single layer module showing a flux of 0.55 kg m^{-2} h^{-1}.[305]

5. Challenges in PMD

5.1 Reduction of membrane porosity

An optimized design of the photothermal layer requires a proper balance between an effective light harvesting enhanced by a highly dense distribution of NPs at the surface of modified membranes and high porosity for an efficient mass and heat transport through the microporous membrane. This aspect is particularly critical when the incorporation of NPs takes place by applying a functional coating, usually based on polydopamine (PDA),[301,308,314] polypyrrole (PPy),[292,315] polydimethylsiloxane (PDMS),[316] and polyvinyl alcohol (PVA),[294] that inevitably reduces membrane porosity. As discussed in Section 4.2.2, porous structures promote internal light scattering and minimize light reflection and the consequent energy loss.

High membrane porosity also reduces the resistance to the diffusional transport of volatile molecules through the pores, promoting higher transmembrane fluxes. As established by the Dusty Gas Model,[317] both effective free molecular diffusion coefficient $\left(\mathfrak{D}_{ij}^{e}\right)$ and effective Knudsen diffusion $\left(\mathfrak{D}_{K}^{e}\right)$ increase linearly with porosity (ε):

$$\mathfrak{D}_{ij}^{e} = \frac{\varepsilon}{\tau}\mathfrak{D}_{ij} \tag{31a}$$

$$\mathfrak{D}_{K}^{e} = \frac{\varepsilon}{\tau}\frac{d_p}{3}\sqrt{\frac{8RT}{\pi M_i}} \tag{31b}$$

where τ is the tortuosity, d_p is the average pore diameter, R is the universal gas constant, T is the temperature, and M_i is the molecular weight of the diffusing species. Additionally, porosity affects the energetics of PMD, when one considers that a low thermal conductivity (k_m) of the membrane is required to prevent heat loss to the distillate side (eqn (4)). In this regard,

k_m is lowered by increasing the porosity of the hydrophobic membrane, since the thermal conductivity of gases filling the pores (*e.g.*, k_m values for air and water vapour at 25 °C are 0.026 and 0.020 W m^{-1} K^{-1}, respectively) is one order of magnitude lower than the conductivity of inherently hydrophobic polymers typically used to fabricate MD and PMD membranes (*e.g.*, PP: 0.12 W m^{-1} K^{-1}, PVDF: 0.19 W m^{-1} K^{-1}, PTFE: 0.27 W m^{-1} K^{-1}, and PDMS: 0.25 W m^{-1} K^{-1}).[318]

5.2 Fouling and wetting

Fouling is a major challenge in all membrane separation processes, including MD and PMD. The crystallization of sparingly soluble salts – most commonly $CaCO_3$ and $CaSO_4$ in different polymorphs and hydrates – within membrane pores, enhanced by the concentration polarization phenomenon and heterogeneous nucleation mechanism[234,319] ("scaling"), the deposition of colloids and particulate matter such as silica, clay, silt, debris, iron oxide generated from electrochemical corrosion *etc.* ("colloidal and particulate fouling"),[320,321] the accumulation of natural organic matter (NOM) composed of a large spectrum of substances such as proteins, polyhydroxy aromatics, polysaccharides, amino sugars and humic substances[322,323] (organic fouling), and the growth of bacteria and microorganisms excreting extracellular polymer substances (EPS) to adhere to the membrane surface[324,325] ("biological fouling" or "biofouling"), degrade the performance of the membrane process by lowering rejection and transmembrane flux. An additional concern in PMD is that fouling dramatically affects the long-term stability against wetting, with major concerns for the crystallization of hydrophilic salts within the porous membrane matrix, and the presence of organics, synthetic surfactants and natural amphiphiles that reduce the surface tension of the feedwater.[326] As discussed in Section 2.2, the primary parameter for evaluating membrane wettability is the liquid entry pressure (LEP) expressed by the Laplace (Cantor) eqn (2). Therefore, occurrence and prevention of wetting in PMD operation mainly depend on the interactions between feed components (especially those having low surface tension) and membrane (usually characterized by contact angle-based parameters). The correlation between contact angle and interfacial tension of phases in contact, ideally expressed by the Young equation for solid, homogeneous, smooth and flat surfaces,[327] is not applicable to real membranes. In order to take into account the surface roughness, the Wenzel model[231] (suitable at moderate hydrophobicity) and the Cassie–Baxter model[232] (relevant at high roughness and superhydrophobic behavior, *i.e.*, water contact angle $>150°$) were developed (Fig. 18a):

$$\cos\theta_W = r\cdot\cos\theta \quad (32a)$$

$$\cos\theta_C = f_s(\cos\theta + 1) - 1. \quad (32b)$$

In eqn (32), θ is the ideal contact angle (Young model), θ_W is the apparent contact angle (*i.e.*, the one experimentally measured at the macroscopic scale) in the Wenzel model, r is the roughness factor (defined as the ratio of the actual solid/liquid contact area to its vertical projection), θ_C is the apparent contact angle

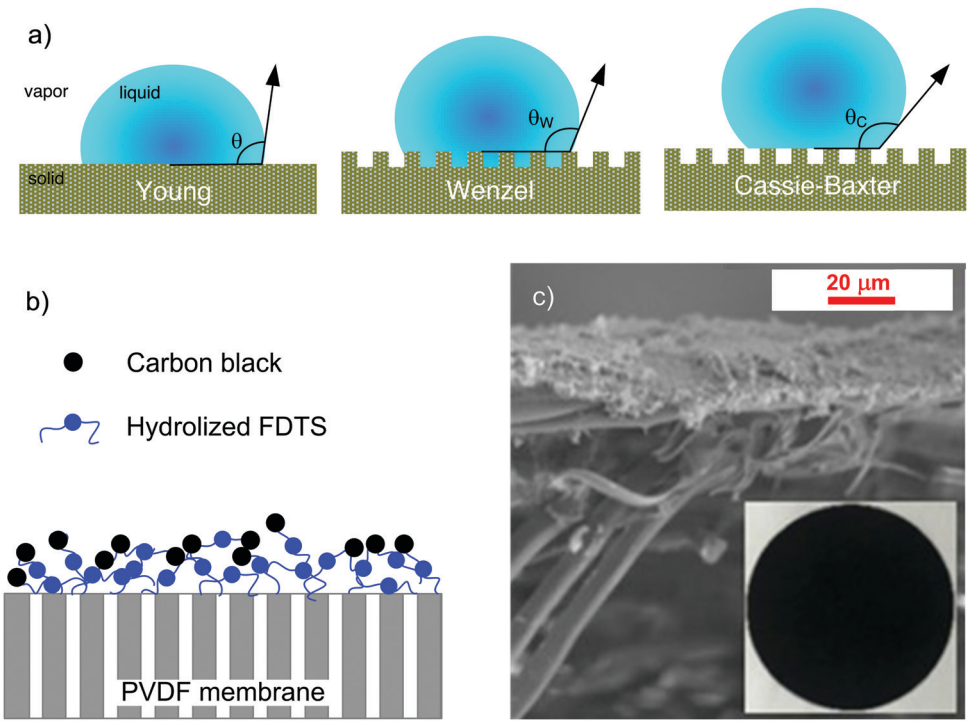

Fig. 18 (a) Schematic representation of the Young, Wenzel and Cassie–Baxter models. (b) Schematics of a dual-layer FDTS-CB membrane structure. Reprinted (adapted) with permission from ref. 355 Copyright 2019 American Chemical Society. (c) SEM images of the cross-section of the FDTS-CB-membrane. Inset: Optical image of the membrane. Reprinted (adapted) with permission from ref. 355 Copyright 2019 American Chemical Society.

in the Cassie model, and f_s is the area fraction of the solid phase.

From a practical point of view, the system is in the Cassie–Baxter state if the liquid, in contact with the re-entrant surface, is supported by the protrusions of the solid substrate and the air trapped in the grooves between these protrusions. In addition to contact angle and LEP, the surface free energy (SFE) of the membrane can provide useful information about the wetting potential of the feed solution with surface tension γ_l. In principle, wetting is predicted to occur if SFE $>$ γ_l; however, the easy applicability of this indicator is counterbalanced by the complexity in SFE calculation, commonly made by the Lifshitz–van der Waals/Acid–base (LW-AB) method.[328] Causes that can lead to membrane wettability are various and, in some cases, concomitant. Table 12 classifies those occurring more frequently in three main categories: feed characteristics,[90,329] fouling,[319,326,330] and operating conditions.[331]

An efficient strategy to avoid or reduce the risk of wetting is to implement an appropriate pre-treatment of the feed solution. Typically, conventional membrane filtration (microfiltration, ultrafiltration) can be operated upstream of PMD to remove particulate and colloidal contaminants, while nanofiltration or softening *via* reactive precipitation can also be used to remove sparingly soluble compounds including divalent and multivalent ions (most commonly Ca^{2+}, Mg^{2+}).[332,333] The use of anti-scalants (*e.g.*, polyacrylic acid) can prolong the induction period for the nucleation of gypsum and calcite, although their organic nature increases the risk of membrane wetting.[334,335] Beside coagulation/flocculation,[336,337] nanofiltration is also effective to remove anionic surfactants[336] and organic matter. However, the addition of a pretreatment stage increases capital and operating costs; for this reason, many research efforts are addressed to the development of wetting-resistant membranes as more versatile and affordable alternatives to sustain long-term stability of MD/PMD operations.

In this respect, preparation methods and/or surface modification protocols are oriented to the fabrication of superhydrophobic membranes (repellent to water), omniphobic membranes (repellent to both water and organic liquids), and Janus membranes composed of an omniphobic or superhydrophobic substrate and a fouling-resistant hydrophilic surface coating, all exhibiting superior wetting resistance.[338]

Membranes are conventionally classified as superhydrophobic when exhibiting a static water contact angle higher than 150° and a contact angle hysteresis (difference between the advancing and receding contact angles) or – alternatively – a sliding angle lower than 10°.[339]

Membrane superhydrophobicity is achieved by tuning surface roughness, thus minimizing the liquid–solid contact area to achieve a Cassie–Baxter state (eqn (32b)). From a practical point of view, surface roughening is usually achieved by attaching nanoparticles (*e.g.*, CNTs,[340,341] graphenes,[342,343] carbon black,[344,345] SiO_2,[346,347] TiO_2,[346,347] ZnO nanostructures[348–350] *etc.*), eventually grafted with perfluorinated agents to increase their hydrophobicity, *via* (electro)spray coating or electrospinning to form hierarchical or re-entrant structures at the nanoscale, or by patterning the skin layer of the membrane with micro-pillared arrays *via* the micromolding phase separation method.[351–353] The complex fabrication procedures involved in the last approach pose severe hurdles to the implementation at large scales. On the other side, the opportunity to simultaneously combine the light-to-heat conversion properties of photothermal nanoparticles with their ability to roughen the membrane surface makes the first option the one preferentially used in PMD. Liao *et al.* (2022) electrosprayed a PVDF/PDMS/MWCNT solution on an electrospun nanofiber PVDF membrane; the consequent formation of microspheres at the PVDF surface conferred the superhydrophobicity to the composite membrane, resulting in water contact angles greater than 150°.[354] Moreover, mixing different typologies of nanoparticles can act synergistically to achieve multiple goals. Anti-wetting and

Table 12 Main causes and related mechanisms of wetting in MD

Category	Cause	Wetting mechanism	Explanation
Feed characteristics	High salt concentration	Surface free energy (SFE) of the membrane $>$ feed surface tension (γ_l)	Decrease of the surface free energy of the membrane
	Presence of organics, oil, and surfactants		Synthetic surfactants and natural amphiphiles decrease the feed surface tension: LEP is reduced proportionally to γ_l Hydrophobic moieties allow organics/oil/surfactants to adsorb on the membrane surface through hydrophobic–hydrophobic interactions, increasing the SFE
Fouling	Scaling-induced wetting	Loss of membrane hydrophobicity	Overcoming the saturation limit of sparingly soluble salts (primarily $CaCO_3$ and $CaSO_4$) leads to the formation of hydrophilic crystals within the membrane pores
	Organic fouling		Strong attractive interactions between membrane and humic acids/polysaccharides/proteins *etc.*, decrease the surface free energy of the membrane
	Biological fouling (or Biofouling)	Biological microorganisms (*e.g.* bacteria, fungi, algae *etc.*) grow at the membrane surface forming a gel-like structure termed "biofilm"	Pore wetting occurs due to the secretion of extracellular polymeric substances (EPS) with amphiphilic properties
Operating conditions	High feed flow rate	Transmembrane pressure $\Delta P >$ LEP	High feed velocity increases the pressure of the feed solution; wetting risk is enhanced when a vacuum is applied at the distillate side (VMD/PVMD)
	Chemical degradation during the long-term MD process	Loss of membrane hydrophobicity	Reduction of contact angle due do the formation of hydrophilic groups (*e.g.* hydroxyl (OH), carbonyl (C═O) and unsaturated (C═C) groups) by chemical oxidative degradation

anti-fouling abilities have been stimulated by spraying on PVDF membranes a mixture of titanium carbide (TiC) NPs – exhibiting photothermal properties – and titania (TiO_2) NPs – having potential to degrade organic compounds; a final fluorination step was accomplished to enhance surface hydrophobicity (water contact angle of 154.7°).[303]

Whereas most of the superhydrophobic membranes are prone to wetting by organic solutions, omniphobic surfaces exhibit high repellency to both water and other low surface tension liquids such as surfactants, alcohols and oils. Typically, the preparation of omniphobic surfaces includes the creation of a single/multilevel re-entrant hierarchical texture that provides an energy barrier to the wetting transition from the metastable Cassie–Baxter state to the stable Wenzel state, and the functionalization (typically a fluorination treatment) of the coated substrates to lower the SFE.

A re-entrant topography is typically obtained by adding nanoparticles such as SiO_2,[356,357] ZnO,[358,359] TiO_2[358,359] *etc.*, while chemical modification is prevalently carried out *via* fluorinated alkyl silane (FAS), 1*H*,1*H*,2*H*,2*H*-perfluorodecyltriethoxysilane (17-FAS), 1*H*,1*H*,2*H*,2*H*-perfluorodecyltriethoxysilane (FTCS), 1*H*,1*H*,2*H*,2*H*-perfluorodecyltriethoxysilane (FDTES), perfluorodecyltrichlorosilane (FDTS), fluorinated-decyl polyhedraloligomeric silsesquioxane (F-POSS), trichloro (1*H*,1*H*,2*H*,2*H*-tridecafluoro-*n*-octyl) silane (FOTS), 1*H*,1*H*,2*H*,2*H*-perfluorooctyltrichlorosilane (PFTS), perfluorooctanoate (PFO), 1*H*,1*H*,2*H*,2*H*-perfluorooctyltrichlorosilane (PFOTS), and poly(perfluorodecyl acrylate) (PPFDA), as comprehensively reviewed.[90] Focusing on specific PMD applications, omniphobic photothermal membranes were prepared by forming a hierarchical structure of 17-FAS modified carbon black (CB) NPs on the PVDF membrane surface. The functionalization resulted in an increase of the contact angle from 0° (pristine PVDF membrane) to 94.2° (0.2 wt% CB NPs) for an 80% v/v ethanol–water mixture (surface tension of 26 mN m^{-1}), and from 132.1° to 140.8° for pure water (surface tension of 72 mN m^{-1}). In addition, the membrane exhibited anti-wetting behavior in the presence of surfactants: no liquid penetration was observed for sodium dodecyl sulfate (SDS) concentration within the investigated range of 0.1–0.4 mM, while liquid intrusion through a pristine PVDF membrane was detected at 0.2 mM SDS.[360] With a similar approach, FDTS-CB coated PVDF membranes (Fig. 18b and c) exhibited an increased water CA from 118.1° (pristine PVDF) to 142.3°, corresponding to an LEP of 424 kPa; moreover, FDTS-CB coated PVDF membranes showed effective repellent behavior the low-surface tension liquids, such as mineral oil (138.5°) and ethanol (126.2°) in air.[355]

In the perspective of PMD, the manufacturing of the hydrophilic face of Janus composite membranes resistant to fouling and wetting can potentially exploit the photothermal ability of polymers such as polypyrrole[361] and polydopamine.[300]

5.3 Cost assessment of photothermal MD

The purpose of the implementation of photothermal membrane technology is to produce freshwater at the water–energy nexus by minimizing the environmental impact of the desalination and water treatment processes. Despite their superior performance in the light-to-heat conversion, there are serious concerns about the viability of photothermal membranes based on metallic NPs. Their synthesis commonly implies the employment of harmful chemicals (*e.g.* CTAB and $NaBH_4$) employed as capping/reducing agents, hindering the industrial scale up of the production of metallic nanoparticles.[172] Microbes have gained more attention as promising, inexpensive, energy-efficient and green nano-factories, whereas plant extracts (*e.g.*, polyphenols, phenolic acid, alkaloids, proteins, and sugar) have been extensively studied in metal NP fabrication as a reducing or stabilizing agent of nanoparticles allowing an inexpensive scalable eco-friendly route to be followed.[362] Nevertheless, the understanding of the molecular mechanism of biosynthesis is not still achieved. Moreover, the high cost of photothermal membranes loaded with noble metal NPs (typically above 100 \$\$ g^{-1}[363]) is the main drawback of the commercialization of thermoplasmonics.

From an energetic point of view, thermoplasmonics typically relies on UV radiation, characterized by a consequent remarkable specific energy consumption for the generation of artificial radiation,[364] counterbalanced by outstanding performance. Taking as example the work of Politano *et al.* (2017),[278] PVDF membranes loaded with Ag NPs guaranteed a flux of *ca.* 26 kg m^{-2} h^{-1} under UV radiation of 23 kW m^{-2} resulting in a specific energy consumption of 1.5 kW h L^{-1} which makes photothermal PMD based on noble metal NPs technically misleading.

Thus, the band-gap engineering for the exploitation of sunlight is a crucial strategy to overcome the severe energy impact of thermoplasmonics.[364] In this framework, advanced carbon-based materials (*e.g.* graphene and CWNTs) emerged as the most viable solution acting as a black body achieving a photothermal efficiency above 95% under natural radiation. Unfortunately, the cost of graphene (150–250 \$ g^{-1}[365]) still makes the preparation of the next-generation of photothermal carbon-based materials prohibitively expensive.

On the other hand, commercially available and inexpensive carbonous NPs have the potential to guarantee economic and energetic viability to photothermal MD. Roughly, the natural radiation daily provides 4–8 kW h m^{-2} useful to vaporize 3–6 L m^{-2} day^{-1} (water evaporation heat is around 667 kW h m^{-3}) assuming a photothermal efficiency of 50%,[366] as confirmed by the stand-alone PMD system based on CB-PVA-PVDF developed by Dongare *et al.* (2017).[294] Another interesting advantage is the opportunity to synthesize effective photothermal carbon-based NPs by the carbonization of organic compounds opening the door for the valorization of the biomass coherently with the circular economy paradigm.[367]

Beyond these two major categories, PDA has gained more attention as an ecofriendly and inexpensive photothermal material being a biocompatible and biodegradable polymer with a broad absorption of the solar radiation.[368] Although PDA showed competitive performance with conventional carbon-based materials,[252,307] the cost of a mussel-inspired membrane (33\$ m^{-2}[369]) and its long term stability under real conditions are two critical challenges to be addressed.[370]

6. Other applications based on photothermal membrane distillation

In recent years, membrane crystallization (MCr) has demonstrated the potential to replace the conventional crystallizers, considering its unique advantages. MCr enables accurate control of the transmembrane flux of the solvent driving the system through specific supersaturation pathways within the metastable zone, thus enhancing crystal formation in terms of particle shape and size distribution, polymorph/hydration form selection and impurity control. Moreover, the physicochemical properties of the polymeric membrane (surface energy/contact angle) and topography (roughness, porosity, pore size, *etc.*) act as exclusive tools to modulate the extent of the free Gibbs energy barrier to heterogeneous nucleation and, ultimately, to control the crystallization kinetics.[371] Thermally- or osmotically-driven MCr can be considered as an evolution of the MD process since supersaturation is achieved through the removal of the solvent from the feed solutions.[372] Among the most interesting applications, MCr has been studied as a feasible method for the post-treatment of the hypersaline retentate of desalination and wastewater treatment processes for the recovery of valuable minerals such as NaCl,[30] Na_2SO_4,[373] $MgSO_4{\cdot}7H_2O$,[373] LiCl[374] *etc.*

A nature-inspired synthetic floating leaf made of a graphene oxide (GO) thin film has been studied for solar-driven MCr. Under 0.82 sun illumination, the system reported allowed the photothermal generation of steam at a rate of 1.1 L m^{-2} h^{-1} with a light-to-vapor energy conversion of 54%.[375] A long-term evaporation experiment with a 15 wt% NaCl solution showed the possibility to crystallize the salt on the membrane surface.[375]

Inspired by the natural transpiration process in plants, GO-based membranes with over 85% solar steam efficiency under one-sun were employed for the treatment of heavy-metal-contaminated solutions (Cu^{2+}, Cr^{3+}, and Pb^{2+}).[376] Nevertheless, this strategy can potentially open the perspective of a sustainable recovery of valuable raw materials: a photothermal 3-D device based on a GO-filter paper membrane allowed the treatment of an aqueous solution mimicking the wastewater from electroplating industry and the simultaneous precipitation of copper sulfate salt ($CuSO_4$ $5H_2O$).[259]

Overall, from the perspective of ZLD, photothermal membranes can potentially guarantee a thermally efficient steam generation and a feasible recovery of valuable salt crystals to fulfil the goal of a sustainable brine management.[42]

The implementation of photothermal membranes for a simultaneous production of freshwater and energy with the goal to alleviate the water–energy nexus was investigated by using a photocatalytic hydrogel of TiO_2/Ag nanofibers embedded into CS.[377] Ag played the dual role of: (i) thermoplasmonic effects facilitating the vaporization of water at a rate of 1.49 kg m^{-2} h^{-1} under 1 sun and (ii) a cocatalyst to facilitate charge transfer and the light absorption for improved hole-scavenging activity for the photocatalytic H_2 generation at a rate of 3260 μmol m^{-2} h^{-1} [377]. An emerging trend is to exploit the electrochemical potential of the brines to produce renewable blue energy (Salinity Gradient Power) *via* Reverse Electrodialysis (RED), an electromembrane-based process that harvests the Gibbs free energy of mixing of solutions with different salinity;[378] feeding the hypersaline retentate from the photothermal SGMD unit to a RED stack enabled the recovery of 10% of the energy not used for water evaporation, thus improving the overall efficiency of the integrated system.[280]

Biofouling control is essential to extend the shelf-life of the membrane, to reduce the operation and maintenance cost, to sustain the long-term performance of the membrane process, and to ensure a stable quality of produced water. Carbon-based materials and metal NPs have been widely explored to enhance the anti-fouling properties of the membranes.[379] Ag and Au NPs are able to inhibit biofouling because of their reactivity with the thiol groups present in bacteria, leading to the inactivation of the proteins.[380] The synergistic coupling of the photothermal and bactericidal properties of GO and Au NPs allowed the development of multifunctional membranes: the presence of a nanoheater effectively inactivated the bacteria on the membrane surface improving its fouling resistance.[381] Studies have demonstrated that rGO flakes dispersed in a cellulose-based membrane efficiently converted the light energy to heat, killing *Escherichia coli* bacteria within 3 min.[382]

MD has been also proven as a beneficial treatment for wastewater from textile industries ensuring the recovery of large portions of water and the concentration of dyes according to the ZLD paradigm.[383,384] In this scenario, the integration of PMD with photocatalytic membranes (synergic exploitation of light and a photocatalytic semiconductor for the generation of oxidizing/reducing species inducing the total degradation of organic and inorganic pollutants to innocuous substances) demonstrated a great potential for use in energy-efficient and intensified wastewater treatment processes.[385] Graphene-based membranes have been widely studied because of their excellent photocatalytic properties explored in many important energy and environmental applications including photocatalytic pollutant degradation, H_2 production, and CO_2 reduction.[386] However, the role of carbon-based nanomaterials has been so far underestimated if one considers that their photothermal behaviour can play an important role in the enhancement of photocatalytic performance.[387] For instance, the photothermal effect of rGO has been exploited in cooperation with the TiO_2 P25 catalyst to develop a nanocomposite with superior efficiency for the photocatalytic degradation of methylene blue.[387] Likewise, photothermal-assisted 3D flower-like CuS superparticles exhibited a 213% enhanced catalytic activity for the photodegradation of methylene blue in water.[388]

The use of PMD could also alleviate the pressure on water-stressed oil-producing countries, enabling the remediation of their wastewater with an organic carbon rejection ranging between 73% and 96%.[389] Nevertheless, the implementation of photothermal materials is of interest for breaking azeotropic mixtures: Ag NPs in the PDMS membrane significantly improved the performance in terms of flux and selectivity in ethanol recovery from aqueous solution upon light exposure.[390]

Overall, advancements in photothermal membranes have injected new vitality into the field of membranes for water

treatment applications, giving the realistic perspective to achieve the blue dream of low-energy water purification.[42]

7. Conclusions and outlook

MD is an emerging technology potentially able to mitigate water–energy nexus pressure, producing freshwater from different sources such as seawater, brackish water, brine and contaminated water. Unlike RO, the aptitude of MD to efficiently treat water with higher salt concentration may positively affect the sustainability of the desalination industry. However, the operativity of MD at the industrial scale has been so far hampered due to serious limitations related to low productivity in terms of transmembrane flux and low thermal efficiency mainly due to temperature polarization.

Recently, the synergic combination of solar energy and MD has improved the sustainability of the process. The emergence of engineered photothermal materials with a wide range of physicochemical properties (*i.e.*, morphology, structure, and absorption) and light-to-heat conversion higher than 90% is opening new avenues for MD. Recent advancements in the synthesis and functionalization of photothermal NPs and, in those of metal and carbon-based NPs, encourage the progress towards the production scale-up and high-volume applications. Furthermore, as concerns photothermal materials, the advent of high-throughput computational screening over thousands of candidate materials could favor the optimization of solar thermal conversion though detailed comparative evaluation of their physicochemical and electronic properties (dielectric functions, optical anisotropies, plasmonic excitations matching solar radiation, *etc.*), with subsequent benefits for solar-driven MD.

The dispersion of the photothermal material into/onto the membrane demonstrated the superior performance of the interfacial solar evaporation by the *in situ* harvesting of the nano-heating spots at the membrane–feed water interface, leading to mitigation or withdrawal of temperature polarization. Although in an embryonic phase, the recent advent of PMD is recognized as a promising arrow in the quiver when facing the challenge of sustainable water desalination and purification processes using renewable energies, such as sunlight. However, even if the efficiency of sun-powered PMD at lab-scale is proven, long-term stability of materials is still questionable. The mitigation of fouling (less aggressive in MD/PMD with respect to conventional pressure-driven membrane operations) is typically achieved by applying a hydrophilic coating on top of a hydrophobic membrane to improve the organic fouling resistance; this approach also limits the potential leakage of NPs, assuring longevity to the membranes.

In this scenario, the fundamental understanding of the effect of the membrane structure and the operating conditions of the process on the energy management is crucial for the scalability of PMD.

It is worth mentioning that modularity is another strength point, which paves the way for the practical and flexible integration of PMD within downstream process schemes for the post-treatment and the valorisation of waste effluents, including desalination of brine. These prospects are exciting with a view to circular economy and green transition, although the economic potential and the environmental footprint of PMD require further assessment.

Conflicts of interest

There are no conflicts to declare.

Acknowledgements

Sergio Santoro acknowledges the European Commission for the financial support activated under the PON ''Research and Innovation'' 2014–2020, Action I.2 ''Researchers' Mobility'', Notice D. D. 407 of 02.27.2018 – AIM ''Attraction and International Mobility''-Line 2 ''Researchers' Attraction''.

References

1 T. Distefano and S. Kelly, *Ecol. Econ.*, 2017, **142**, 130–147.
2 C. Tortajada and A. K. Biswas, *Curr. Opin. Environ. Sustain.*, 2018, **34**, 21–25.
3 J. R. Ziolkowska, *Water Supply*, 2015, **16**, 563–578.
4 J. Willet, K. Wetser, J. Vreeburg and H. H. M. Rijnaarts, *Water Resour. Ind.*, 2019, **21**, 100110.
5 E. Drioli, S. Santoro, S. Simone, G. Barbieri, A. Brunetti, F. Macedonio and A. Figoli, *React. Funct. Polym.*, 2014, **79**, 1–7.
6 B. G. Ridoutt and S. Pfister, *Glob. Environ. Chang.*, 2010, **20**, 113–120.
7 S. Santoro, H. Estay, A. H. Avci, L. Pugliese, R. Ruby-Figueroa, A. Garcia, M. Aquino, S. Nasirov, S. Straface and E. Curcio, *Clean. Eng. Technol.*, 2021, **2**, 100091.
8 A. Alkaisi, R. Mossad and A. Sharifian-Barforoush, *Energy Procedia*, 2017, **110**, 268–274.
9 A. Ali, R. A. Tufa, F. Macedonio, E. Curcio and E. Drioli, *Renewable Sustainable Energy Rev.*, 2018, **81**, 1–21.
10 D. L. Shaffer, L. H. Arias Chavez, M. Ben-Sasson, S. Romero-Vargas Castrillón, N. Y. Yip and M. Elimelech, *Environ. Sci. Technol.*, 2013, **47**, 9569–9583.
11 A. Gherghel, C. Teodosiu and S. De Gisi, *J. Clean. Prod.*, 2019, **228**, 244–263.
12 N. Misdan, W. J. Lau and A. F. Ismail, *Desalination*, 2012, **287**, 228–237.
13 F. Calise, F. L. Cappiello, R. Vanoli and M. Vicidomini, *Appl. Energy*, 2019, **253**, 113575.
14 M. Badruzzaman, N. Voutchkov, L. Weinrich and J. G. Jacangelo, *Desalination*, 2019, **449**, 78–91.
15 I. C. Karagiannis and P. G. Soldatos, *Desalination*, 2008, **223**, 448–456.
16 N. Voutchkov, *Desalination*, 2018, **431**, 2–14.
17 Desalination and Water Reuse by the Numbers, **https://idadesal.org/**.
18 A. Deshmukh, C. Boo, V. Karanikola, S. Lin, A. P. Straub, T. Tong, D. M. Warsinger and M. Elimelech, *Energy Environ. Sci.*, 2018, **11**, 1177–1196.

19 ResearchAndMarkets.com, Major Reverse Osmosis System Components for Water Treatment: The Global Market, 2020.
20 K. P. Lee, T. C. Arnot and D. Mattia, *J. Membr. Sci.*, 2011, **370**, 1–22.
21 A. H. Avci, D. A. Messana, S. Santoro, R. A. Tufa, E. Curcio, G. Di Profio and E. Fontananova, *Membranes*, 2020, **10**, 168.
22 S. Santoro, R. A. Tufa, A. H. Avci, E. Fontananova, G. Di Profio and E. Curcio, *Energy*, 2021, 120563.
23 C. Fritzmann, J. Löwenberg, T. Wintgens and T. Melin, *Desalination*, 2007, **216**, 1–76.
24 C. Laspidou, K. Hadjibiros and S. Gialis, *Water*, 2010, **2**, 75–84.
25 I. Abd-Elaty, A. E. L. Shahawy, S. Santoro, E. Curcio and S. Straface, *Sci. Total Environ*, 2021, **795**, 148928.
26 S. Al-Obaidani, E. Curcio, F. Macedonio, G. Di Profio, H. Al-Hinai and E. Drioli, *J. Membr. Sci.*, 2008, **323**, 85–98.
27 M. A. E. R. Abu-Zeid, Y. Zhang, H. Dong, L. Zhang, H. L. Chen and L. Hou, *Desalination*, 2015, **356**, 1–14.
28 A. Cerda, M. Quilaqueo, L. Barros, G. Seriche, M. Gim-Krumm, S. Santoro, A. H. Avci, J. Romero, E. Curcio and H. Estay, *J. Water Process Eng.*, 2021, **41**, 102063.
29 E. Drioli, A. Ali and F. Macedonio, *Desalination*, 2015, **356**, 56–84.
30 X. Ji, E. Curcio, S. Al Obaidani, G. Di Profio, E. Fontananova and E. Drioli, *Sep. Purif. Technol.*, 2010, **71**, 76–82.
31 I. Hitsov, T. Maere, K. De Sitter, C. Dotremont and I. Nopens, *Sep. Purif. Technol.*, 2015, **142**, 48–64.
32 S. Santoro, I. M. Vidorreta, V. Sebastian, A. Moro, I. M. Coelhoso, C. A. M. Portugal, J. C. Lima, G. Desiderio, G. Lombardo, E. Drioli, R. Mallada, J. G. Crespo, A. Criscuoli and A. Figoli, *J. Membr. Sci.*, 2017, **536**, 156–166.
33 S. Santoro, I. Vidorreta, I. Coelhoso, J. C. Lima, G. Desiderio, G. Lombardo, E. Drioli, R. Mallada, J. Crespo, A. Criscuoli and A. Figoli, *Molecules*, 2019, **24**, 638.
34 J. Koschikowski, M. Wieghaus and M. Rommel, *Water Sci. Technol. Water Supply*, 2003, **156**, 295–304.
35 X. Wang, L. Zhang, H. Yang and H. Chen, *Desalination*, 2009, **247**, 403–411.
36 R. B. Saffarini, E. K. Summers, H. A. Arafat and J. H. Lienhard V, *Desalination*, 2012, **286**, 332–341.
37 M. A. A. Hejazi, O. A. Bamaga, M. H. Al-Beirutty, L. Gzara and H. Abulkhair, *Sep. Purif. Technol.*, 2019, **220**, 300–308.
38 A. E. Kabeel, M. Abdelgaied and E. M. S. El-Said, *Renew. Energy*, 2017, **106**, 192–200.
39 F. Banat, N. Jwaied, M. Rommel, J. Koschikowski and M. Wieghaus, *Desalination*, 2007, **217**, 17–28.
40 F. Banat, R. Jumah and M. Garaibeh, *Renew. Energy*, 2002, **25**, 293–305.
41 L. Zhu, M. Gao, C. K. N. Peh and G. W. Ho, *Mater. Horiz.*, 2018, **5**, 323–343.
42 C. Zhang, H.-Q. Liang, Z.-K. Xu and Z. Wang, *Adv. Sci.*, 2019, **6**, 1900883.
43 P. Zhang, Q. Liao, H. Yao, Y. Huang, H. Cheng and L. Qu, *Energy Storage Mater.*, 2019, **18**, 429–446.
44 L. Shi, X. Wang, Y. Hu, Y. He and Y. Yan, *Appl. Therm. Eng.*, 2020, **179**, 115691.
45 Q. Huang, X. Liang, C. Yan and Y. Liu, *Appl. Energy*, 2021, **283**, 116361.
46 Y. Lin, H. Xu, X. Shan, Y. Di, A. Zhao, Y. Hu and Z. Gan, *J. Mater. Chem. A*, 2019, **7**, 19203–19227.
47 H. Ghasemi, G. Ni, A. M. Marconnet, J. Loomis, S. Yerci, N. Miljkovic and G. Chen, *Nat. Commun.*, 2014, **5**, 4449.
48 A. Politano, in *Current Trends and Future Developments on (Bio-) Membranes*, ed. A. Basile, E. Curcio and Inamuddin, Elsevier, 2019, pp. 55–80.
49 N. S. Fuzil, N. H. Othman, N. H. Alias, F. Marpani, M. H. D. Othman, A. F. Ismail, W. J. Lau, K. Li, T. D. Kusworo, I. Ichinose and M. M. A. Shirazi, *Desalination*, 2021, **517**, 115259.
50 S. Santoro, A. H. Avci, M. Aquino, L. Pugliese, S. Straface and E. Curcio, *Towards the Global Rise of Zero Liquid Discharge for Wastewater Management: The Mining Industry Case in Chile, The Handbook of Environmental Chemistry*, Springer Berlin Heidelberg, Berlin, Heidelberg, 2021, pp. 1–14, DOI: 10.1007/6982021785.
51 A. G. Razaqpur, Y. Wang, X. Liao, Y. Liao and R. Wang, *Water Res.*, 2021, **201**, 117299.
52 S. W. Sharshir, A. M. Algazzar, K. A. Elmaadawy, A. W. Kandeal, M. R. Elkadeem, T. Arunkumar, J. Zang and N. Yang, *Desalination*, 2020, **491**, 114564.
53 E. Curcio, G. Di Profio, E. Fontananova and E. Drioli, in *Advances in Membrane Technologies for Water Treatment: Materials, Processes and Applications*, ed. A. Basile, A. Cassano and N. K. Rastogi, Woodhead Publishing, Cambridge, 2015, pp. 411–441.
54 E. Curcio, G. Di Profio and E. Drioli, in *Comprehensive Membrane Science and Engineering*, ed. E. F. Drioli, Enrico and L. Giorno, Elsevier, Amsterdam, 2010.
55 N. Thomas, M. O. Mavukkandy, S. Loutatidou and H. A. Arafat, *Sep. Purif. Technol.*, 2017, **189**, 108–127.
56 E. Curcio and G. Di Profio, *The Handbook of Continuous Crystallization*, The Royal Society of Chemistry, 2020, pp. 321–352.
57 M. Gryta, *J. Membr. Sci.*, 2005, **246**, 145–156.
58 S. M. Huang, Y. H. Chen, W. Z. Yuan, S. Zhao, Y. Hong, W. B. Ye and M. Yang, *Sep. Purif. Technol.*, 2019, **220**, 334–344.
59 A. M. Alklaibi and N. Lior, *J. Membr. Sci.*, 2006, **282**, 362–369.
60 P. Wang and T. S. Chung, *J. Membr. Sci.*, 2015, **474**, 39–56.
61 G. Zuo, R. Wang, R. Field and A. G. Fane, *Desalination*, 2011, **283**, 237–244.
62 G. Lewandowicz, W. Białas, B. Marczewski and D. Szymanowska, *J. Membr. Sci.*, 2011, **375**, 212–219.
63 Z. Xie, T. Duong, M. Hoang, C. Nguyen and B. Bolto, *Water Res.*, 2009, **43**, 1693–1699.
64 A. Criscuoli, P. Bafaro and E. Drioli, *Desalination*, 2013, **323**, 17–21.
65 J. A. Andrés-Mañas, A. Ruiz-Aguirre, F. G. Acién and G. Zaragoza, *Desalination*, 2020, **475**, 114202.

66 S. O. Olatunji and L. M. Camacho, *Front. Energy Res.*, 2018, **6**, 130.
67 A. Mourgues, N. Hengl, M. P. Belleville, D. Paolucci-Jeanjean and J. Sanchez, *J. Membr. Sci.*, 2010, **355**, 112–125.
68 S. Shukla, J. P. Méricq, M. P. Belleville, N. Hengl, N. E. Benes, I. Vankelecom and J. Sanchez Marcano, *J. Membr. Sci.*, 2018, **545**, 150–157.
69 S. Shukla, N. E. Benes, I. Vankelecom, J. P. Méricq, M. P. Belleville, N. Hengl and J. S. Marcano, *J. Membr. Sci.*, 2015, **493**, 167–178.
70 S. K. Hubadillah, Z. S. Tai, M. H. D. Othman, Z. Harun, M. R. Jamalludin, M. A. Rahman, J. Jaafar and A. F. Ismail, *Sep. Purif. Technol.*, 2019, **217**, 71–84.
71 Z. Cui, E. Drioli and Y. M. Lee, *Prog. Polym. Sci.*, 2014, **39**, 164–198.
72 S. A. Ali and M. A. J. Mazumder, *J. Hazard. Mater.*, 2018, **350**, 169–179.
73 L.-T. Huang, P.-S. Hsu, C.-Y. Kuo, S.-C. Chen and J.-Y. Lai, *Desalination*, 2008, **233**, 64–72.
74 S. Feng, Z. Zhong, Y. Wang, W. Xing and E. Drioli, *J. Membr. Sci.*, 2018, **549**, 332–349.
75 L. Eykens, K. De Sitter, C. Dotremont, L. Pinoy and B. Van der Bruggen, *Sep. Purif. Technol.*, 2017, **182**, 36–51.
76 A. Figoli, S. Santoro, F. Galiano and A. Basile, *Pervaporation membranes: Preparation, characterization, and application*, 2015.
77 C. M. Hansen, *Hansen solubility parameters: a user's handbook*, CRC Press, Boca Raton, 2007.
78 M. H. V. Mulder, T. Franken and C. A. Smolders, *J. Membr. Sci.*, 1985, **22**, 155–173.
79 N. T. Hassankiadeh, Z. Cui, J. H. Kim, D. W. Shin, S. Y. Lee, A. Sanguineti, V. Arcella, Y. M. Lee and E. Drioli, *J. Membr. Sci.*, 2015, **479**, 204–212.
80 F. Russo, C. Ursino, E. Avruscio, G. Desiderio, A. Perrone, S. Santoro, F. Galiano and A. Figoli, *Membranes*, 2020, **10**, 36.
81 J. Chang, J. Zuo, L. Zhang, G. S. O'Brien and T.-S. Chung, *J. Membr. Sci.*, 2017, **539**, 295–304.
82 T. Marino, F. Russo and A. Figoli, *Membranes*, 2018, **8**, 71.
83 S. Ebnesajjad, in *Fluoroplastics (Second Edition)*, ed. S. Ebnesajjad, William Andrew Publishing, Oxford, 2015, vol. 1, pp. 382–395.
84 F. Russo, C. Ursino, B. Sayinli, I. Koyuncu, F. Galiano and A. Figoli, *Clean Technol.*, 2021, **3**, 761–786.
85 M. Khayet, *Adv. Colloid Interface Sci.*, 2011, **164**, 56–88.
86 F. Sadeghi, A. Ajji and P. J. Carreau, *J. Membr. Sci.*, 2007, **292**, 62–71.
87 G.-G. Wu, C. Ding, W.-B. Chen, Y. Zhang, W. Yang and M.-B. Yang, *Polymer*, 2019, **175**, 177–185.
88 N. G. P. Chew, S. Zhao, C. H. Loh, N. Permogorov and R. Wang, *J. Membr. Sci.*, 2017, **528**, 126–134.
89 R. B. Saffarini, B. Mansoor, R. Thomas and H. A. Arafat, *J. Membr. Sci.*, 2013, **429**, 282–294.
90 H. Chang, B. Liu, Z. Zhang, R. Pawar, Z. Yan, J. C. Crittenden and R. D. Vidic, *Environ. Sci. Technol.*, 2021, **55**, 1395–1418.
91 L. Eykens, K. De Sitter, C. Dotremont, L. Pinoy and B. Van der Bruggen, *Ind. Eng. Chem. Res.*, 2016, **55**, 9333–9343.
92 P. A. B. de Sampaio, *Desalination*, 2022, **533**, 115769.
93 L. Li and K. K. Sirkar, *J. Membr. Sci.*, 2016, **513**, 280–293.
94 P. Wang and T.-S. Chung, *J. Membr. Sci.*, 2015, **474**, 39–56.
95 S. Santoro, E. Drioli and A. Figoli, *Coatings*, 2016, **6**, 40.
96 K. Xu, Y. Cai, N. T. Hassankiadeh, Y. Cheng, X. Li, X. Wang, Z. Wang, E. Drioli and Z. Cui, *Desalination*, 2019, **456**, 13–22.
97 D. Tong, X. Wang, M. Ali, C. Q. Lan, Y. Wang, E. Drioli, Z. Wang and Z. Cui, *Sep. Purif. Technol.*, 2016, **157**, 1–8.
98 M. H. D. A. Farahani and V. Vatanpour, *Sep. Purif. Technol.*, 2018, **197**, 372–381.
99 Y. Wu, Y. Xia, X. Jing, P. Cai, A. D. Igalavithana, C. Tang, D. C. W. Tsang and Y. S. Ok, *J. Hazard. Mater.*, 2020, **382**, 120976.
100 S. Santoro, A. J. Moro, C. A. M. Portugal, J. G. Crespo, I. M. Coelhoso and J. C. Lima, *J. Membr. Sci.*, 2016, **514**, 467–475.
101 S. Santoro, V. Sebastian, A. J. Moro, C. A. M. Portugal, J. C. Lima, I. M. Coelhoso, J. G. Crespo and R. Mallada, *J. Colloid Interface Sci.*, 2017, **486**, 144–152.
102 O. Iglesias, M. J. Rivero, A. M. Urtiaga and I. Ortiz, *Chem. Eng. J.*, 2016, **305**, 136–148.
103 J. Guo, D. Y. S. Yan, F. L.-Y. Lam, B. J. Deka, X. Lv, Y. H. Ng and A. K. An, *Chem. Eng. J.*, 2019, **378**, 122137.
104 G. Zaragoza, A. Ruiz-Aguirre and E. Guillén-Burrieza, *Appl. Energy*, 2014, **130**, 491–499.
105 M. Khayet, *Desalination*, 2013, **308**, 89–101.
106 M. A. E.-R. Abu-Zeid, Y. Zhang, H. Dong, L. Zhang, H.-L. Chen and L. Hou, *Desalination*, 2015, **356**, 1–14.
107 I. Hitsov, T. Maere, K. De Sitter, C. Dotremont and I. Nopens, *Sep. Purif. Technol.*, 2015, **142**, 48–64.
108 M. Khayet, C. Cojocaru and A. Baroudi, *Desalination*, 2012, **287**, 159–166.
109 M. Qtaishat, T. Matsuura, B. Kruczek and M. Khayet, *Desalination*, 2008, **219**, 272–292.
110 S. O. Olatunji and L. M. Camacho, *Front. Energy Res.*, 2018, **6**, 130.
111 J. Deshpande, K. Nithyanandam and R. Pitchumani, *J. Membr. Sci.*, 2017, **523**, 301–316.
112 M. Essalhi and M. Khayet, *Sep. Purif. Technol.*, 2014, **133**, 176–186.
113 X. Wu, G. Y. Chen, G. Owens, D. Chu and H. Xu, *Mater. Today Energy*, 2019, **12**, 277–296.
114 X. Niu, X. Hu, S. Chu and Q. Gong, *Adv. Opt. Mater.*, 2018, **6**, 1701292.
115 A. Ciattoni, A. Marini, C. Rizza, M. Scalora and F. Biancalana, *Phys. Rev. A*, 2013, **87**, 53853.
116 S. Campione, I. Brener and F. Marquier, *Phys. Rev. B*, 2015, **91**, 121408.
117 T. Low, A. Chaves, J. D. Caldwell, A. Kumar, N. X. Fang, P. Avouris, T. F. Heinz, F. Guinea, L. Martin-Moreno and F. Koppens, *Nat. Mater.*, 2017, **16**, 182–194.
118 E. Ozbay, *Science*, 2006, **311**, 189–193.
119 Q. Bao and K. P. Loh, *ACS Nano*, 2012, **6**, 3677–3694.

120 P. Avouris and M. Freitag, *IEEE J. Sel. Top. Quantum Electron.*, 2014, **20**, 72–83.
121 C. W. Berry, N. Wang, M. R. Hashemi, M. Unlu and M. Jarrahi, *Nat. Commun.*, 2013, **4**, 1622.
122 A. Politano, L. Viti and M. S. Vitiello, *APL Mater.*, 2017, **5**, 35504.
123 Z. Liang, J. Sun, Y. Jiang, L. Jiang and X. Chen, *Plasmonics*, 2014, **9**, 859–866.
124 V. Cebrián, F. Martín-Saavedra, L. Gómez, M. Arruebo, J. Santamaria and N. Vilaboa, *Nanomedicine*, 2013, **9**, 646–656.
125 J. Z. Zhang, *J. Phys. Chem. Lett.*, 2010, **1**, 686–695.
126 W.-C. Law, K.-T. Yong, A. Baev and P. N. Prasad, *ACS Nano*, 2011, **5**, 4858–4864.
127 M. R. K. Ali, H. R. Ali, C. R. Rankin and M. A. El-Sayed, *Biomaterials*, 2016, **102**, 1–8.
128 R. Sundararaman, P. Narang, A. S. Jermyn, W. A. Goddard III and H. A. Atwater, *Nat. Commun.*, 2014, **5**, 5788.
129 A. M. Brown, R. Sundararaman, P. Narang, W. A. Goddard and H. A. Atwater, *ACS Nano*, 2016, **10**, 957–966.
130 M. L. Brongersma, N. J. Halas and P. Nordlander, *Nat. Nanotechnol.*, 2015, **10**, 25–34.
131 J. Liang, H. Liu, J. Yu, L. Zhou and J. Zhu, *Nanophotonics*, 2019, **8**, 771–786.
132 G. Baffou and R. Quidant, *Laser Photon. Rev.*, 2013, **7**, 171–187.
133 J. Gargiulo, R. Berté, Y. Li, S. A. Maier and E. Cortés, *Acc. Chem. Res.*, 2019, **52**, 2525–2535.
134 C. Zhan, X.-J. Chen, Y.-F. Huang, D.-Y. Wu and Z.-Q. Tian, *Acc. Chem. Res.*, 2019, **52**, 2784–2792.
135 H.-K. Choi, K. S. Lee, H.-H. Shin, J.-J. Koo, G. J. Yeon and Z. H. Kim, *Acc. Chem. Res.*, 2019, **52**, 3008–3017.
136 C. J. Murphy, H.-H. Chang, P. Falagan-Lotsch, M. T. Gole, D. M. Hofmann, K. N. L. Hoang, S. M. McClain, S. M. Meyer, J. G. Turner, M. Unnikrishnan, M. Wu, X. Zhang and Y. Zhang, *Acc. Chem. Res.*, 2019, **52**, 2124–2135.
137 H.-Y. Ahn, S. Yoo, N. H. Cho, R. M. Kim, H. Kim, J.-H. Huh, S. Lee and K. T. Nam, *Acc. Chem. Res.*, 2019, **52**, 2768–2783.
138 B. Khlebtsov, V. Zharov, A. Melnikov, V. Tuchin and N. Khlebtsov, *Nanotechnology*, 2006, **17**, 5167–5179.
139 H. Chen, L. Shao, T. Ming, Z. Sun, C. Zhao, B. Yang and J. Wang, *Small*, 2010, **6**, 2272–2280.
140 G. Baffou and R. Quidant, *Laser Photonics Rev.*, 2013, **7**, 171–187.
141 A. Politano, A. Cupolillo, G. Di Profio, H. A. Arafat, G. Chiarello and E. Curcio, *J. Phys.: Condens. Matter*, 2016, **28**, 363003.
142 S. Agnihotri, S. Mukherji and S. Mukherji, *RSC Adv.*, 2014, **4**, 3974–3983.
143 G. Baffou, R. Quidant and F. J. García De Abajo, *ACS Nano*, 2010, **4**, 709–716.
144 A. O. Govorov, W. Zhang, T. Skeini, H. Richardson, J. Lee and N. A. Kotov, *Nanoscale Res. Lett.*, 2006, **1**, 84.
145 H. H. Richardson, M. T. Carlson, P. J. Tandler, P. Hernandez and A. O. Govorov, *Nano Lett.*, 2009, **9**, 1139–1146.
146 G. Baffou, P. Berto, E. Bermúdez Ureña, R. Quidant, S. Monneret, J. Polleux and H. Rigneault, *ACS Nano*, 2013, **7**, 6478–6488.
147 J. T. Jørgensen, K. Norregaard, P. Tian, P. M. Bendix, A. Kjaer and L. B. Oddershede, *Sci. Rep.*, 2016, **6**, 30076.
148 D. Elmaghraoui, A. Politano and S. Jaziri, *J. Chem. Phys.*, 2020, **152**, 114102.
149 L. Durdevic, H. M. L. Robert, B. Wattellier, S. Monneret and G. Baffou, *Sci. Rep.*, 2019, **9**, 4644.
150 G. Baffou, P. Bon, J. Savatier, J. Polleux, M. Zhu, M. Merlin, H. Rigneault and S. Monneret, *ACS Nano*, 2012, **6**, 2452–2458.
151 Q. Jiang, B. Rogez, J.-B. Claude, G. Baffou and J. Wenger, *ACS Photonics*, 2019, **6**, 1763–1773.
152 G. Baffou, M. P. Kreuzer, F. Kulzer and R. Quidant, *Opt. Express*, 2009, **17**, 3291–3298.
153 G. Baffou, *Thermoplasmonics: Heating Metal Nanoparticles Using Light*, Cambridge University Press, 2017, pp. 101–142.
154 S. Santoro, A. J. Moro, C. Portugal, J. G. Crespo, J. C. Lima and I. M. Coelhoso, *J. Food Eng.*, 2016, **189**, 37–44.
155 G. Naik, J. Kim, N. Kinsey and A. Boltasseva, in *Modern Plasmonics*, ed. N. V. Richardson and S. Holloway, North-Holland, 2014, vol. 4, pp. 189–221.
156 A. Boltasseva and H. A. Atwater, *Science*, 2011, **331**, 290–291.
157 M. Rocca, *Surf. Sci. Rep.*, 1995, **22**, 1–71.
158 A. Politano, V. Formoso and G. Chiarello, *Plasmonics*, 2008, **3**, 165.
159 H. Ditlbacher, A. Hohenau, D. Wagner, U. Kreibig, M. Rogers, F. Hofer, F. R. Aussenegg and J. R. Krenn, *Phys. Rev. Lett.*, 2005, **95**, 257403.
160 M. G. Blaber, M. D. Arnold and M. J. Ford, *J. Phys.: Condens. Matter*, 2010, **22**, 143201.
161 G. H. Chan, J. Zhao, G. C. Schatz and R. P. Van Duyne, *J. Phys. Chem. C*, 2008, **112**, 13958–13963.
162 L. Zhou, Y. Tan, J. Wang, W. Xu, Y. Yuan, W. Cai, S. Zhu and J. Zhu, *Nat. Photonics*, 2016, **10**, 393–398.
163 P. R. West, S. Ishii, G. V. Naik, N. K. Emani, V. M. Shalaev and A. Boltasseva, *Laser Photon. Rev.*, 2010, **4**, 795–808.
164 M. I. Stockman, *Opt. Express*, 2011, **19**, 22029–22106.
165 J. M. Sanz, D. Ortiz, R. Alcaraz de la Osa, J. M. Saiz, F. González, A. S. Brown, M. Losurdo, H. O. Everitt and F. Moreno, *J. Phys. Chem. C*, 2013, **117**, 19606–19615.
166 A. Lalisse, G. Tessier, J. Plain and G. Baffou, *J. Phys. Chem. C*, 2015, **119**, 25518–25528.
167 P. B. Johnson and R. W. Christy, *Phys. Rev. B*, 1972, **6**, 4370–4379.
168 E. D. Palik, *Handbook of optical constants of solids*, Academic Press, Orlando, 1985.
169 M. D. Mcmahon, R. Lopez, H. M. Meyer, L. C. Feldman and R. F. Haglund, *Appl. Phys. B*, 2005, **80**, 915–921.
170 A. Loiseau, V. Asila, G. Boitel-Aullen, M. Lam, M. Salmain and S. Boujday, *Biosensors*, 2019, **9**, 1–40.
171 G. A. Sotiriou, G. D. Etterlin, A. Spyrogianni, F. Krumeich, J.-C. Leroux and S. E. Pratsinis, *Chem. Commun.*, 2014, **50**, 13559–13562.
172 K. Kalimuthu, B. S. Cha, S. Kim and K. S. Park, *Microchem. J.*, 2020, **152**, 104296.

173 V. Amendola, R. Pilot, M. Frasconi, O. M. Maragò and M. A. Iatì, *J. Phys.: Condens. Matter*, 2017, **29**, 203002.
174 I. Fabijanić, V. Janicki, J. Ferré-Borrull, M. Bubaš, V. Blažek Bregović, L. F. Marsal and J. Sancho-Parramon, *Coatings*, 2019, **9**, 382.
175 M. D. Susman, Y. Feldman, A. Vaskevich and I. Rubinstein, *Chem. Mater.*, 2012, **24**, 2501–2508.
176 V. G. Kravets, R. Jalil, Y.-J. Kim, D. Ansell, D. E. Aznakayeva, B. Thackray, L. Britnell, B. D. Belle, F. Withers, I. P. Radko, Z. Han, S. I. Bozhevolnyi, K. S. Novoselov, A. K. Geim and A. N. Grigorenko, *Sci. Rep.*, 2014, **4**, 5517.
177 V. Amendola, R. Saija, O. M. Maragò and M. A. Iatì, *Nanoscale*, 2015, **7**, 8782–8792.
178 S. Sarina, H. Zhu, E. Jaatinen, Q. Xiao, H. Liu, J. Jia, C. Chen and J. Zhao, *J. Am. Chem. Soc.*, 2013, **135**, 5793–5801.
179 T. Lin, C. Yang, Z. Wang, H. Yin, X. Lü, F. Huang, J. Lin, X. Xie and M. Jiang, *Energy Environ. Sci.*, 2014, **7**, 967–972.
180 M. Ye, J. Jia, Z. Wu, C. Qian, R. Chen, P. G. O'Brien, W. Sun, Y. Dong and G. A. Ozin, *Adv. Energy Mater.*, 2017, **7**, 1601811.
181 J. Wang, Y. Li, L. Deng, N. Wei, Y. Weng, S. Dong, D. Qi, J. Qiu, X. Chen and T. Wu, *Adv. Mater.*, 2017, **29**, 1603730.
182 M. Li, U. Guler, Y. Li, A. Rea, E. K. Tanyi, Y. Kim, M. A. Noginov, Y. Song, A. Boltasseva, V. M. Shalaev and N. A. Kotov, *ACS Energy Lett.*, 2018, **3**, 1578–1583.
183 T. N. Lambert, N. L. Andrews, H. Gerung, T. J. Boyle, J. M. Oliver, B. S. Wilson and S. M. Han, *Small*, 2007, **3**, 691–699.
184 C. Lee, H. Kim, C. Hong, M. Kim, S. S. Hong, D. H. Lee and W. I. Lee, *J. Mater. Chem.*, 2008, **18**, 4790–4795.
185 D. D. Vaughn and R. E. Schaak, *Chem. Soc. Rev.*, 2013, **42**, 2861–2879.
186 I. Kriegel, F. Scotognella and L. Manna, *Phys. Rep.*, 2017, **674**, 1–52.
187 Y. Li, W. Lu, Q. Huang, C. Li and W. Chen, *Nanomedicine*, 2010, **5**, 1161–1171.
188 S. Ghosh, T. Avellini, A. Petrelli, I. Kriegel, R. Gaspari, G. Almeida, G. Bertoni, A. Cavalli, F. Scotognella, T. Pellegrino and L. Manna, *Chem. Mater.*, 2016, **28**, 4848–4858.
189 C. Yan, Q. Tian and S. Yang, *RSC Adv.*, 2017, **7**, 37887–37897.
190 X. Yang, Y. Yang, L. Fu, M. Zou, Z. Li, A. Cao and Q. Yuan, *Adv. Funct. Mater.*, 2018, **28**, 1704505.
191 H. Li, Y. He, Y. Hu and X. Wang, *ACS Appl. Mater. Interfaces*, 2018, **10**, 9362–9368.
192 C. S. Yung, N. A. Tomlin, K. Heuerman, M. W. Keller, M. G. White, M. Stephens and J. H. Lehman, *Carbon N. Y.*, 2018, **127**, 195–201.
193 J. Lehman, A. Sanders, L. Hanssen, B. Wilthan, J. Zeng and C. Jensen, *Nano Lett.*, 2010, **10**, 3261–3266.
194 C. Chen, Y. Li, J. Song, Z. Yang, Y. Kuang, E. Hitz, C. Jia, A. Gong, F. Jiang, J. Y. Zhu, B. Yang, J. Xie and L. Hu, *Adv. Mater.*, 2017, **29**, 1701756.
195 A. A. Balandin, *Nat. Mater.*, 2011, **10**, 569–581.
196 B. Han, Y. Zhang, Q. Chen and H. Sun, *Adv. Funct. Mater.*, 2018, **28**, 1802235.
197 G. Fugallo, A. Cepellotti, L. Paulatto, M. Lazzeri, N. Marzari and F. Mauri, *Nano Lett.*, 2014, **14**, 6109–6114.
198 J. Chen, X. Wang and T. Chen, *Nanoscale Res. Lett.*, 2014, **9**, 86.
199 X. Wang, Y. He, G. Cheng, L. Shi, X. Liu and J. Zhu, *Energy Convers. Manage.*, 2016, **130**, 176–183.
200 X. Yu, X. Cai, H. Cui, S.-W. Lee, X.-F. Yu and B. Liu, *Nanoscale*, 2017, **9**, 17859–17864.
201 H. Lin, X. Wang, L. Yu, Y. Chen and J. Shi, *Nano Lett.*, 2017, **17**, 384–391.
202 F. Shahzad, M. Alhabeb, C. B. Hatter, B. Anasori, S. Man Hong, C. M. Koo and Y. Gogotsi, *Science*, 2016, **353**, 1137–1140.
203 X. Zhao, L.-M. Peng, C.-Y. Tang, J.-H. Pu, X.-J. Zha, K. Ke, R.-Y. Bao, M.-B. Yang and W. Yang, *Mater. Horiz.*, 2020, **7**, 855–865.
204 J. K. El-Demellawi, S. Lopatin, J. Yin, O. F. Mohammed and H. N. Alshareef, *ACS Nano*, 2018, **12**, 8485–8493.
205 D. Xu, Z. Li, L. Li and J. Wang, *Adv. Funct. Mater.*, 2020, **30**, 2000712.
206 M. Alhabeb, K. Maleski, B. Anasori, P. Lelyukh, L. Clark, S. Sin and Y. Gogotsi, *Chem. Mater.*, 2017, **29**, 7633–7644.
207 P. Lakhe, E. M. Prehn, T. Habib, J. L. Lutkenhaus, M. Radovic, M. S. Mannan and M. J. Green, *Ind. Eng. Chem. Res.*, 2019, **58**, 1570–1579.
208 J. Li, X. Li and B. der Bruggen, *Environ. Sci.: Nano*, 2020, **7**, 1289–1304.
209 B. Y. Li and Y. Zou, *Adv. Mater.*, 2008, **20**, 2952–2958.
210 B.-P. Jiang, L. Zhang, Y. Zhu, X.-C. Shen, S.-C. Ji, X.-Y. Tan, L. Cheng and H. Liang, *J. Mater. Chem. B*, 2015, **3**, 3767–3776.
211 Q. Zou, J. Huang and X. Zhang, *Small*, 2018, **14**, 1803101.
212 S. Huang, Q. He, S. Xu and L. Wang, *Anal. Chem.*, 2015, **87**, 5451–5456.
213 M. Gizdavic-nikolaidis, J. Travas-sejdic, G. A. Bowmaker, R. P. Cooney and P. A. Kilmartin, *Synth. Met.*, 2004, **140**, 225–232.
214 H. Sun, F. Lv, L. Liu, Q. Gu and S. Wang, *Adv. Ther.*, 2018, **1**, 1800057.
215 J. Yang, J. Choi, D. Bang, E. Kim, E.-K. Lim, H. Park, J.-S. Suh, K. Lee, K.-H. Yoo, E.-K. Kim, Y.-M. Huh and S. Haam, *Angew. Chem., Int. Ed.*, 2011, **50**, 441–444.
216 Z. Zha, X. Yue, Q. Ren and Z. Dai, *Adv. Mater.*, 2013, **25**, 777–782.
217 K. Turcheniuk, T. Dumych, R. Bilyy, V. Turcheniuk, J. Bouckaert, V. Vovk, V. Chopyak, V. Zaitsev, P. Mariot, N. Prevarskaya, R. Boukherroub and S. Szunerits, *RSC Adv.*, 2016, **6**, 1600–1610.
218 H. Chen, M. C. Roco and J. Son, *J. Nanopart. Res.*, 2013, **15**, 1951.
219 B. Henderson-Sellers, *Q. J. R. Meteorol. Soc.*, 1984, **110**, 1186–1190.
220 X. Wang, G. Ou, N. Wang and H. Wu, *ACS Appl. Mater. Interfaces*, 2016, **8**, 9194–9199.
221 Z. Hong, J. Pei, Y. Wang, B. Cao, M. Mao, H. Liu, H. Jiang, Q. An, X. Liu and X. Hu, *Energy Convers. Manage.*, 2019, **199**, 112019.
222 A. Iqbal, M. S. Mahmoud, E. T. Sayed, K. Elsaid, M. A. Abdelkareem, H. Alawadhi and A. G. Olabi, *J. Environ. Manage.*, 2021, **277**, 111415.

223 Z. Li, W. Cai, X. Wang, Y. Hu and Z. Gui, *J. Colloid Interface Sci.*, 2021, **582**, 496–505.
224 Y. Zeng, J. Yao, B. A. Horri, K. Wang, Y. Wu, D. Li and H. Wang, *Energy Environ. Sci.*, 2011, **4**, 4074–4078.
225 X. Wang, Y. He, X. Liu, L. Shi and J. Zhu, *Sol. Energy*, 2017, **157**, 35–46.
226 M. Gao, C. K. Peh, H. T. Phan, L. Zhu and G. W. Ho, *Adv. Energy Mater.*, 2018, **8**, 1800711.
227 Z. Gan, Z. Chen, L. Liu, L. Zhang, W. Tu and Y. Liu, *Sol. RRL*, 2017, **1**, 1600032.
228 A. H. Elsheikh, S. W. Sharshir, M. Kamal, A. Ali and J. Shaibo, *Sol. Energy*, 2019, **177**, 561–575.
229 G. Ni, S. H. Zandavi, S. M. Javid, S. V. Boriskina, T. A. Cooper and G. Chen, *Energy Environ. Sci.*, 2018, **11**, 1510–1519.
230 R. Enright, N. Miljkovic, J. L. Alvarado, K. Kim and J. W. Rose, *Nanoscale Microscale Thermophys. Eng.*, 2014, **18**, 223–250.
231 R. N. Wenzel, *Ind. Eng. Chem.*, 1936, **28**, 988–994.
232 A. B. D. Cassie and S. Baxter, *Trans. Faraday Soc.*, 1944, **40**, 546–551.
233 A. Aili, Q. Ge and T. Zhang, *J. Heat Transfer*, 2017, **139**, 112401–112411.
234 E. Curcio, X. Ji, G. Di Profio, A. O. Sulaiman, E. Fontananova and E. Drioli, *J. Membr. Sci.*, 2010, **346**, 263–269.
235 S. Cao, P. Rathi, X. Wu, D. Ghim, Y.-S. Jun and S. Singamaneni, *Adv. Mater.*, 2020, 2000922.
236 F. E. Ahmed, R. Hashaikeh and N. Hilal, *Desalination*, 2019, **453**, 54–76.
237 A. Amri, Z. T. Jiang, T. Pryor, C.-Y. Yin and S. Djordjevic, *Renewable Sustainable Energy Rev.*, 2014, **36**, 316–328.
238 X. Wang, Y. He, X. Liu, G. Cheng and J. Zhu, *Appl. Energy*, 2017, **195**, 414–425.
239 J. Chen, J. Feng, Z. Li, P. Xu, X. Wang, W. Yin, M. Wang, X. Ge and Y. Yin, *Nano Lett.*, 2019, **19**, 400–407.
240 L. Yi, S. Ci, S. Luo, P. Shao, Y. Hou and Z. Wen, *Nano Energy*, 2017, **41**, 600–608.
241 X. Wang, Y. He, X. Liu and J. Zhu, *Powder Technol.*, 2017, **321**, 276–285.
242 Y. Wang, C. Wang, X. Song, S. K. Megarajan and H. Jiang, *J. Mater. Chem. A*, 2018, **6**, 963–971.
243 X. Han, W. Wang, K. Zuo, L. Chen, L. Yuan, J. Liang, Q. Li, P. M. Ajayan, Y. Zhao and J. Lou, *Nano Energy*, 2019, **60**, 567–575.
244 Y. Shi, R. Li, Y. Jin, S. Zhuo, L. Shi, J. Chang, S. Hong, K.-C. Ng and P. Wang, *Joule*, 2018, **2**, 1171–1186.
245 Y. Wang, C. Wang, X. Song, M. Huang, S. K. Megarajan, S. F. Shaukat and H. Jiang, *J. Mater. Chem. A*, 2018, **6**, 9874–9881.
246 S. Hong, Y. Shi, R. Li, C. Zhang, Y. Jin and P. Wang, *ACS Appl. Mater. Interfaces*, 2018, **10**, 28517–28524.
247 X. Gao, H. Ren, J. Zhou, R. Du, C. Yin, R. Liu, H. Peng, L. Tong, Z. Liu and J. Zhang, *Chem. Mater.*, 2017, **29**, 5777–5781.
248 H. Sun, X. Li, J. Chen, H. Zhu, H. Miao, Y. Li, X. Liu and G. Shi, *Soft Matter*, 2021, **17**, 4730–4737.
249 M. Keshavarz Hedayati and M. Elbahri, *Materials*, 2016, **9**, 497.
250 Refractive index of polymers by index, **https://scipoly.com/technical-library/refractive-index-of-polymers-by-index**.
251 E. Curcio and E. Drioli, *Sep. Purif. Rev.*, 2005, **34**, 35–86.
252 X. Wu, Q. Jiang, D. Ghim, S. Singamaneni and Y.-S. Jun, *J. Mater. Chem. A*, 2018, **6**, 18799–18807.
253 Y. Z. Tan, E. H. Ang and J. W. Chew, *J. Membr. Sci.*, 2019, **572**, 171–183.
254 Renewable Resource Data Center, Reference solar spectral irradiance: ASTM G-173, 2009.
255 W. Wien and O. Lummer, *Ann. Phys.*, 1895, **292**, 451–456.
256 J. Y. Lu, S. H. Nam, K. Wilke, A. Raza, Y. E. Lee, A. AlGhaferi, N. X. Fang and T. Zhang, *Adv. Opt. Mater.*, 2016, **4**, 1255–1264.
257 K.-T. Lin, H. Lin, T. Yang and B. Jia, *Nat. Commun.*, 2020, **11**, 1389.
258 G. Ni, G. Li, S. V. Boriskina, H. Li, W. Yang, T. Zhang and G. Chen, *Nat. Energy*, 2016, **1**, 16126.
259 X. Li, R. Lin, G. Ni, N. Xu, X. Hu, B. Zhu, G. Lv, J. Li, S. Zhu and J. Zhu, *Natl. Sci. Rev.*, 2017, **5**, 70–77.
260 K. Pietrak and T. S. Winiewski, *J. Power Technol*, 2014, **95**, 14–24.
261 Y. Fu, J. Hansson, Y. Liu, S. Chen, A. Zehri, M. K. Samani, N. Wang, Y. Ni, Y. Zhang, Z.-B. Zhang, Q. Wang, M. Li, H. Lu, M. Sledzinska, C. M. S. Torres, S. Volz, A. A. Balandin, X. Xu and J. Liu, *2D Mater.*, 2019, **7**, 12001.
262 M. Seyhan, C. L. Altan, B. Gurten and S. Bucak, *AIP Adv.*, 2017, **7**, 45101.
263 G. Langer, J. Hartmann and M. Reichling, *Rev. Sci. Instrum.*, 1997, **68**, 1510–1513.
264 B. Kumanek and D. Janas, *J. Mater. Sci.*, 2019, **54**, 7397–7427.
265 R. Yan, J. R. Simpson, S. Bertolazzi, J. Brivio, M. Watson, X. Wu, A. Kis, T. Luo, A. R. Hight Walker and H. G. Xing, *ACS Nano*, 2014, **8**, 986–993.
266 Y. Li, T. Zhang, Y. Qin, T. Day, G. Jeffrey Snyder, X. Shi and L. Chen, *J. Appl. Phys.*, 2014, **116**, 203705.
267 B. A. Lunn, J. Unsworth, N. G. Booth and P. C. Innis, *J. Mater. Sci.*, 1993, **28**, 5092–5098.
268 G. Wang, Y. Fu, X. Ma, W. Pi, D. Liu and X. Wang, *Carbon*, 2017, **114**, 117–124.
269 G. Wang, Y. Fu, A. Guo, T. Mei, J. Wang, J. Li and X. Wang, *Chem. Mater.*, 2017, **29**, 5629–5635.
270 F. Jiang, H. Liu, Y. Li, Y. Kuang, X. Xu, C. Chen, H. Huang, C. Jia, X. Zhao, E. Hitz, Y. Zhou, R. Yang, L. Cui and L. Hu, *ACS Appl. Mater. Interfaces*, 2018, **10**, 1104–1112.
271 Q. Chen, Z. Pei, Y. Xu, Z. Li, Y. Yang, Y. Wei and Y. Ji, *Chem. Sci.*, 2018, **9**, 623–628.
272 X. Wu, M. E. Robson, J. L. Phelps, J. S. Tan, B. Shao, G. Owens and H. Xu, *Nano Energy*, 2019, **56**, 708–715.
273 X. Li, W. Xu, M. Tang, L. Zhou, B. Zhu, S. Zhu and J. Zhu, *Proc. Natl. Acad. Sci. U. S. A.*, 2016, **113**, 13953–13958.
274 F. Domínguez-Muñoz, B. Anderson, J. M. Cejudo-López and A. Carrillo-Andrés, *Energy Build.*, 2010, **42**, 2159–2168.
275 X. Lin, M. Yang, W. Hong, D. Yu and X. Chen, *Front. Mater.*, 2018, **5**, 74.

276 N. N. Hamadneh, W. S. Khan and W. A. Khan, *J. King Saud Univ. Sci.*, 2019, **31**, 618–627.
277 X. Hu, W. Xu, L. Zhou, Y. Tan, Y. Wang, S. Zhu and J. Zhu, *Adv. Mater.*, 2017, **29**, 1604031.
278 A. Politano, P. Argurio, G. Di Profio, V. Sanna, A. Cupolillo, S. Chakraborty, H. A. Arafat and E. Curcio, *Adv. Mater.*, 2017, **29**, 1603504.
279 Z. Hua, B. Li, L. Li, X. Yin, K. Chen and W. Wang, *J. Phys. Chem. C*, 2017, **121**, 60–69.
280 A. H. Avci, S. Santoro, A. Politano, M. Propato, M. Micieli, M. Aquino, Z. Wenjuan and E. Curcio, *Chem. Eng. Process. – Process Intensif.*, 2021, **164**, 108382.
281 T. Li, Q. Fang, H. Lin and F. Liu, *J. Mater. Chem. A*, 2019, **7**, 17505–17515.
282 J. Zhao, Y. Yang, C. Yang, Y. Tian, Y. Han, J. Liu, X. Yin and W. Que, *J. Mater. Chem. A*, 2018, **6**, 16196–16204.
283 A. P. Bell, J. A. Fairfield, E. K. McCarthy, S. Mills, J. J. Boland, G. Baffou and D. McCloskey, *ACS Nano*, 2015, **9**, 5551–5558.
284 P. B. Roder, B. E. Smith, E. J. Davis and P. J. Pauzauskie, *J. Phys. Chem. C*, 2014, **118**, 1407–1416.
285 G. Baffou, R. Quidant and C. Girard, *Appl. Phys. Lett.*, 2009, **94**, 153109.
286 T. Ma, C. Yang, W. Guo, H. Lin, F. Zhang, H. Liu, L. Zhao, Y. Zhang, Y. Wang, Y. Cui, J. Zhao and F. Qu, *ACS Appl. Mater. Interfaces*, 2020, **12**, 27140–27149.
287 Y. Chang, Z. Wang, Y. Shi, X. Ma, L. Ma, Y. Zhang and J. Zhan, *J. Mater. Chem. A*, 2018, **6**, 10939–10946.
288 T. Gao, Y. Li, C. Chen, Z. Yang, Y. Kuang, C. Jia, J. Song, E. M. Hitz, B. Liu, H. Huang, J. Yu, B. Yang and L. Hu, *Small Methods*, 2019, **3**, 1800176.
289 X. Wang, Y. He and X. Liu, *Energy Convers. Manage.*, 2018, **173**, 158–166.
290 W. Xu, X. Hu, S. Zhuang, Y. Wang, X. Li, L. Zhou, S. Zhu and J. Zhu, *Adv. Energy Mater.*, 2018, **8**, 1702884.
291 C. Wang, Y. Wang, X. Song, M. Huang and H. Jiang, *Adv. Sustainable Syst.*, 2019, **3**, 1800108.
292 H.-H. Yu, L.-J. Yan, Y.-C. Shen, S.-Y. Chen, H.-N. Li, J. Yang and Z.-K. Xu, *Research*, 2020, **2020**, 3241758.
293 I. A. Said, S. Wang and Q. Li, *Ind. Eng. Chem. Res.*, 2019, **58**, 18829–18835.
294 P. D. Dongare, A. Alabastri, S. Pedersen, K. R. Zodrow, N. J. Hogan, O. Neumann, J. Wu, T. Wang, A. Deshmukh, M. Elimelech, Q. Li, P. Nordlander and N. J. Halas, *Proc. Natl. Acad. Sci. U. S. A.*, 2017, **114**, 6936–6941.
295 W. Li, Y. Chen, L. Yao, X. Ren, Y. Li and L. Deng, *Desalination*, 2020, **478**, 114288.
296 J. Huang, Y. Hu, Y. Bai, Y. He and J. Zhu, *Desalination*, 2020, **489**, 114529.
297 Y. Z. Tan, H. Wang, L. Han, M. B. Tanis-Kanbur, M. V. Pranav and J. W. Chew, *J. Membr. Sci.*, 2018, **565**, 254–265.
298 M. U. Farid, J. A. Kharraz and A. K. An, *ACS Appl. Mater. Interfaces*, 2021, **13**, 3805–3815.
299 Y. Peng, Y. Wang, W. Li and J. Jin, *J. Mater. Chem. A*, 2021, **9**, 10678–10684.
300 W. Li, L. Deng, H. Huang, J. Zhou, Y. Liao, L. Qiu, H. Yang and L. Yao, *ACS Appl. Mater. Interfaces*, 2021, **13**, 26861–26869.
301 S. Cao, X. Wu, Y. Zhu, R. Gupta, A. Tan, Z. Wang, Y.-S. Jun and S. Singamaneni, *J. Mater. Chem. A*, 2020, **8**, 5147–5156.
302 Q. Huang, S. Gao, Y. Huang, M. Zhang and C. Xiao, *J. Membr. Sci.*, 2019, **582**, 203–210.
303 J. Liu, H. Guo, Z. Sun and B. Li, *J. Membr. Sci.*, 2021, **634**, 119434.
304 Y. Zhang, K. Li, L. Liu, K. Wang, J. Xiang, D. Hou and J. Wang, *Chemosphere*, 2020, **256**, 127053.
305 D. Ghim, X. Wu, M. Suazo and Y.-S. Jun, *Nano Energy*, 2021, **80**, 105444.
306 Y.-S. Jun, X. Wu, D. Ghim, Q. Jiang, S. Cao and S. Singamaneni, *Acc. Chem. Res.*, 2019, **52**, 1215–1225.
307 X. Wu, S. Cao, D. Ghim, Q. Jiang, S. Singamaneni and Y.-S. Jun, *Nano Energy*, 2021, **79**, 105353.
308 J. Wu, K. R. Zodrow, P. B. Szemraj and Q. Li, *J. Mater. Chem. A*, 2017, **5**, 23712–23719.
309 M. Drobek, A. Figoli, S. Santoro, N. Navascués, J. Motuzas, S. Simone, C. Algieri, N. Gaeta, L. Querze, A. Trotta, G. Barbieri, R. Mallada, A. Julbe and E. Drioli, *Microporous Mesoporous Mater.*, 2015, **207**, 126–133.
310 M. R. Esfahani, S. A. Aktij, Z. Dabaghian, M. D. Firouzjaei, A. Rahimpour, J. Eke, I. C. Escobar, M. Abolhassani, L. F. Greenlee, A. R. Esfahani, A. Sadmani and N. Koutahzadeh, *Sep. Purif. Technol.*, 2019, **213**, 465–499.
311 A. Politano, G. Di Profio, E. Fontananova, V. Sanna, A. Cupolillo and E. Curcio, *Desalination*, 2019, **451**, 192–199.
312 G. Guan, R. Wang, F. Wicaksana, X. Yang and A. G. Fane, *Ind. Eng. Chem. Res.*, 2012, **51**, 13405–13413.
313 Y. Liao, R. Wang, M. Tian, C. Qiu and A. G. Fane, *J. Membr. Sci.*, 2013, **425–426**, 30–39.
314 X. Wu, Q. Jiang, D. Ghim, S. Singamaneni and Y. S. Jun, *J. Mater. Chem. A*, 2018, **6**, 18799–18807.
315 X. Huang, Y.-H. Yu, O. L. de Llergo, S. M. Marquez and Z. Cheng, *RSC Adv.*, 2017, **7**, 9495–9499.
316 M. Wu, S. Ding, L. Deng and X. Wang, *Sep. Purif. Technol.*, 2022, **281**, 119995.
317 S. K. Das, *Chem. Eng. Sci.*, 2019, **203**, 293–301.
318 I.-L. Ngo, S. Jeon and C. Byon, *Int. J. Heat Mass Transf.*, 2016, **98**, 219–226.
319 D. M. Warsinger, J. Swaminathan, E. Guillen-Burrieza, H. A. Arafat and J. H. Lienhard V, *Desalination*, 2015, **356**, 294–313.
320 M. Gryta, *Desalination*, 2007, **216**, 88–102.
321 H. W. Warsinger, C. Martin, D. Swaminathan, J. Chung, D. M. Jeong, S. Lienhard, J. H. Martin Warsinger and D. Warsinger, *Int. Desalin. Assoc.*, 2015, 0–14.
322 M. Gryta, M. Tomaszewska, J. Grzechulska and A. W. Morawski, *J. Membr. Sci.*, 2001, **181**, 279–287.
323 M. Khayet, A. Velázquez and J. I. Mengual, *J. Membr. Sci.*, 2004, **240**, 123–128.
324 Y.-F. Yang, Y. Li, Q.-L. Li, L.-S. Wan and Z.-K. Xu, *J. Membr. Sci.*, 2010, **362**, 255–264.
325 M. Krivorot, A. Kushmaro, Y. Oren and J. Gilron, *J. Membr. Sci.*, 2011, **376**, 15–24.

326 L. D. Tijing, Y. C. Woo, J. S. Choi, S. Lee, S. H. Kim and H. K. Shon, *J. Membr. Sci.*, 2015, **475**, 215–244.
327 T. Young, *Philos. Trans. R. Soc. Lond.*, 1805, **95**, 65–87.
328 C. J. Van Oss, M. K. Chaudhury and R. J. Good, *Chem. Rev.*, 1988, **88**, 927–941.
329 Z. Wang, Y. Chen, F. Zhang and S. Lin, *Desalination*, 2019, **450**, 46–53.
330 M. R. Choudhury, N. Anwar, D. Jassby and M. S. Rahaman, *Adv. Colloid Interface Sci.*, 2019, **269**, 370–399.
331 E. Guillen-Burrieza, M. O. Mavukkandy, M. R. Bilad and H. A. Arafat, *J. Membr. Sci.*, 2016, **515**, 163–174.
332 S. O. L. and, W. J. Lau, P. S. Goh and A. F. Ismail, *Membr. Water Treat.*, 2014, **5**, 14–29.
333 J. Kavitha, M. Rajalakshmi, A. R. Phani and M. Padaki, *J. Water Process Eng.*, 2019, **32**, 100926.
334 F. Qu, Z. Yan, H. Yu, G. Fan, H. Pang, H. Rong and J. He, *Desalination*, 2020, **486**, 114493.
335 F. He, K. K. Sirkar and J. Gilron, *J. Membr. Sci.*, 2009, **345**, 53–58.
336 J. Beltrán-Heredia, J. Sánchez-Martín and M. Barrado-Moreno, *Chem. Eng. J.*, 2012, **180**, 128–136.
337 M. A. Aboulhassan, S. Souabi, A. Yaacoubi and M. Baudu, *Int. J. Environ. Sci. Technol.*, 2006, **3**, 327–332.
338 T. Horseman, Y. Yin, K. S. S. Christie, Z. Wang, T. Tong and S. Lin, *ACS ES&T Eng*, 2021, **1**, 117–140.
339 B. Bhushan and Y. C. Jung, *Prog. Mater. Sci.*, 2011, **56**, 1–108.
340 J.-G. Lee, E.-J. Lee, S. Jeong, J. Guo, A. K. An, H. Guo, J. Kim, T. Leiknes and N. Ghaffour, *J. Membr. Sci.*, 2017, **526**, 395–408.
341 X. Fan, Y. Liu, X. Quan, H. Zhao, S. Chen, G. Yi and L. Du, *J. Membr. Sci.*, 2016, **514**, 501–509.
342 Y. C. Woo, L. D. Tijing, W.-G. Shim, J.-S. Choi, S.-H. Kim, T. He, E. Drioli and H. K. Shon, *J. Membr. Sci.*, 2016, **520**, 99–110.
343 R. Moradi, J. Karimi-Sabet, M. Shariaty-Niassar and M. A. Koochaki, *Polymers*, 2015, **7**, 1444–1463.
344 N. A. Zakaria, S. Q. Zaliman, C. P. Leo, A. L. Ahmad, B. S. Ooi and P. E. Poh, *J. Environ. Chem. Eng.*, 2022, **10**, 107346.
345 S. S. Ray, M. Gandhi, S.-S. Chen, H.-M. Chang, C. T. N. Dan and H. Q. Le, *Environ. Sci.: Water Res. Technol.*, 2018, **4**, 1612–1623.
346 M. Baghbanzadeh, D. Rana, C. Q. Lan and T. Matsuura, *Sep. Purif. Technol.*, 2016, **157**, 60–71.
347 Z.-Q. Dong, X.-H. Ma, Z.-L. Xu and Z.-Y. Gu, *RSC Adv.*, 2015, **5**, 67962–67970.
348 J. Li, L.-F. Ren, H. S. Zhou, J. Yang, J. Shao and Y. He, *J. Membr. Sci.*, 2021, **620**, 118924.
349 M. Wang, G. Liu, H. Yu, S.-H. Lee, L. Wang, J. Zheng, T. Wang, Y. Yun and J. K. Lee, *ACS Appl. Mater. Interfaces*, 2018, **10**, 13452–13461.
350 R. Mardosaitė, A. Jurkevičiūtė and S. Račkauskas, *Cryst. Growth Des.*, 2021, **21**, 4765–4779.
351 R. Huang, Z. Liu, Y. C. Woo, W. Luo, S. R. Gray and M. Xie, *Environ. Sci.: Water Res. Technol.*, 2020, **6**, 1786–1793.
352 Z. Xiao, R. Zheng, Y. Liu, H. He, X. Yuan, Y. Ji, D. Li, H. Yin, Y. Zhang, X.-M. Li and T. He, *Water Res.*, 2019, **155**, 152–161.
353 J. A. Kharraz and A. K. An, *J. Membr. Sci.*, 2020, **595**, 117596.
354 X. Liao, P. Dai, Y. Wang, X. Zhang, Y. Liao, X. You and A. G. Razaqpur, *J. Membr. Sci.*, 2022, **650**, 120423.
355 B. Gong, H. Yang, S. Wu, J. Yan, K. Cen, Z. Bo and K. K. Ostrikov, *ACS Sustainable Chem. Eng.*, 2019, **7**, 20151–20158.
356 W. Zhang, Y. Lu, J. Liu, X. Li, B. Li and S. Wang, *J. Membr. Sci.*, 2020, **595**, 117563.
357 S. Lin, S. Nejati, C. Boo, Y. Hu, C. O. Osuji and M. Elimelech, *Environ. Sci. Technol. Lett.*, 2014, **1**, 443–447.
358 B. J. Deka, J. Guo, N. K. Khanzada and A. K. An, *Water Res.*, 2019, **165**, 114982.
359 L.-H. Chen, A. Huang, Y.-R. Chen, C.-H. Chen, C.-C. Hsu, F.-Y. Tsai and K.-L. Tung, *Desalination*, 2018, **428**, 255–263.
360 Y.-R. Chen, R. Xin, X. Huang, K. Zuo, K.-L. Tung and Q. Li, *J. Membr. Sci.*, 2021, **620**, 118913.
361 S. Zhang, J. Chen, J. Zheng, X. Chen, H. Xu, F. I. T. Petrescu, L. M. Ungureanu, Y. Li and G. Shi, *Nanomaterials*, 2022, **12**, 859.
362 P. Vijaya Kumar, S. Mary Jelastin Kala and K. S. Prakash, *Mater. Lett.*, 2019, **236**, 19–22.
363 S. Cao, Q. Jiang, X. Wu, D. Ghim, H. Gholami Derami, P.-I. Chou, Y.-S. Jun and S. Singamaneni, *J. Mater. Chem. A*, 2019, **7**, 24092–24123.
364 S. Santoro, P. Timpano, A. H. Avci, P. Argurio, F. Chidichimo, M. De Biase, S. Straface and E. Curcio, *Desalination*, 2021, **520**, 115378.
365 D. J. Johnson and N. Hilal, *Desalination*, 2021, **500**, 114852.
366 Q. Ma, Z. Xu and R. Wang, *Water Res.*, 2021, **198**, 117154.
367 R. Fillet, V. Nicolas, V. Fierro and A. Celzard, *Sol. Energy Mater. Sol. Cells*, 2021, **219**, 110814.
368 Y. Liu, K. Ai and L. Lu, *Chem. Rev.*, 2014, **114**, 5057–5115.
369 S. Sun, B. Sun, Y. Wang, M. Fordjour Antwi-Afari, H.-Y. Mi, Z. Guo, C. Liu and C. Shen, *Sep. Purif. Technol.*, 2021, **278**, 119621.
370 Z. Wang, H.-C. Yang, F. He, S. Peng, Y. Li, L. Shao and S. B. Darling, *Matter*, 2019, **1**, 115–155.
371 I. R. Salmón and P. Luis, *Chem. Eng. Process. – Process Intensif.*, 2018, **123**, 258–271.
372 E. Drioli, G. Di Profio and E. Curcio, *Membrane-Assisted Crystallization Technology*, Imperial College Press, 2015.
373 E. Curcio, X. Ji, A. M. Quazi, S. Barghi, G. Di Profio, E. Fontananova, T. Macleod and E. Drioli, *J. Membr. Sci.*, 2010, **360**, 493–498.
374 C. A. Quist-Jensen, A. Ali, S. Mondal, F. Macedonio and E. Drioli, *J. Membr. Sci.*, 2016, **505**, 167–173.
375 C. Finnerty, L. Zhang, D. L. Sedlak, K. L. Nelson and B. Mi, *Environ. Sci. Technol.*, 2017, **51**, 11701–11709.
376 X. Li, J. Li, J. Lu, N. Xu, C. Chen, X. Min, B. Zhu, H. Li, L. Zhou, S. Zhu, T. Zhang and J. Zhu, *Joule*, 2018, **2**, 1331–1338.
377 M. Gao, C. K. Peh, L. Zhu, G. Yilmaz and G. W. Ho, *Adv. Energy Mater.*, 2020, **10**, 2000925.

378 A. H. Avci, C. Van Goethem, T. Rijnaarts, S. Santoro, M. Aquino, G. Di Profio, I. F. J. Vankelecom, W. M. De Vos, E. Fontananova and E. Curcio, *Mol. Psychiatry*, 2021, **26**, 265.
379 J. H. Jhaveri and Z. V. P. Murthy, *Desalination*, 2016, **379**, 137–154.
380 A. Nguyen, L. Zou and C. Priest, *J. Membr. Sci.*, 2014, **454**, 264–271.
381 J. R. Ray, S. Tadepalli, S. Z. Nergiz, K.-K. Liu, L. You, Y. Tang, S. Singamaneni and Y.-S. Jun, *ACS Appl. Mater. Interfaces*, 2015, **7**, 11117–11126.
382 Q. Jiang, D. Ghim, S. Cao, S. Tadepalli, K.-K. Liu, H. Kwon, J. Luan, Y. Min, Y.-S. Jun and S. Singamaneni, *Environ. Sci. Technol.*, 2019, **53**, 412–421.
383 A. Criscuoli, J. Zhong, A. Figoli, M. C. Carnevale, R. Huang and E. Drioli, *Water Res.*, 2008, **42**, 5031–5037.
384 S. Mozia, A. W. Morawski, M. Toyoda and T. Tsumura, *Desalination*, 2010, **250**, 666–672.
385 Y. Shi, J. Huang, G. Zeng, W. Cheng and J. Hu, *J. Membr. Sci.*, 2019, **584**, 364–392.
386 X. Li, J. Yu, S. Wageh, A. A. Al-Ghamdi and J. Xie, *Small*, 2016, **12**, 6640–6696.
387 Z. Gan, X. Wu, M. Meng, X. Zhu, L. Yang and P. K. Chu, *ACS Nano*, 2014, **8**, 9304–9310.
388 X. Wang, Y. He, Y. Hu, G. Jin, B. Jiang and Y. Huang, *Sol. Energy*, 2018, **170**, 586–593.
389 I. A. Said, T. R. Chomiak, Z. He and Q. Li, *Sep. Purif. Technol.*, 2020, **250**, 117170.
390 Y. Li, T. Verbiest, R. Strobbe and I. F. J. Vankelecom, *J. Mater. Chem. A*, 2013, **1**, 15031–15038.